

UNIVERSITY OF WARMIA AND MAZURY IN OLSZTYN

Technical Sciences

21(4) 2018



PUBLISHER UWM

Editorial Board

Ceslovas Aksamitauskas (Vilnius Gediminas Technical University, Lithuania), Olivier Bock (Institut National de L'Information Géographique et Forestière, France), Stefan Cenkowski (University of Manitoba, Canada), Adam Chrzanowski (University of New Brunswick, Canada), Davide Ciucci (University of Milan-Bicocca, Italy), Sakamon Devahastin (King Mongkut's University of Technology Thonburi in Bangkok, Thailand), German Efremov (Moscow Open State University, Russia), Mariusz Figurski (Military University of Technology, Poland), Maorong Ge (Helmholtz-Zentrum Potsdam Deutsches GeoForschungsZentrum, Germany), Dorota Grejner-Brzezinska (The Ohio State University, USA), Janusz Laskowski (University of Life Sciences in Lublin, Poland), Arnold Norkus (Vilnius Gediminas Technical University, Lithuania), Stanisław Pabis (Warsaw University of Life Sciences-SGGW, Poland), Lech Tadeusz Polkowski (Polish-Japanese Institute of Information Technology, Poland), Arris Tijsseling (Technische Universiteit Eindhoven, Netherlands), Vladimir Tilipalov (Kaliningrad State Technical University, Russia), Alojzy Wasilewski (Koszalin University of Technology,

Poland) Editorial Committee

Marek Markowski (Editor-in-Chief), Piotr Artiemjew, Kamil Kowalczyk, Wojciech Sobieski, Piotr Srokosz, Magdalena Zielińska (Assistant Editor), Marcin Zieliński

Features Editors

Piotr Artiemjew (Information Technology), Marcin Dębowski (Environmental Engineering), Zdzisław Kaliniewicz (Biosystems Engineering), Grzegorz Królczyk (Materials Engineering), Marek Mróz (Geodesy and Cartography), Ryszard Myhan (Safety Engineering), Wojciech Sobieski (Mechanical Engineering), Piotr Srokosz (Civil Engineering), Jędrzej Trajer (Production Engineering)

Statistical Editor

Paweł Drozda

Executive Editor

Mariola Jezierska

The Technical Sciences is indexed and abstracted in BazTech (<http://baztech.icm.edu.pl>) and in IC Journal Master List (<http://journals.indexcopernicus.com>)

The Journal is available in electronic form on the web sites
<http://www.uwm.edu.pl/techsci> (subpage Issues)
<http://wydawnictwo.uwm.edu.pl> (subpage Czytelnia)

The electronic edition is the primary version of the Journal

PL ISSN 1505-4675
e-ISSN 2083-4527

© Copyright by Wydawnictwo UWM • Olsztyn 2018

Address

ul. Jana Heweliusza 14
10-718 Olsztyn-Kortowo, Poland
tel.: +48 89 523 36 61
fax: +48 89 523 34 38
e-mail: wydawca@uwm.edu.pl

Contents

M. MIATSIELSKI, B. STARUCH, B. STARUCH – <i>An Integer Optimization Model and Algorithms to Support the Cost-Revenue Study and Provisionary Designing Warehouses Or Other Storage Objects</i>	257
J. PELC – <i>Numerical Equilibrium Analysis of a Stack of Steel Post Pallets</i>	271
K. GRABOWSKA, J. KRZYWAŃSKI, K. SZTEKLER, W. KALAWA, W. NOWAK – <i>Fuzzy Logic Approach in the Analysis of Heat Transfer in a Porous Sorbent Bed of the Adsorption Chiller</i>	281
T. KRZYWICKI – <i>Weather and a Part of Day Recognition in the Photos Using a kNN Methodology</i>	291
W. LUDWIG – <i>Impact of Friction Coefficient on Particles Circulation Velocity Calculated by Euler-Lagrange Model in Spouted Bed Apparatus for Dry Coating</i>	303
Z. KALINIEWICZ, Ł. MALESZEWSKI, Z. KRZYŚIAK – <i>Influence of Saw Chain Type and Wood Species on the Kickback Angle of a Chainsaw</i>	323
M. GWOŹDZIK – <i>Evaluation of High-Temperature Corrosion On 13CrMo4-5 Steel Operated in the Power Industry</i>	335
J. KUBIASZCZYK, E. GOLISZ, M. JAROS – <i>The Effect of Trays' Slope in the Tunnel Dryer on Drying Rate of Carrot Cubes</i>	345



Quarterly peer-reviewed scientific journal

ISSN 1505-4675
e-ISSN 2083-4527

TECHNICAL SCIENCES

Homepage: www.uwm.edu.pl/techsci/



AN INTEGER OPTIMIZATION MODEL AND ALGORITHMS TO SUPPORT THE COST-REVENUE STUDY AND PROVISORY DESIGNING WAREHOUSES OR OTHER STORAGE OBJECTS

Mikalai Miatselski, Bożena Staruch, Bogdan Staruch

Division of Algebra and Geometry
Faculty of Mathematics and Computer Science
University of Warmia and Mazury in Olsztyn

Received 8 September 2018; accepted 17 October 2018; available online 19 October 2018.

Key words: warehouses design, cost-revenue recognition, state space, model and algorithms, nonlinear and integer programming.

Abstract

An optimization model for the cost–revenue study at the stage of system analysis and preliminary designs of storage objects such as warehouses, containers, packs and similar objects are developed. Our assumptions motivated by warehouses design lead us to a nonlinear integer optimization problem with the only basic constraint. We present algorithmic methods for obtaining the exact solution to the general problem with emphasizing the special case when both the objective and the constraint functions are increasing. The results of the paper may be used in developing software tools intended for supporting designers.

Introduction

An optimization model for the cost–revenue study at the stage of system analysis and provisory designs of storage objects such as warehouses, containers, packs and similar objects are developed. The design includes both: single objects and object complexes.

Correspondence: Bożena Staruch, Katedra Algebry i Geometrii, Wydział Matematyki i Informatyki, Uniwersytet Warmińsko-Mazurski, ul. Słoneczna 54, 10-710 Olsztyn, e-mail: bostar@matman.uwm.edu.pl

The problem of warehouses design is the strategic factor in the success of many businesses and hence there is a need of developing different types of warehouse storage solutions. A lot of companies offer their support in warehouse and layout design (see, e.g., Mecalux, Logistics Bureau). Scientific articles concern mainly layout design (see CHITTRATANAWAT 1999, SINGH, SHARMA 2006, VAN CAMP et al. 1991). A design project of a warehouse should compile as much information as possible, so that the installation fulfils its function and can even adapt to any future needs that may arise. It is essential that designers clearly understand all the characteristics of storing goods: the load unit used, its dimensions and the required dimensions of the shelves and the installation work areas, as well. The dimensions and characteristics of the warehouse infrastructure are essential and must be very accurate information. They are required for the design of shelves, to calculate the capacity of the installations and the distribution of the goods inside the warehouse.

The following simplified sequence of relationships underlies our approach: entrepreneur's revenue from selling storage services is roughly proportional to the total loading of all the storage objects the latter, in turn, is roughly proportional to the entire interior volume of the storage objects and, finally, the interior volume of all the pre-designed objects is a function of their dimensions. Such a function may be defined either by an analytical formula or even by an algorithm.

Naturally, the objective function is maximized subject to constraints that express budget limitation derived from landscape peculiarities or by structural or technological norms and regulations. The major financial constraint takes into account costs (prices) of the building materials, raw and fabricated, letting the other construction expenses (e.g. caused by purchasing and installing the equipment or facilities, labor costs etc.) be represented by a collective evaluation. There are also limitations that must be included: access, floors, windows, columns, boxes, lines and power lines are all examples of parts of an installation that influence its design. Furthermore, there are the building regulations that directly affect the calculations of storage structures.

Structural and technology requirements imply that we mainly deal with a nonlinear integer optimization problem. The main version is proved to be an *NP*-hard problem. We study basic properties of this problem which underlie our algorithms. Examples and applications are given as well.

Although our algorithms are based on searching the state space and have exponential complexity instances of the presented problem with a small number of variables are solved efficiently. In case of a large number of variables it is worth looking for fast sub-optimal algorithms enriched with the appropriate tests for optimality.

The paper is organized as follows. First, we present assumption and conventions that are motivated by practice. Next an optimization problem for three decision variables is described together with its algorithmic solution. Later

we generalize this problem to n decision variables. We also discuss the role of the choice of the set of parameters (that corresponds to decision variables) characterizing the predesign shape of construction. Finally, we consider increasing property of both the objective function and the constraint function and we give an algorithm based on this property.

Assumptions and conventions

Assume that an entrepreneur has a land area sufficient to build a logistics center, the main object of which would be a warehouse to provide regular revenue, and therefore to gain profit from the provision of warehousing and storage services for goods, raw materials, semi-finished products, etc., generally called “loading” of the magazine. We also make the following assumptions:

- regular income is quite stable and proportional to the amount of the whole loading stored;

- the size of the loading is related to the interior volume: larger volume creates a predisposition for greater loading. In any case, the lack of space at the occurrence of demand for storage services clearly leads to revenue losses;

- storage capacity depends on the geometric shape and individual dimensions of the warehouse. The most common shapes of real structures are quite simple: a cuboid (possibly with a “gable roof” or a shade), a pyramid or pyramid truncated;

- assuming the geometric shape of the storage structure to be already defined, we have that the values of the basic dimensions of the construction determine the final design of the interior space of the warehouse. Such a project is designed to provide the largest volume of interior space and thereby maximize the potential loading of the warehouse. This means that the dimensions are variable values, selectable in certain intervals and subject to some constraining conditions (in other words, they are supposed to be *decision variables* in appropriate optimization mathematical models);

- as the basic limiting condition, we require that the pre-determined amount of money for warehouse construction be not exceeded. We assume that the costs are dependent on the prices of building materials used for the structural components, i.e. walls, floor, roof and so on. Also, other costs such as design, land preparation and development, energy infrastructure for machines, energy costs of equipment exploitation, labor, etc. are under consideration. The entire sum of costs is presented as a function dependent on decision variables;

- summing up, we would like to develop and explore a model for achieving best business results based on the provision of stock warehousing services at the design stage of storage facilities, depending on the structural components and dimensions of the building.

Formulation of optimization model

We start with an example of an optimization model for a cuboid warehouse. The problem is to determine the size of the warehouse with the greatest volume under budget. We take the following assumptions:

- the warehouse is a cuboidal building described by three parameters: length, width and height denoted, respectively, by x_1, x_2, x_3 . In our optimization problem these parameters measured e.g. in meters will play the role of decision variables. Our purpose is to maximize volume of the cuboid, hence the function $\text{Vol}(x_1, x_2, x_3) = x_1 x_2 x_3$ will constitute the objective function;

- the parameters values are restricted to intervals determined by lower bounds l_1, l_2, l_3 and upper bounds u_1, u_2, u_3 ;

- the construction expenses are obtained by summing costs of the main parts of the building such as walls, floor, roof and others which are supposed to be proportional to their surfaces. Let a, b, c, d denote the given unit costs of construction of one square meter of the floor, side and rear walls, roof, and the front wall, respectively;

- the total cost (denoted by **Cost**) of constructing the warehouse is the sum of all the main parts and some costs e that are independent of the size of the building. Hence, we obtain a mathematical expression for the constraint function:

$$\text{Cost}(x_1, x_2, x_3) = ax_1x_2 + b(2x_2x_3 + x_1x_3) + cx_1x_2 + dx_1x_3 + e;$$

- let B denote the budget limitation for the investment. Thus, we obtain the following constraint on the size of the building: $\text{Cost}(x_1, x_2, x_3) \leq B$;

- finally, the problem can be stated as follows: maximize $\text{Vol}(x_1, x_2, x_3)$ subject to:

$$\text{C1 } \text{Cost}(x_1, x_2, x_3) \leq B,$$

$$\text{C2 } l_i \leq x_i \leq u_i, l_i < u_i \text{ and } l_i, u_i \text{ are nonnegative reals for every } i = 1, 2, 3;$$

- the integer form of this problem assumes that x_i, l_i, u_i are nonnegative integers.

The integer optimization problem with three decision variables will be abbreviated as **IP3** (Integer Problem with 3 decision variables). Certainly, **Vol** and **Cost** in **IP3** can be different from those presented in above.

The above problem can be stated for continuous variables and hence certain attempts to apply real analysis optimization methods may be done. However, as we assume that the objective function describes the volume not only of a warehouse but also of a container or a collection of containers, the **Vol** function may have many different types and forms. Practically, any arbitrary function, even defined by an algorithm (with no explicit formula given) can be considered as an objective function. The constraint function **Cost** is assumed to express

the sum of all the construction costs. Therefore, there is no reason to assume any ‘nice’ analytic property such as differentiability, continuity or convexity of any of these two functions.

In this situation, an approach based on partial enumeration of feasible solutions, seems to be the only practically efficient technique. Certainly, we realize that even decision problem of simple membership in the feasible region may turn out to be hard. Nevertheless, strong variability of objective functions justifies this approach in our work. Moreover, we assume that, as a rule, in practical applications the variables are integer. For example, the walls are made of some normalized components (modules) of a given size or the material is stored in containers of a given size. For this reason, we assume that the parameters are measured in some units depending on a specific situation and we consider the values of variables to be integer multiples of these units. Consequently, these units are used to calculate costs. Hence, we focus our attention on integer optimization problems such as **IP3** or more generally, **IP n** , where n is the number of decision variables.

Algorithmic solution of **IP3**

The set of all the integer points satisfying C2 will be called the state space. To solve the **IP3** problem we need to scan the state space S :

$$S = [l_1, u_1] \cdot [l_2, u_2] \cdot [l_3, u_3],$$

where $[l_i, u_i] = \{l_i, l_i + 1, \dots, u_i\}$ for every $i = 1, 2, 3$.

If a point in S satisfies the constraint C1 i.e. is a feasible solution, then the value of **Vol** is calculated, and finally, the points with the greatest value of **Vol** are the optimal solutions.

Below the reader will find the pseudo-code of an algorithm which for every point in S checks if this point is a feasible solution, and if the answer is “yes” it calculates the value of **Vol**. The points with currently the highest value of the variable V are remembered (**REMEMBER**) and they are cleared (**CLEAR**) as soon as V becomes greater.

Algorithm-3DmaxVolume

Vol: = 0; **V**: = 0

FOR $l := u_l$ DOWNTO l_l

 FOR $w := u_w$ DOWNTO l_w

 FOR $h := u_h$ DOWNTO l_h

 IF (**Cost**(l, w, h) $\leq B$) THEN

$V := \text{Vol}(l, w, h)$

```

IF (V = Vol) THEN
REMEMBER (l, w, h)
END IF
IF (V > Vol) THEN
Vol := V
CLEAR
REMEMBER (l, w, h)
END IF
END IF
END FOR
END FOR
END FOR
END

```

The above algorithm scans the whole state space, so it makes $(1 + u_l - l_l) \cdot (1 + u_w - l_w) \cdot (1 + u_h - l_h)$ of steps. To improve effectivity of solving IC3 some deeper analysis of the functions **Vol** and **Cost** should be done.

The IPn model

We present here a general optimization model **IPn**. By assuming a general point of view, we are able to consider any solid figure (or even a collection of solid figures) the volume of which is being maximized. We assume that such a figure is described by a set of parameters (*describing parameters*) that characterizes this figure in the sense that there is a function on the set of parameters returning its volume. Assume that we have:

- describing parameters x_1, \dots, x_n that fully characterize the figure as a rigid body;
- the volume function $\text{Vol}(x_1, \dots, x_n)$ to be maximized;
- the cost function $\text{Cost}(x_1, \dots, x_n)$ limited by a fixed number B ;
- integer values of describing parameters that are constrained by the integer lower and upper bounds $0 \leq l_i \leq u_i$ so that $l_i \leq x_i \leq u_i$ for every $i = 1, \dots, n$.

The state space of this problem consists of integer points of the n -orthotope S :

$$S = [l_1, u_1] \cdot \dots \cdot [l_n, u_n],$$

where $[l_i, u_i] = \{l_i, l_i + 1, \dots, u_i\}$ for every $i = 1, \dots, n$.

Then the **IPn** problem is formulated as follows:

Maximize $\text{Vol}(x_1, \dots, x_n)$, subject to

C1 $\text{Cost}(x_1, \dots, x_n) \leq B$, where B is a positive real,

- C2 $l_i \leq x_i \leq u_i$ and $0 \leq l_i \leq u_i$, where x_i, l_i, u_i are nonnegative integers for $i = 1, \dots, n$
- C3 $S \subseteq D_{\text{Vol}} \cap D_{\text{Cost}}$, where $D_{\text{Vol}}, D_{\text{Cost}}$ are the domains of **Vol** and **Cost**, respectively.

Any solution of the above problem is based on searching (exhaustively or partially) the state space, checking constraints and choosing the optimal solution (or solutions). Obviously, the cardinality of S is equal to:

$$\text{card}(S) = (1 + u_1 - l_1) \cdot \dots \cdot (1 + u_n - l_n) \leq [\max\{(1 + u_1 - l_1), \dots, (1 + u_n - l_n)\}]^n$$

Therefore, it is important that the chosen set of describing parameters be minimal. The choice of describing parameters is crucial in faster methods for solving the problem.

The 3DmaxVolume algorithm easily generalizes (n nested loops FOR) to the algorithm n DmaxVolume solving IP n . Notice that the condition C3 guarantees the correctness of this generalization. If C3 is not satisfied, the n DmaxVolume algorithm should be improved by introducing the mechanism for checking if the current point belongs to $D_{\text{Vol}} \cap D_{\text{Cost}}$. If the answer is “no” the next point is taken. As the n DmaxVolume algorithm is of exponential time complexity, other quick methods for solving IP n are worth of considering including methods based on some kind of heuristics. For example, genetic or other evolutionary algorithm would bring a suboptimal solution in better time. It depends on preferences of the entrepreneur if the exact solution with bigger cost is required, or if a non-exact suboptimal solution is good enough to use.

Choosing describing parameters

The next two examples show that even for a fixed solid figure there are various choices of describing parameters. Every choice has some advantages and disadvantages, as well. The solid figure in Example 1 is a cone and the value of the cost function is given as the value of the lateral surface area. It can be characterized by two parameters e.g. radius r and height h , or radius r and slant height l .

Example 1 (Cone):

– $\text{Vol}(r, h) = \frac{1}{3}\pi r^2 h$, $\text{Cost}(r, h) = \pi r \sqrt{r^2 + h^2}$. Here, the constraint C3 is satisfied:

– $\text{Vol}(r, l) = \frac{1}{2}\pi r^2 \sqrt{l^2 - r^2}$, $\text{Cost}(r, l) = \pi r l$. Here, the domain of **Vol** is restricted to pairs $l > r$. In this case, the improved version of 2DmaxVolume should be used or some change in describing parameters should be done. Let us introduce a new decision variable $x = l - r, x \geq 0$. Then $\text{Vol}(r, x) = \frac{1}{3}\pi r^2 \sqrt{(x + r)^2 - r^2}$, $\text{Cost}(r, x) = \pi r(x + r)$ and C3 is satisfied.

When the solid figure is a conical frustum, created by slicing the top off a cone with a cut parallel to the base, we need at least three parameters.

Example 2 (Conical Frustum). Describing parameters: L, r, R , where R is the radius of the base, r is the radius of the top, and L is the slant height. Then $\text{Vol}(L, r, R) = \frac{1}{3}\pi\sqrt{L^2 - (R - r)^2}(R^2 + Rr + r^2)$, and $\text{Cost}(L, r, R) = a\pi R^2 + b\pi r^2 + c\pi(R + r)L$, where a, b, c are unit costs of constructing the base, the top and the lateral surface, respectively. Here the domain assumptions that $R > r$ and $L > R - r$ can be used. By substituting new variables $x = R - r, x > 0$ and $y = L - x, y > 0$ we obtain a model with describing parameters x, y, r that satisfies C3.

NP-hardness of IPn

To show that **IPn** is **NP-hard** we present a polynomial (linear) reduction of the very known **KNAPSACK** problem) to **IPn**. To learn more on **KNAPSACK** problems see e.g. KELLERER et al. (2004).

Based on a **KNAPSACK** instance:

maximize $a_1x_1 + \dots + a_nx_n$, subject to

$$c_1x_1 + \dots + c_nx_n \leq C,$$

where x_i are nonnegative integers for every $i = 1, \dots, n$

create the following instance of **IPn**:

maximize $\text{Vol}(x_1, \dots, x_n) = a_1x_1 + \dots + a_nx_n$, subject to

$$\text{Cost}(x_1, \dots, x_n) = b_1(2a_1 + 2)x_1 + \dots + b_n(2a_n + 2)x_n \leq B,$$

where x_i are positive integers and $b_i = \frac{c_i}{2a_i + 2}$ for every $i = 1, \dots, n$ and $B = C + (a_1 + \dots + a_n)$.

It is easy to see that the model **IPn** describes the situation of designing a collection of n bins of sizes $1, a_i, x_i, i = 1, \dots, n$. Such a collection may be intended for serial batch manufacturing. The very creation of the model instance uses linear time $O(n)$. Any optimal solution of the **IPn** is an optimal solution of the **KNAPSACK** instance. **NP-hardness** of **KNAPSACK** implies **NP-hardness** of **IPn**.

Increasing assumption

In this section we consider an assumption that the functions Vol and Cost are increasing. This allows us to propose an algorithm solving IP2 in linear time and to lower time complexity of IPn.

Basic definitions and properties

Let $\check{x} = (x_1, \dots, x_n)$ and let $(\check{x}, x_i/a) = (x_1, \dots, x_{i-1}, a, x_{i+1}, \dots, x_n)$ denote an n -tuple obtained from \check{x} by substitution a for x_i , where $1 \leq i \leq n$. Analogously, $(\check{x}, x_i/a, x_j/b)$ stands for an n -tuple obtained from \check{x} by substitution a for x_i and b for x_j , where $1 \leq i < j \leq n$.

Let f be a real function of n variables x_1, \dots, x_n and let $D_f \subseteq R^n$. We say that:

– f is increasing on variable x_i on a set $A \subseteq D_f$ if and only if for any $a < b$ with $(\check{x}, x_i/a), (\check{x}, x_i/b) \in A$ it holds that $f(\check{x}, x_i/a) \leq f(\check{x}, x_i/b)$;

– f is strictly increasing on variable x_i on a set $A \subseteq D_f$ if and only if for any $a < b$ with $(\check{x}, x_i/a), (\check{x}, x_i/b) \in A$ it holds that $f(\check{x}, x_i/a) < f(\check{x}, x_i/b)$;

– f is increasing on a set $A \subseteq D_f$ if and only if f is increasing on a set A on every variable;

– f is strictly increasing on a set $A \subseteq D_f$ if and only if f is strictly increasing on a set A on every variable.

Example 3:

– in Example 1.1, the functions **Vol** and **Cost** are strictly increasing on their domains;

– in Example 1.2, the function **Vol**(r, l) is strictly increasing on l and it would not be increasing on r . After substitution, Vol(r, x) is strictly increasing on its domain;

– in Example 2, **Vol**(L, r, R) is strictly increasing on variables r, L and would not be increasing on R . The cost function Cost is strictly increasing on its domain. After substitution, **Vol**(x, r, y) is strictly increasing on its domain;

– as the state space S is a Cartesian product, the natural ordering \preceq (state space ordering) on S is determined. Namely, for any $(x_1, \dots, x_n), (y_1, \dots, y_n) \in S$:

– $(x_1, \dots, x_n) \preceq (y_1, \dots, y_n)$ if $x_i \leq y_i$ for every $i = 1, \dots, n$;

– $(x_1, \dots, x_n) < (y_1, \dots, y_n)$ if $x_i \leq y_i$ for every $i = 1, \dots, n$ and there is $j \leq n$ with $x_j < y_j$.

Directly from definition of the order \preceq we have that a function $f: R^n \rightarrow R$ is increasing (strictly increasing) on the state space S if and only if $S \subseteq D_f$ and for any $\tilde{x}, \tilde{y} \in S$, if $\tilde{x} \prec \tilde{y}$ then $f(\tilde{x}) \leq f(\tilde{y})$ ($f(\tilde{x}) < f(\tilde{y})$).

Proposition 1. If the objective function **Vol** is:

– increasing, then for any optimal solution \tilde{a} there exists a maximal (in the order \preceq restricted to feasible solutions) element \tilde{m} which is an optimal solution of **IPn**;

– strictly increasing, then any optimal solution of **IPn** is a maximal element among feasible solutions.

To see the correctness of the above proposition, let \tilde{a} be an optimal solution of **IPn** with $\tilde{a} \prec \tilde{x}$ for a feasible solution \tilde{x} . If **Vol** is increasing, then $\text{Vol}(\tilde{a}) \leq \text{Vol}(\tilde{x})$ and, as $\text{Vol}(\tilde{a})$ is maximal we have $\text{Vol}(\tilde{a}) = \text{Vol}(\tilde{x})$, which means that \tilde{x} is an optimal solution. If **Vol** is strictly increasing, then $\text{Vol}(\tilde{a}) < \text{Vol}(\tilde{x})$, which yields a contradiction.

A linear algorithmic solution of **IP2**

Proposition 1 and the next observation will be used in our algorithms in the sequel. Let us say that $\tilde{x} \in S$ satisfies the cost constraint if $\text{Cost}(\tilde{x}) \leq B$ and \tilde{x} does not satisfy the cost constraint, in the opposite case.

Proposition 2. If the function **Cost** is increasing on its domain and $S \subseteq D_{\text{Cost}}$ then for any $\tilde{x}, \tilde{y} \in S$

– if \tilde{x} satisfies the cost constraint and $\tilde{y} \preceq \tilde{x}$ then \tilde{y} satisfies the cost constraint;

– if \tilde{x} does not satisfy the cost constraint and $\tilde{x} \preceq \tilde{y}$ then \tilde{y} does not satisfy the cost constraint, either.

This proposition can be used to fit upper bounds u_i in **IPn C2** as follows:

Algorithm-Fitting (x_i)

WHILE ($(\text{Cost}(\tilde{i}, l_i/u_i) > B)$ AND $(u_i > l_i)$)

$u_i := u_i - 1$

END WHILE

OUTPUT u_i

END

Assume from now on that the upper bound for every decision variable is set by the above algorithm, and that **Vol** is strictly increasing and **Cost** is increasing on S (increasing assumptions). First, we will present the algorithm for **IP2** (based on Proposition 2) that finds maximal feasible solutions which are, at the same time, optimal solutions (by Proposition 1).

Let $S \subseteq D_{\text{Vol}}$ be a 2-D state space. Let x, y be the decision variables with $k \leq x \leq K$, $l \leq y \leq L$. We present an algorithm solving IP2 in at most $(1 + K - k) + (1 + L - l)$ steps.

Algorithm 2D-IncreasingAssumptions (2D-IA)

```

x := k; y := L
WHILE ((x ≤ K) AND (y > l))
  WHILE ((Cost(x, y) ≤ B) AND (x ≤ K))
    x := x + 1
  END WHILE
  REMEMBER (x - 1, y)
  WHILE ((Cost(x, y) > B) AND (y > l))
    y := y - 1
  END WHILE
END WHILE
END

```

The algorithm starts in the North-West corner ($x = k; y = L$) of the rectangle $[k, K] \cdot [l, L]$. As (k, L) satisfies the cost constraint, (k, b) satisfies the cost constraint for every $b < L$. In this situation, we should move right ($x = x + 1$) and repeat this procedure until (x, y) does not satisfy the cost constraint. And again, we move down then right and so on. The algorithm ends when we get to the bottom or to the right-side boundary of the rectangle.

Time complexity of this algorithm (the number of visited points) is not greater than the length of the path starting in the North-West corner and ending in the South-East corner, which is equal to $(1 + K - k) + (1 + L - l) - 1$. The usage of space is not greater than $\min(1 + K - k; 1 + L - l)$, because every line (row or column) contains at most one maximal element. To obtain optimal solutions it is enough to calculate the values of Vol for every remembered point and choose the best ones.

An algorithmic solution of IP3

Consider IP3 and choose a variable (say, z with $m \leq z \leq M$) and repeat the 2D-IA algorithm for x, y and every fixed z . For simplicity, let

2D-IA($x; k; K; y; l; L; \text{Cost}(x, y, z)$)

mean that 2D-IA runs for variables x, y with the cost function $\text{Cost}_z(x, y) = \text{Cost}(x, y, z)$ is for a fixed value z , bounded as $k \leq x \leq K, l \leq y \leq L$

Algorithm 3D-IncreasingAssumptions (3D-IA)

```

FOR z: = m TO M
  RUN 2D-IA(x; k; K; y; l; L; Cost(x, y, z))
END FOR
END
    
```

This algorithm needs at most $(1 + M - m) \cdot ((K - k) + (L - l) + 1)$ steps. Algorithm 3D-IA easily generalizes to higher dimensions (n D-IA algorithm) by using the appropriate number of FOR loops. Notice that the n D-IA algorithm can be used under assumption that the Vol and the Cost function are increasing only on a pair of decision variables.

A slight improvement of the n D-IA algorithm

Assume that Vol and the Cost are increasing functions on S . Notice that n D-IA solves IP n in time $s_1 s_2 \dots s_{n-2} (s_{n-1} + s_n - 1)$, where $s_i = 1 + u_i - l_i$ for $i = 1, 2, \dots, n$. Moreover, if the variables are ordered according to increasing values of s_i i.e. $s_1 \leq s_2 \leq \dots \leq s_n$ then

$$s_1 s_2 \dots s_{n-2} (s_{n-1} + s_n - 1) \leq s_{\pi(1)} s_{\pi(2)} \dots s_{\pi(n-2)} (s_{\pi(n-1)} + s_{\pi(n)} - 1),$$

where π is a permutation of n .

To show the last property consider $E_1 = s_1 s_2 \dots s_{n-2} (s_{n-1} + s_n - 1)$ and $E_2 = s_1 s_2 \dots s_{i-1} s_{i+1} \dots s_{n-1} (s_i + s_n - 1)$ for some $1 \leq i \leq n - 2$. Then $E_1 = s_1 s_2 \dots s_{n-2} (s_{n-1} - 1) + s_1 s_2 \dots s_{n-2} s_n$ and $E_2 = s_1 s_2 \dots s_{n-2} (s_{n-1} - 1) + s_1 s_2 \dots s_{i-1} s_{i+1} \dots s_{n-1} s_n$

As the first components are equal, we compare the second ones:

$$\frac{s_1 s_2 \dots s_{n-2} s_n}{s_1 s_2 \dots s_{i-1} s_{i+1} \dots s_{n-1} s_n} = \frac{s_i}{s_{n-1}} \leq 1.$$

This yields that $E_1 \leq E_2$.

Conclusions and remarks

In the paper, we introduced into consideration and investigated a problem of warehouse design under budget limitation. Certainly, this motivation leads to the IP n problems which can be also used in other applications e.g. allocation problem (see IBARAKI and KATOH 1988). The proposed IP n model has a single constraint however it may be extended to a multi-constraint model.

When we make increasing assumptions on the IP n problem we obtain an instance of the nonlinear integer knapsack problem (see LI DUAN, SUN XIAOLING

2006). Therefore, methods for solving IPn can be used in a very wider class of problems and we think that developing methods presented in this paper is worth of effort (for example, an effective generalization of 2D-IA to higher dimensions is desirable).

References

- CAMP D. VAN, CARTER M., VANNELLI A. 1991. *A nonlinear optimization approach for solving facility layout problems*. European Journal of Operations Research, 57: 174–189.
- CHITTRATANAWAT S. 1999. *An integrated approach for facility layout, P/D location and material handling system design*. International Journal of Production Research, 37(3): 683-706.
- IBARAKI T., KATOH N. 1988. *Resource allocation problems: algorithmic approaches*. MIT Press, Cambridge, Mass.
- KELLERER H., PFERSCHY U., PISINGER D. 2004. *Knapsack Problems*. Springer Science & Business Media, Berlin.
- LI D., SUN X. 2006. *Nonlinear Integer Programming*. International Series in Operations Research & Management. Springer US.
- Logistics Bureau, <https://www.logisticsbureau.com>.
- Mecalux, <https://www.mecalux.com>.
- SINGH S.P., SHARMA R.R.K. 2006. *A review of different approaches to the facility layout problems*. The International Journal of Advanced Manufacturing Technology, 30: 425–433.



Quarterly peer-reviewed scientific journal

ISSN 1505-4675
e-ISSN 2083-4527

TECHNICAL SCIENCES

Homepage: www.uwm.edu.pl/techsci/



NUMERICAL EQUILIBRIUM ANALYSIS OF A STACK OF STEEL POST PALLETS

Józef Pelc

Department of Mechanical Engineering and Fundamentals of Machine Design
University of Warmia and Mazury in Olsztyn

Received 25 April 2018; accepted 20 November 2018; available online 21 November 2018.

Key words: pallet, stack, equilibrium, stability, imperfection, warehouse.

Abstract

A method for analyzing the equilibrium of a stack of loaded post pallets is presented. The finite element method was used to investigate the behavior of the bottom pallet in the stack during the addition of successive pallets. The stack was regarded as a self-stable multi-storey structure without bracings which is subjected to the weight of loaded pallets, horizontal forces resulting from sway and bow imperfections, and the impact of a forklift truck. The definite quadratic form of the tangent stiffness matrix after every increment in load was determined by nonlinear analysis to indicate the loss of post stability. An analysis of the stacking process of the evaluated pallets did not reveal a buckling trend in the posts of the bottommost pallet and demonstrated that the loss of equilibrium can lead to the collapse of the entire stack when a critical number of pallets is reached.

Introduction

Different types of pallets are used in warehouses for storing various products. Pneumatic tires are usually stored on steel post pallets. These pallets have a rigid bottom grid for storing tires. Posts are welded to the bottom grid, and the structural elements in the upper part of each post support the stacking of subsequent pallets. Pallets are stacked on top of each other to maximize storage space. However, the stack can become unstable when it reaches

Correspondence: Józef Pelc, Katedra Mechaniki i Podstaw Konstrukcji Maszyn, Wydział Nauk Technicznych, Uniwersytet Warmińsko-Mazurski, ul. M. Oczapowskiego 11, 10-719 Olsztyn, phone: +48 89 523 49 31, e-mail: joseph@uwm.edu.pl

a critical height, which can be caused by the buckling of the bottommost pallet or the collapse of the entire stack around the edge of its base. In daily practice, the determination of the safe maximum number of pallets in a stack poses a significant challenge for engineering staff. The above can be attributed to the absence of the applicable standards. Two pallet standards were previously in force in Poland (PN-M-78207: 1981, PN-M-78205: 1988). The first standard was revoked in 2012, and the second was revoked in 2015 without any replacements. These types of pallets have been rarely discussed in scientific and technical literature. WOLNY et al. (2014) investigated the stability and resistance of a box pallet to bending, stacking, free fall impact, lifting with a forklift truck, and horizontal impact with both edges and legs. They conducted analyses with the Finite Element Method (FEM) in the Femap/NEi Nastran system with the use of beam elements that are particularly useful in pallet design. Most published studies focus on pallet racks and on pallets for storing products in racks (on rack shelves) (BERNUZZI et al. 2015a, 2015b, SHAH et al. 2016). Unlike pallets, racks have post footings attached to the warehouse floor, and adjacent racks and pallet rack series are often connected by bracings, whereas post pallets are placed on the warehouse floor.

According to PELC (2017), a stack of post pallets should be regarded as a self-stable multi-storey structure without bracings. The above approach supports analyses of pallet stack stability with the use of the methods detailed in the standard applicable to steel structures (EN 1993-1-1:2005). The cited study proposes a calculation procedure and an exemplary analytical procedure for verifying the safety and stability of a stack of steel post pallets loaded with pneumatic tires.

This study relies on the FEM to propose a numerical method for determining the maximum number of loaded post pallets in a stack. The stability of structural components in the most loaded pallet, i.e. the bottommost pallet in the stack, and the stability of the entire stack were investigated by simulating the process of adding subsequent pallets to the stack. The vertical load of the bottommost pallet and the horizontal forces resulting from sway and bow imperfections increased with every additional pallet. The horizontal force generated by the forklift truck on the top pallet in the stack was taken into account based on the value calculated by TILBURGS (2001). The stack equilibrium was analyzed using the nonlinear incremental-iterative method, and the presence of a positive-definite or negative-definite quadratic form of the tangent stiffness matrix was determined after each increment. The absence of a positive-definite quadratic form was indicative of stack collapse. The FEM MSC.Marc/Mentat system was used in numerical simulations. In the analyzed case, pallet posts were stiff enough to prevent buckling, whereas a loss of static equilibrium was previously observed when the critical number of pallets was exceeded in the stack.

Computational Model

The pallet which was used to build the analyzed stack is shown in Figure 1. It was assumed that the rigid grid at the bottom the pallet was non-deformable.

The pallet computational model with specific dimensions is presented in Figure 2. The main structural elements of the pallet were: *1* – post (tubular section, 50×50×3), *2* – bed for the top pallet (angle bar, 50×50×4), *3* – crossbar (tubular section, 50×50×3), *4* – boom (flat, 50×8), *5* – bracket (tube, 50×3). In the analyzed pallet, dimensions *a*, *b*, *c*, *d*, *h* and *e* were determined at [m]: 1.25, 1.20, 1.07, 0.93, 1.50 and 0.09, respectively.

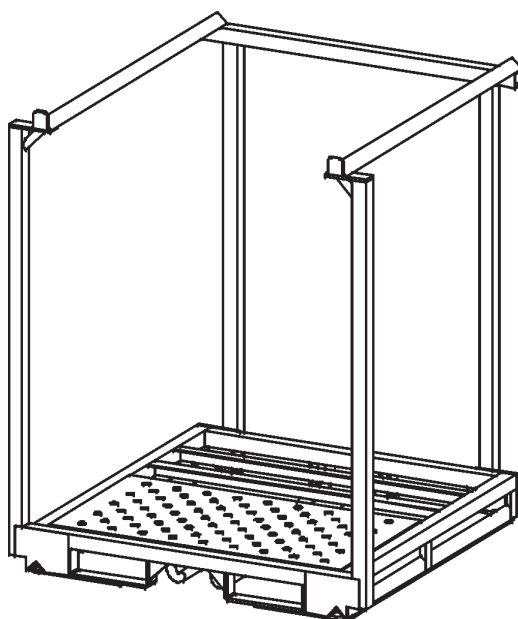


Fig. 1. View of the post pallet for storing pneumatic tires

The top pallet in the stack transfers load to the bottom pallet as a continuous load acting on the bed. In beds made of angle bars, the bar is bent around the axis of the minimum moment of inertia of the beam cross-section; therefore, it can be assumed that load will be transferred to the most rigid zones in the bed, i.e. points *A-D* which are supported by the posts. The rigid grid of the top pallet limits the relative displacement of points *A* and *B*, which is why they were joined by a non-deformable and weightless truss rod.

The bottommost pallet will be hereinafter referred to as the bottom pallet. The bottom pallet is subjected to the greatest load, and it determines the stability of the entire stack. The loads acting on successive pallets in the stack

were reduced to points A - D of the bottom pallet. It was assumed that the lower ends of the posts are fixed in the pallet's rigid grid and that the bottom pallet touches the floor at four points. Friction forces prevent horizontal displacement of the pallet. In order to apply boundary conditions, all three possible rotations of bottom post nodes were blocked, and non-deformable elements were used to connect pallet support points on the floor with bottom post nodes and with the post nodes located on the pallet grid (Fig. 2).

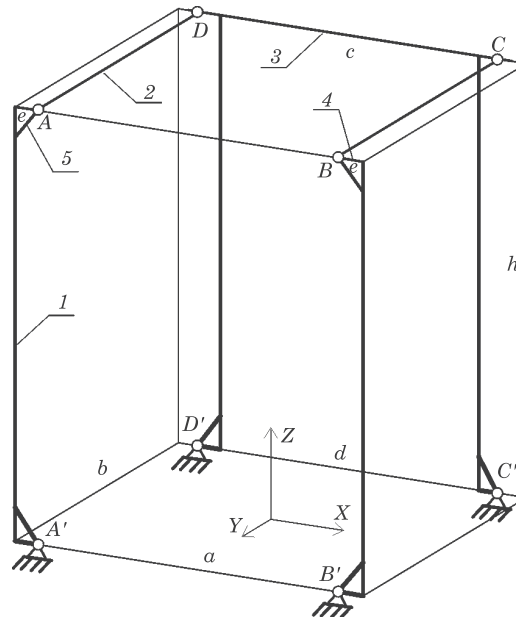


Fig. 2. Computational model of the post pallet (description in the text)

Sway and bow imperfections occurring in the system, whose values are specified in Standard EN 1993-1-1:2005, exert horizontal forces on the stack. The method of calculating these imperfections and the resulting values were presented in detail by PELC (2017). It should be noted that all possible translational and torsional sways were considered based on the recommendations formulated in the above Standard. The following inclinations were examined in this study: $DACB$ (forward), $BADC$ (torsional) and $BACD$ (left). The acronym $DACB$ indicates that points D and A move towards vector DA , whereas the remaining two points move towards vector CB . In the first two analytical cases, load-carrying capacity conditions were least satisfied by the bottom pallet in the stack (cf. PELC 2017). The forces acting on one point of the bottom pallet as a function of the number of pallets in the stack are presented graphically in Figure 3. The diagrams of increasing characteristic forces which were used in the analysis

of stack displacement and static equilibrium are similar, but their values are smaller than the values of the calculated forces. Vertical forces acting as pairs of opposite forces (couples) originate from the horizontal forces acting above the bottom pallet and represent the moment of stack collapse (Fig. 4).

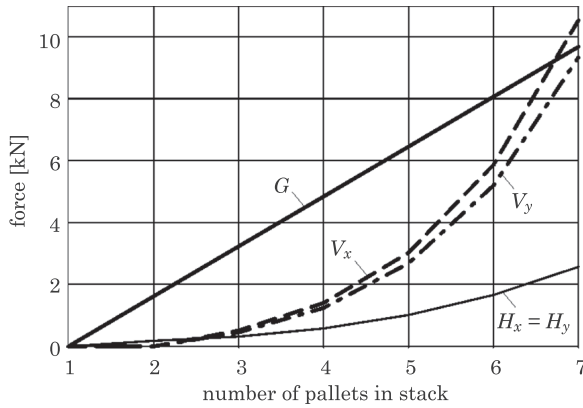


Fig. 3. Forces caused by weight (G) and imperfections (H – horizontal, V – vertical), acting on one point of the bottom pallet

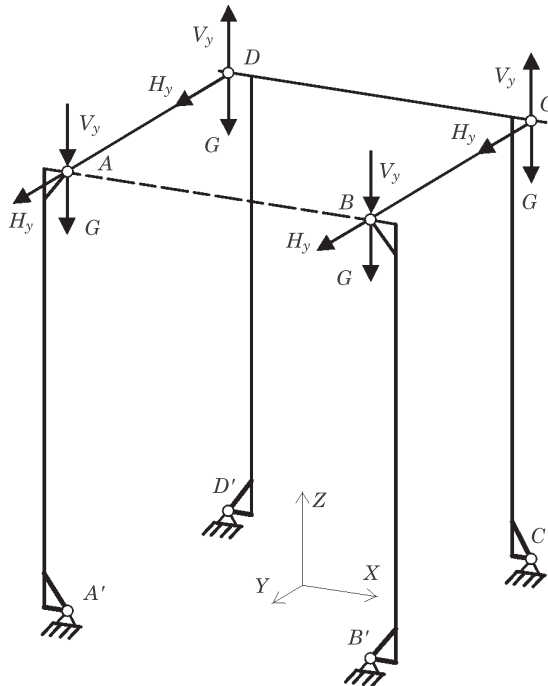


Fig. 4. Forces acting on the bottom pallet in case of DACB sway

A minor difference in the progression of vertical forces acting in planes parallel to planes XZ and YZ results from the difference in the distance between points A and B and points B and C ($AB < BC$), respectively.

Due to the significant values of horizontal forces acting on the stack (see Fig. 3) in addition to vertical forces, the maximum load-carrying capacity of the bottom pallet was calculated with a non-linear method. In the analyzed case, the distribution of forces is known, but the load, i.e. the number of pallets which cause stack instability, is unknown. In the total Lagrangian formulation, the increment in node displacement in the studied structure was determined from the following equation (BATHE 1982):

$$({}_0^t\mathbf{K}_L + {}_0^t\mathbf{K}_{NL}) \Delta\mathbf{U}^{(i)} = ({}^{t+\Delta t}\beta)^{\Delta t}\mathbf{R} - {}^{t+\Delta t}\mathbf{F}^{(i-1)} \quad (1)$$

where:

- ${}^{\Delta t}\mathbf{R}$ – vector of known loads in the first loading step,
- ${}^{t+\Delta t}\beta$ – scale parameter which determines load in time $t + \Delta t$. The index in brackets is the iteration number,
- ${}_0^t\mathbf{K}_L, {}_0^t\mathbf{K}_{NL}$ – linear and non-linear (geometric) part of the stiffness matrix, respectively,
- ${}^{t+\Delta t}\mathbf{F}^{(i-1)}$ – nodal force vector resulting from node displacement.

When load reaches the value which causes system instability, small increments in load are accompanied by large increments in displacement, and the tangent stiffness matrix (the sum is given in brackets in equation 1) becomes singular. Furthermore, the iterative process ceases to converge. The assumption that the linear stiffness matrix ${}_0^t\mathbf{K}_L$ does not change significantly before system buckling and that the non-linear stiffness matrix ${}_0^t\mathbf{K}_{NL}$ is a multiple of its initial form leads to the so-called linear (initial) stability analysis of the eigenvalue problem (cf WOOD 1992)

$$({}_0^0\mathbf{K}_L + \lambda \Delta {}_0^0\mathbf{K}_{NL}) \Delta\mathbf{U} = 0 \quad (2)$$

The smallest eigenvalue λ_1 is determined to calculate critical load $\lambda_1 \Delta {}^0\mathbf{R}$.

Two-noded beam elements with six degrees of freedom per node (three linear displacements and three angles of rotation) were used to analyze stack stability. The finite element model was composed of 294 elements (element 52 from MARC element library: straight, Euler-Bernoulli beam in space), and the assumed mesh density was validated with the mesh refinement method due to an approximation error. In a non-linear analysis examining the elastic behavior of the bottom pallet subjected to increasing load, the influence of large displacements (total Lagrangian formulation) was taken into account. The load imposed by additional pallets was increased in ten equal increments. The iterative process was conducted according to the Newton-Raphson procedure and was terminated when the displacement convergence criterion was satisfied.

Results and Discussion

A steel post pallet can be regarded as a frame whose legs are fixed in a non-deformable floor (grid at the bottom of the pallet). An initial/linearized stability analysis of the bottom pallet was performed according to (2). Vertical unit forces were applied to points A , B , C and D , and the lowest eigenvalue λ_1 was determined by solving the eigenvalue problem. The resulting critical load value was 62.7 kN. The fundamental mode of buckling was the lateral displacement and rotation of the upper part of the pallet (Fig. 5).

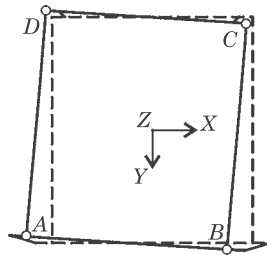


Fig. 5. The first mode of bottom pallet buckling

In sways $DACB$, $BADC$ and $BACD$, vertical reactions were examined at points where the bottom pallet was supported by the warehouse floor (Fig. 6) and at points of displacement of the forces applied to the pallet, i.e. points A , B , C and D (Fig. 7a, b). The diagrams presenting the changes in the values of vertical reactions acting on the bottom pallet indicate that all reactions had positive values up to six pallets in the stack, but when the seventh pallet was added, the reactions of some supports reached zero; therefore, negative reactions should be applied to balance the stack. This approach is possible in the adopted

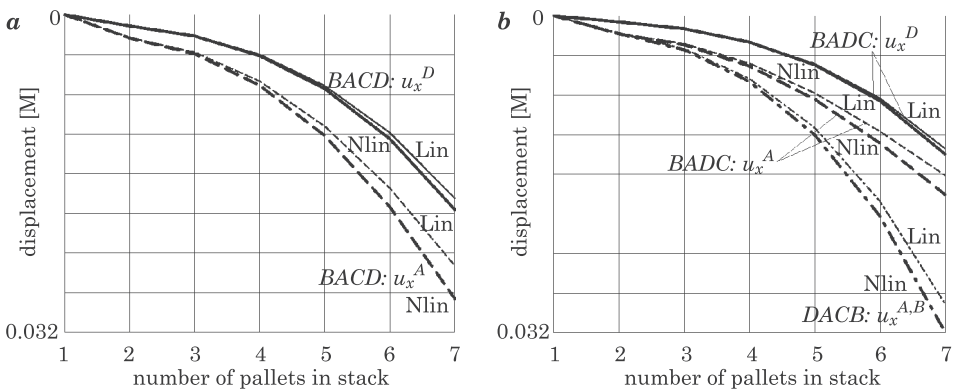


Fig. 6. Vertical reactions at points where they can assume negative value

model, but in reality, the pallet and the floor are bound by one-sided constraints, and the achievement of zero reaction force should be regarded as a loss of static balance. Changes in floor reaction forces acting on the bottom pallet in the three analyzed sways are presented in Figure 6, but only at points where a given number of pallets can change the sign of these reactions. These points are located opposite to the sway. For example when the stack sways to the left (*BACD*), these are points located on the right side of the pallet, i.e. *B'* and *C'*. Reaction forces increase monotonically in the remaining supports.

The displacement of points *A-D* on the bottom pallet increases monotonically with an increase in the number of pallets in the stack. In a stack with six pallets, the greatest displacement of 20.2 mm in the direction of the *y*-axis was noted in points *A* and *B* with *DACB* sway. Points *A* and *B* were least displaced in torsional sway *BADC*. The results of the linear analysis are presented in Figures 7*a* and 7*b*. In a stack with six pallets, the linear displacement of point *A* deviated most significantly from non-linear displacement in sway *BACD* (9.7%) and a similar deviation occurred in sway *BADC* (9.2%).

Displacement of points *A*, *B* and *D* on the bottom pallet as a function of the number of pallets in the stack in sways *DACB* and *BACD*.

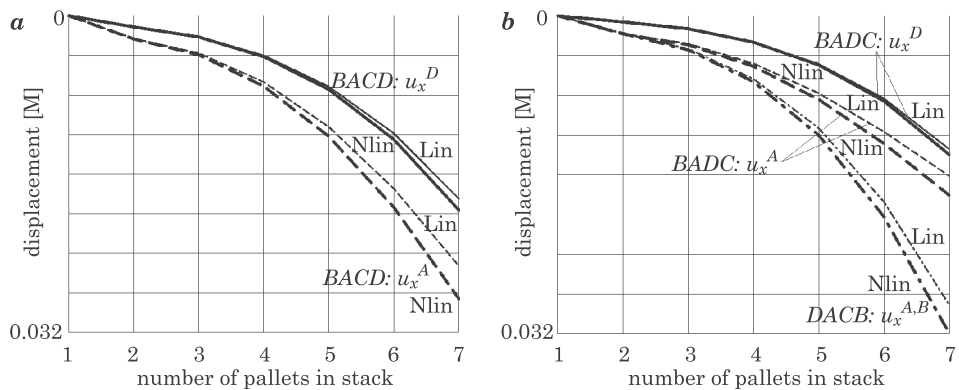


Fig. 7. Displacement of points *A* and *D* on the bottom pallet as a function of the number of pallets in the stack in sway *BACD* (a); displacement of points *A*, *B* and *D* on the bottom pallet as a function of the number of pallets in the stack in sways *DACB* and *BADC* (b):
 Lin – linear analysis, Nlin – non-linear analysis

It should be noted that the progression of displacement changed rapidly in an incremental manner when 5 pallets were stacked (refer to the variant of sway *DACB* in Figure 7*b*), which resulted from the rapid increase in horizontal forces mainly due to bow imperfection. The values of these forces depend on the values of the compressive normal forces acting on the posts, and they increase with the number of pallets in the stack.

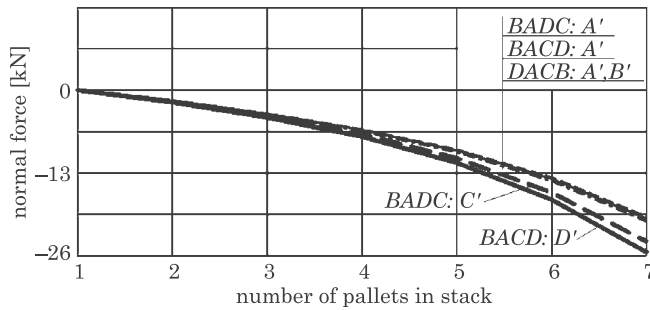


Fig. 8. Compressive normal forces acting on posts

Diagrams of compressive normal forces acting on pallet posts with different sway forms presented in Figure 8. In the case of the most dangerous sway *BACD*, the compressive force of 26 kN is far from the critical post force of 62.7 kN.

Conclusions

Vertical loads and equivalent horizontal loads acting on a stack as a result of sway and bow imperfections can be determined when a pallet stack is regarded as a multi-level self-stable structure.

The stability of stacked loaded post pallets can be effectively analyzed using the general non-linear incremental-iteration FEM procedure.

An analysis of the displacement history of the characteristic points on the bottom pallet indicates that geometric non-linearities exert a moderate influence on displacement. The greatest differences in displacement between linear and non-linear analysis were determined at 10%.

In an analysis of the equilibrium of a stack of post pallets loaded with pneumatic tires, static balance was lost when the seventh pallet was added. None of the posts in the bottom pallet buckled in the analyzed sways, which suggests that the evaluated post cross-sections confer high flexural stiffness.

References

- BATHE K.J. 1982. *Finite element procedures in engineering analysis*. Prentice-Hall, Englewood Cliffs, N.Y.
- BERNUZZI C., GOBETTI A., GABBIANELLI G., SIMONCELLI M. 2015a. *Unbraced pallet rack design in accordance with European practice*. Part 1. *Selection of the method of analysis*. *Thin Walled Structures*, 86: 185–207.
- BERNUZZI C., GOBETTI A., GABBIANELLI G., SIMONCELLI M. 2015b. *Unbraced pallet rack design in accordance with European practice*. Part 2. *Essential verification checks*. *Thin Walled Structures*, 86: 208–229.

- EN 1993-1-1:2005. Eurocode 3. *Design of steel structures*. Part 1.1. *General rules and rules for buildings*.
- PELC J. 2017. *Stability safety assessment for a stack of loaded steel post pallets*. BiTP, 47(3): 14–26, doi: 10.12845/bitp.47.3.2017.1.
- PN-M-78205:1988. *Palety ładunkowe metalowe. Wspólne wymagania i badania*.
- PN-M-78207:1981. *Palety ładunkowe słupkowe metalowe. Parametry podstawowe*.
- SHAH S.N.R., SULONG R.N.H., JUMAAT M.Z., SHARIATI M. 2016. *State-of-the-art review on the design and performance of steel pallet rack connections*. *Engineering Failure Analysis*, 66: 240–258.
- TILBURGS CEES J. 2001. *Regały dla poprawnie użytkowanych wózków*. Cz. 1. *Logistyka*, 1: 33–40.
- WOLNY S., ŁADECKI B., MATACHOWSKI F. 2014. *Designing folding wall box pallets*. *Mechanics and Control*, 33: 37–41.
- WOOD R. 1992. *Geometrically nonlinear finite element analysis*. In: *NAFEMS Introduction to Non-linear finite element analysis*. Ed. E. Hinton. Bell and Bain Ltd., Glasgow, p. 90–94.



FUZZY LOGIC APPROACH IN THE ANALYSIS OF HEAT TRANSFER IN A POROUS SORBENT BED OF THE ADSORPTION CHILLER

*Karolina Grabowska*¹, *Jarosław Krzywański*¹, *Karol Sztekler*²,
*Wojciech Kalawa*², *Wojciech Nowak*²

¹Institute of Technology and Safety System
Faculty of Mathematics and Natural Sciences
Jan Długosz University in Częstochowa

²Department of Thermal and Flow Machinery
Faculty of Energy and Fuels
AGH University of Science and Technology in Cracow

Received 25 June 2018; accepted 20 November 2018; available online 21 November 2018.

Key words: adsorption chiller, porous media, fuzzy logic, thermal conductivity, coated adsorption bed.

Abstract

Thermal conductivity in the boundary layer of heat exchange surface is the crucial parameter of adsorption process efficiency which occurs in the adsorption bed. In order to improve heat transfer conditions in the adsorption chiller, novel constructions of adsorption beds are currently investigated. The porous structure of the sorbent layer causes low thermal conductivity in the adsorption bed. One of the methods to improve heat transfer conditions is a modification of porous media bed structure with glue which is characterized with higher thermal conductivity. The optimum parameters of sorbents and glues to build the novel coated construction, in terms of improving the chiller Coefficient of Performance (COP) were defined in (Grabowska et al. 2018a). The paper implements fuzzy logic approach for predicting thermal conductivity of modified porous media layers. The developed model allows determination of the sorbent layer thermal conductivity based on various input parameters: arithmetic average of particle distribution d , density ρ and thermal diffusivity k . The data from empirical research was used to build up the model by fuzzy logic methods.

Correspondence: Karolina Grabowska, Instytut Techniki i Systemów Bezpieczeństwa, Wydział Matematyczno-Przyrodniczy, Uniwersytet Humanistyczno-Przyrodniczy im. Jana Długosza, al. Armii Krajowej 13/15, 42-200 Częstochowa, e-mail: k.grabowska@ujd.edu.pl

Nomenclature

- C_p – specific heat capacity, J/(kg·K)
 COP – coefficient of performance
 Q_e – heat received in the evaporation process, J
 Q_h – heat supplied during preheating phase of adsorption bed, J
 Q_d – heat supplied during desorption phase of adsorption bed, J
 d – arithmetic average of particle distribution, the averaged distance between the particles centers, m
 k – thermal diffusivity of coated sorbent sample, m²/s
 λ – thermal conductivity, W/(m·K)
 ρ – density of coated sorbent sample, kg/m³
 M – metal mass of heat exchange surface, kg
 m – adsorbent mass in adsorption bed, kg

Introduction

Adsorption refrigeration technology is an alternative source of cooling which significantly reduces electrical energy consumption for purposes of air conditioning. This technology utilizes low grade thermal energy sources as power supply for the adsorption chiller. Therefore, this technology will be a promising concept for sustainable development of the global economy. In the papers (SZTEKLER et al. 2017, KRZYWANSKI et al. 2018a) adsorption chillers driven by waste heat were investigated, and the possibility of utilizing heat produced in cogeneration was proven in (CHOROWSKI, PYRKA 2015). The biggest barrier in popularizing this ecological technology is the significantly lower coefficient of performance (COP) as compared with conventional refrigeration systems. This parameter of chiller efficiency is described by equation:

$$\text{COP} = \frac{Q_e}{Q_h + Q_d} \quad (1)$$

Therefore, research for the improvement of working cycle efficiency is being conducted. The crucial area of research is the heat transfer condition in the vicinity of the heat exchanger surface where this process is strongly limited by the porosity of the sorbent layer and the low thermal conductivity of the adsorption bed. Multiple factors are examined to improve the heat transfer processes, for example, a polydispersive structure of the sorbent bed, finned heat exchangers and changes to the working cycle conditions. The influence of metal additives on thermal resistance decrease in adsorption beds was also observed experimentally in (SHARAFIAN et al. 2014, ASKALANY et al. 2017). The optimization of fins geometry and metal mass/adsorbent mass (M/m) ratio were conducted in (FRENI et al. 2007, ROGALA 2017).

Experimental research of adsorbent bed thermal conductivity were conducted in (ROUHANI et al. 2018, ZHU, WANG 2002). The researchers have examined thermal properties of different types of porous media which are used in fixed adsorption beds. An analytical model and experimental studies of heat transfer in fixed bed of composite sorbent were presented in (FERREIRA et al. 2002). The well-known experimental research is supplemented by numerical models using Computational Fluid Dynamics (CFD) methods or artificial intelligence approach. It allows reduction of experiments costs because CFD methods enable study of a working cycle of an adsorption chiller numerically without expensive measurements and research stands. The CFD model of an adsorption bed, which was built based on boundary conditions from experimental thermal conductivity measurements of the sorbent layers is presented in (GRABOWSKA et al. 2018b). The special nature of heat and mass flow within porous media layers require formulating a specific computational domain in order to correctly describe the actual process. The novel approach to prepare the numerical simulations, especially in porous media volume, were discussed in (SOSNOWSKI 2017). Numerical modelling was used to optimize the performance of the silica gel/water multi-bed adsorption chiller in (REZK et al. 2013). Different mass allocation in the beds and various cold water temperatures were analysed. Improvement of cooling capacity by 10.78% was observed when cold water temperature was maintained at 20°C.

Artificial intelligence (AI) algorithms are another innovative method for adsorption chiller optimization. Neural networks and genetic algorithms were used to improve the cooling capacity (CC) of a three-bed adsorption chiller in (KRZYWANSKI et al. 2017). Calculated accuracy was excellent and the measured data has been preserved. The maximum relative error is lower than 10%. The AI modelling of a re-heat two-stage adsorption chiller was also presented in (KRZYWANSKI et al. 2018). In the paper (KRZYWANSKI, NOWAK 2016a) an alternative AI method was used to calculate the heat transfer coefficient in the combustion chamber of a circulating fluidized bed combustor (CFBC), which constitutes the fuzzy logic (FL) approach. Based on a specific set of received input data, the value of heat transfer coefficient at the output were determined. This modelling method also allows assessment of the individual input data impact on the output parameter. The most popular systems which use the fuzzy logic algorithms are consumer electronics based on fuzzy controller applications and also industrial and engineering automation systems. Moreover, new areas of FL applications are currently being researched (SOBOLEWSKI et al. 2016, HE et al. 2016).

The aim of this paper is to use the fuzzy logic approach in the analysis of heat transfer in a porous sorbent bed of an adsorption chiller.

Methods

The fuzzy logic model of thermal conductivity was built based on experimental measurements performed using the LFA (Laser Flash Methods) MicroFlash apparatus for different coated sorbent samples. Silica gel of various granulation was used as a sorbent and two different epoxy resins were used as a glue material. In the paper (GRABOWSKA et al. 2018a) it was proved that epoxy resin meets the conditions as the material to fill gaseous spaces in the adsorbent bed. The sample geometry used in the experiments is shown in Figure 1. Silica gel was used in the granulation range from $7 \cdot 10^{-4}$ to $10 \cdot 10^{-4}$ [m]. The particles distribution d means the averaged distance between the particles centers and this parameter was given by manufacturer of the silica gel. The results of experimental tests are presented in Table 1.

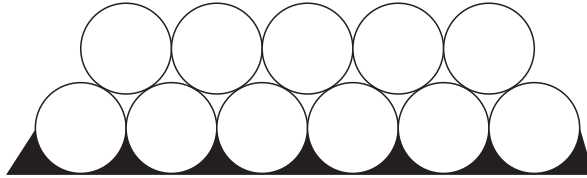


Fig. 1. Coated porous media sample geometry

Table 1

Results of thermal conductivity of experimental tests

d [m]	ρ [kg/m ³]	k [m ² /s]	λ [W/mK]
$7.5 \cdot 10^{-4}$	651	$4.05 \cdot 10^{-7}$	0.504
$7.5 \cdot 10^{-4}$	691	$3.21 \cdot 10^{-7}$	0.530
$8.5 \cdot 10^{-4}$	667	$2.95 \cdot 10^{-7}$	0.429
$8.5 \cdot 10^{-4}$	682	$3.03 \cdot 10^{-7}$	0.488
$9.0 \cdot 10^{-4}$	452	$2.49 \cdot 10^{-7}$	0.350
$9.0 \cdot 10^{-4}$	561	$2.07 \cdot 10^{-7}$	0.323

Fuzzy Logic modelling constitutes one of the calculation algorithms of the artificial intelligence. This model uses attribution operation of linguistic variables to fuzzy sets in order to qualitative evaluation of the considered process. To perform the model, input parameters should be covered by the fuzzy sets F , where numeric value of parameter corresponds to membership degree from the range of [0,1], which can be expressed by the Zadeh's notation (KRZYWANSKI et al. 2018b):

$$F = \left\{ \frac{\mu_F(i_1)}{i_1} + \frac{\mu_F(i_2)}{i_2} + \dots + \frac{\mu_F(i_n)}{i_n} \right\} \tag{2}$$

where:

i_1, i_2, i_n are input parameters and μ_F degree of membership to fuzzy set.

The main parts of a FL model are the fuzzifier, fuzzy rule base, the inference engine and defuzzifier. Further detailed information about the algorithms implemented in QtFuzzyLite software can be found in (KRZYWANSKI et al. 2018b, 2016b, BŁASZCZUK, KRZYWANSKI 2017).

In this case, the arithmetic average of particle distribution d , density ρ of coated sample, their thermal diffusivity k constitute input parameters to which linguistic terms were assigned. The selection of input parameters is related to the used thermal conductivity measurement method. LFM MicroFlash apparatus directly measures the thermal diffusivity of porous media. Thermal conductivity is calculated based on the relationship (FODEMSKI 2001):

$$k = \frac{\lambda}{\rho \cdot c_p} \quad [\text{m}^2/\text{s}] \tag{3}$$

The output parameter is the analysed thermal conductivity of a coated sorbent layer. The FL model was built in QtFuzzyLite™ 6 software. Based on experimental results, the fuzzy rule base was prepared according to Table 2. This base describes the influence of each parameter on the value of a coated sorbent layer’s thermal conductivity. The detailed description of the methodology can be found in (KRZYWANSKI, NOWAK 2016).

Table 2

Fuzzy rule base: L – low, M – medium, H – high

λ [W/mK]	L	M	H
d [μm]	H	M	L
ρ [kg/m^3]	L	H	H
k [mm^2/s]	L	H	H

Results and discussion

The input data are assigned to three overlapping triangle linguistic variables of low (L), medium (M), high (H). The same linguistic variables were used to depict values of thermal conductivity λ at the output. The membership of each variable to fuzzy sets for the input data is shown in Figure 2. The triangular functions were employed as they are the simplest and most widely used.

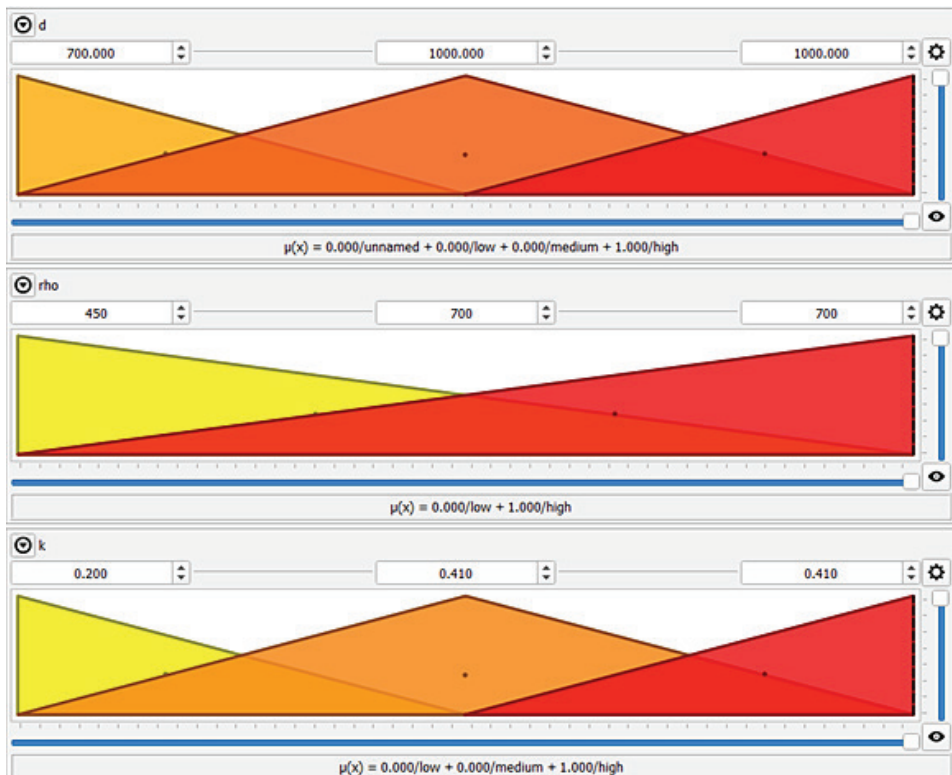


Fig. 2. Input data block with linguistic terms, where d is the arithmetic average of particle distribution, ρ is density of coated sample and k is their thermal diffusivity

The same approach was used in (DRAGOJLOVIC et al. 2001, KUCUKALI, BARIS 2010, KRZYWANSKI, NOWAK, 2016a). The membership of output parameter is given in Figure 3.

The comparison of obtained measured and model values of thermal conductivity is presented in Figure 4. In Table 3, the obtained results have been supplemented by the approximation error. The maximum relative errors are located within the range of $\pm 5\%$ with reference to the measured data. As shown, the developed fuzzy logic model has very good consistency with the experimental measurements.

The developed model was applied to predict thermal conductivity depending on the granulation and thermal diffusivity of a sorbent layer. The results of modelling are shown in Figure 5.

The calculations confirm that the thermal conductivity of the porous media layer strongly depends on arithmetic average of particle distribution. The sorbent layer with smaller granulation is characterized by much smaller amounts of gaseous spaces which significantly improves conductivity

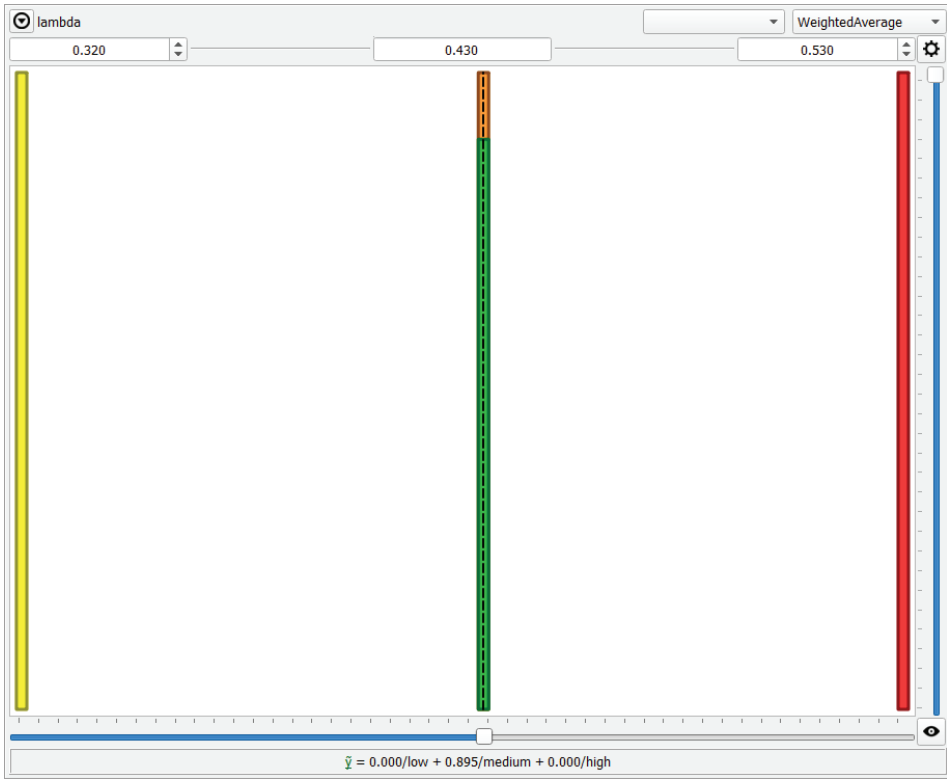


Fig. 3. Output data block with linguistic terms, where lambda is the thermal conductivity of a coated sorbent layer

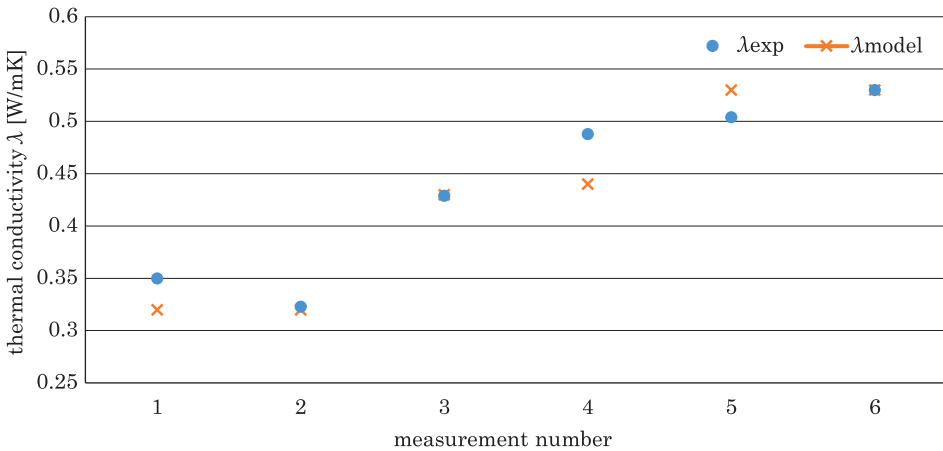


Fig. 4. Comparison of obtained measured and model values of thermal conductivity

Table 3.

Results calculated by the FL model with marked of maximum error			
No	$\lambda_{\text{experimental}}$ [W/mK]	λ_{model} [W/mK]	Error [%]
1	0.35	0.32	3
2	0.323	0.32	0.3
3	0.429	0.43	0.1
4	0.488	0.44	4.8
5	0.504	0.53	2.6
6	0.53	0.53	0

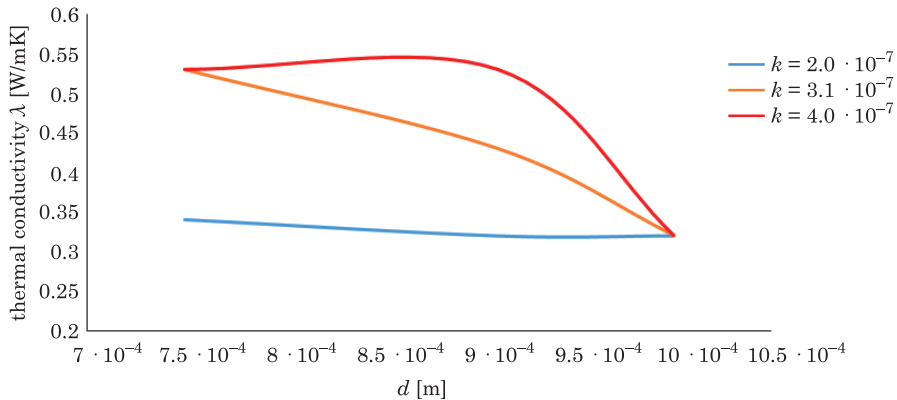


Fig. 5. Predicted values of thermal conductivity in function of d [m] for different amount of k [m^2/s]; $\rho = 560$ [kg/m^3]

of the considered bed layer. One of the methods of heat transfer intensification is the use of a glue layer which increases thermal diffusivity of the porous media layer. This solution is applied in the coated construction of adsorption beds.

Conclusions

The aim of this paper was to introduce the fuzzy logic methods to the analysis of heat transfer in a coated layer of porous media. The FL model was built to calculate the values of thermal conductivity. The differences in the obtained results were lower than $\pm 5\%$. Therefore, the model's compatibility with measured data is very good. The fuzzy logic method can be very useful in the prediction of sorbent layer thermal parameters and optimization of working conditions for an adsorption bed. The developed model allows optimization of adsorption bed configuration leading to increased thermal conductivity of the considered adsorption bed. However, in this case, the number of measurements is too low to extrapolate the model to a wider range of porous media thermal conductivity.

References

- ASKALANY A.A., HENNINGER S.K., GHAZY M., SAHA B.B. 2017. *Effect of improving thermal conductivity of the adsorbent on performance of adsorption cooling system*. Applied Thermal Engineering, 110: 695–702.
- BLASZCZUK A., KRZYWAŃSKI J. 2017. *A comparison of fuzzy logic and cluster renewal approaches for heat transfer modeling in a 1296 t/h CFB boiler with low level of flue gas recirculation*. Archives of Thermodynamics, 3(1): 91–122.
- CHOROWSKI M., PYRKA P. 2015. *Modelling and experimental investigation of an adsorption chiller using low-temperature heat from cogeneration*. Energy, 92: 221–229.
- DRAGOJLOVIC Z., KAMINSKI D.A., JUNTAEK R. 2001. *Tuning of a fuzzy rule set for controlling convergence of a CFD solver in turbulent flow*. International Journal of Heat and Mass Transfer, 44(20): 3811–3822.
- FERREIRA L.M., CASTRO J.A.M., RODRIGUES A.E. 2002. *An analytical and experimental study of heat transfer in fixed bed*. International Journal of Heat and Mass Transfer, (45)5: 951–961.
- FODEMSKI T. 2001. *Pomiar ciepłoty. Część 1. Podstawowe pomiary ciepłoty*. Wydawnictwo Naukowo-Techniczne, Warszawa.
- FRENI A., RUSSO F., VASTA S., TOKAREV M., ARISTOV Y.I., RESTUCCIA G. 2007. *An advanced solid sorption chiller using SWS-1LL*. Applied Thermal Engineering, 27(13): 2200–2204.
- GRABOWSKA K., KRZYWAŃSKI J., NOWAK W., WESOŁOWSKA M. 2018a. *Construction of an innovative adsorbent bed configuration in the adsorption chiller – Selection criteria for effective sorbent-glue pair*. Energy, 151: 317–323.
- GRABOWSKA K., SOSNOWSKI M., KRZYWAŃSKI J., SZTEKLER K., KALAWA W., ZYLKA A., NOWAK W. 2018b. *Analysis of heat transfer in a coated bed of an adsorption chiller*. XI International Conference on Computational Heat, Mass and Momentum Transfer, Krakow.
- HE T.T., UKIL A. 2016. *Design of Fuzzy Logic based Controller for Energy Efficient Operation in Building*. Proceedings of the Iecon 2016 – 42nd Annual Conference of the Ieee Industrial Electronics Society, p. 90–95.
- KUCUKALI S., BARIS K. 2010. *Turkey's short-term gross annual electricity demand forecast by fuzzy logic approach*. Energy Policy, 38(5): 2438–2445.
- KRZYWAŃSKI J., GRABOWSKA K., SOSNOWSKI M., SZTEKLER K., KALAWA W., ZYLKA A., WOJCIK T., NOWAK W. 2018a. *Modeling of re-heat two-stage adsorption chiller by AI approach*. XI International Conference on Computational Heat, Mass and Momentum Transfer (ICCHMT), Krakow.
- KRZYWAŃSKI J., WESOŁOWSKA M., BLASZCZUK A., MAJCHRZAK A., KOMOROWSKI M., NOWAK W. 2018b. *Fuzzy logic and bed-to-wall heat transfer in a large-scale CFBC*. International Journal of Numerical Methods for Heat & Fluid Flow, 28(1): 254–266.
- KRZYWAŃSKI J., GRABOWSKA K., HERMAN F., PYRKA P., SOSNOWSKI M., PRAUZNER T., NOWAK W. 2017. *Optimization of a three-bed adsorption chiller by genetic algorithms and neural networks*. Energy Conversion and Management, 153: 313–322.
- KRZYWAŃSKI J., NOWAK W. 2016a. *Modeling of bed-to-wall heat transfer coefficient in a large-scale CFBC by fuzzy logic approach*. International Journal of Heat and Mass Transfer, 94: 327–334.
- KRZYWAŃSKI J., WESOŁOWSKA M., BLASZCZUK A., MAJCHRZAK A., KOMOROWSKI M., NOWAK W. 2016b. *The Non-Iterative Estimation of Bed-to-Wall Heat Transfer Coefficient in a CFBC by Fuzzy Logic Methods*. Procedia Engineering, 157: 66–71.
- REZK A., AL-DADAH R.K., MAHMOUD S., ELSAYED A. 2013. *Effects of contact resistance and metal additives in finned-tube adsorbent beds on the performance of silica gel/water adsorption chiller*. Applied Thermal Engineering, 53(2): 278–284.
- ROGALA Z. 2017. *Adsorption chiller using flat-tube adsorbers – Performance assessment and optimization*. Applied Thermal Engineering, 121: 431–442.

- ROUHANI M., HUTTEMA W., BAHRAMI M. 2018. *Effective thermal conductivity of packed bed adsorbers. Part 1. Experimental study*. International Journal of Heat and Mass Transfer, 123: 1204–1211.
- SHARAFIAN A., FAYAZMANESH K., MCCAGUE C., BAHRAMI M. 2014. *Thermal conductivity and contact resistance of mesoporous silica gel adsorbents bound with polyvinylpyrrolidone in contact with a metallic substrate for adsorption cooling system applications*. International Journal of Heat and Mass Transfer, 79: 64–71.
- SOSNOWSKI M. 2017. *Computational domain discretization in numerical analysis of flow within granular materials*. The European Physical Journal Conferences, 180(2): 582–588
- SOBOLEWSKI M., GRZESIK N., KORUBA Z., NOWICKI M. 2016. *Fuzzy logic estimator implemented in observation-tracking device control*. Aircraft Engineering and Aerospace Technology, 88(6): 697–706.
- SZTEKLER K., KALAWA W., NOWAK W., STEFAŃSKI S., KRZYWANSKI J., GRABOWSKA K. 2017. *Using the adsorption chillers for utilisation of waste heat from rotary kilns*. International Conference on Experimental Fluid Mechanics (EFM), Mikulov, Czech Republic, p. 650–653.
- ZHU D.S., WANG S.W. 2002. *Experimental investigation of contact resistance in adsorber of solar adsorption refrigeration*. Solar Energy, 73(3): 177–185.



Quarterly peer-reviewed scientific journal

ISSN 1505-4675
e-ISSN 2083-4527

TECHNICAL SCIENCES

Homepage: www.uwm.edu.pl/techsci/



WEATHER AND A PART OF DAY RECOGNITION IN THE PHOTOS USING A KNN METHODOLOGY

Tomasz Krzywicki

Faculty of Mathematics and Computer Science
University of Warmia and Mazury
Polish Information Processing Society

Received 18 May 2018; accepted 16 November 2018; available online 21 November 2018.

Key words: weather recognition, image analysis, machine learning, classification.

Abstract

This article presents a proposal for recognizing the weather and part of a day in digital photos encoded in the bitmap format, based on auctorial edge detection algorithm of horizon to demarcate the sky and k-nearest neighbours algorithm, to classify the daytime in the picture as “day” or “night” and to classify the weather as “sunny” or “cloudy”. To verify the effectiveness of the classification the Internal Bagging-5 model was applied. The data for surveys in the form of pictures was prepared on self-provision. To test the method in a different location, data from the Internet was used.

Introduction

Recognizing the weather based on the bitmap is difficult. There is a lack of basic sensory information which reflecting the actual weather as: temperature [°C], pressure [hPa], wind speed [m/s], downfall [mm/h], dampness [%], etc. The work's aim is to propose the methods to analyze the picture and determine part of a day as “day” or “night”, also determining the weather as “sunny” or “cloudy”. The proposed solution was based on machine learning method – k-nearest neighbours (kNN) to learn the computer's system weather recognizing in virtue of the examples in the form of 24-bitmap photos.

Correspondence: Piotr Artiemjew, Katedra Metod Matematycznych Informatyki, Uniwersytet Warmińsko-Mazurski, ul. Słoneczna 54, 10-710 Olsztyn, phone: 89 524 60 82, e-mail: tomasz.krzywicki@student.uwm.edu.pl

The inspiration to formulating the solution was trying to find the algorithms which automatically tag images, including significant surface of the sky. The method performance was determined with fivefold Internal Bagging-5 test. The results were presented as an average value of all tests. The solution has achieved a satisfactory effectiveness.

The picture exploration analysis

The photos which were used during the experiments were taken in Bartoszyce (Poland) by Microsoft LifeCam HD-3000 camera, within a period from 29th August 2017 to 7th September 2017, with a common frame. Photos confirming the effectiveness of the method used were taken in Le Morne (Mauritius), within a period 7th October 2018 to 6th November 2018, with a common frame.

The daytime characteristics

The part of a day is a time between sunrise and sunset. In the picture, in the RGB colour space, the daytime will be determining in the sum number ratio of red and green colour to blue colour, also the average intensity of pixel level. The pixel intensity should be understood as a brightness in shades of grey, in the field of $\langle 0;255 \rangle$, where the value 0 is the lowest pixel intensity (black colour) and the value 255 is the highest (white colour). The part of a day classification will be automatically after learning the model method k-nearest neighbours.

The sum number ratio parameter of colours was formulated as

$$\frac{R + G}{B},$$

where:

- R – the red colour sum number in the picture,
- G – the green colour sum number in the picture,
- B – the blue sum number in the picture.

The average pixel intensity parameter was formulated as

$$\frac{R + G + B}{3},$$

where:

- R – the colour sum number in the picture,
- G – the green colour sum number in the picture,
- B – the blue sum number in the picture.

The graphic presentation of the layout pixel colours for the photos which were taken during the day and the night, were presented with the histograms (Figs. 1, 2).

The picture's histogram shows that during the day, it can be noticed, for example, for the value 100, the red colour occurred about 1,000 times. In the picture which was taken during the night, number of red colour pixels with intensity 100 was about 3,000. Analysing the colour distribution in RGB photos taken during the day and the night surface, the differences are noticeable. In the picture taken at night towards the picture taken during the day the intensity of blue colour is increasing, the intensity of red and green colour is falling.

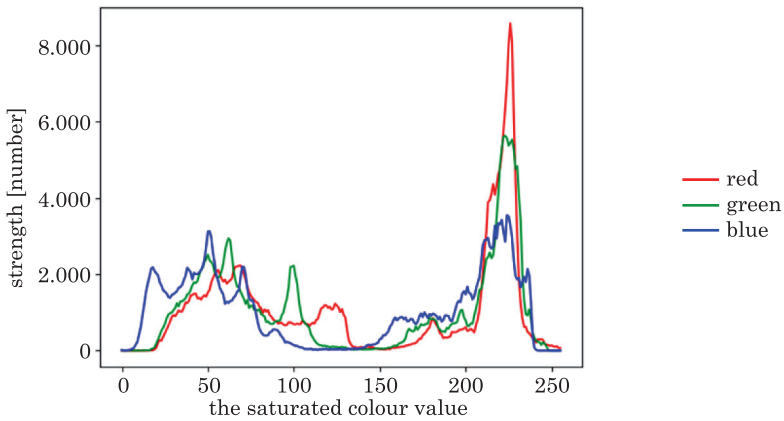


Fig. 1. The distribution of RGB values in the picture taken during the day

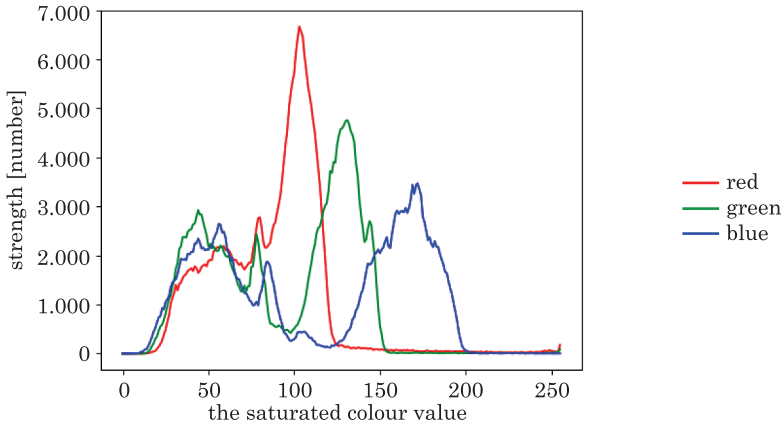


Fig. 2. The distribution of RGB values in the picture taken during the night

The picture histograms' observation taken every minute around the dusk, permitted to see that the sum number ratio parameter of colours and the average pixel intensity is decreasing around the dark (Fig. 3).

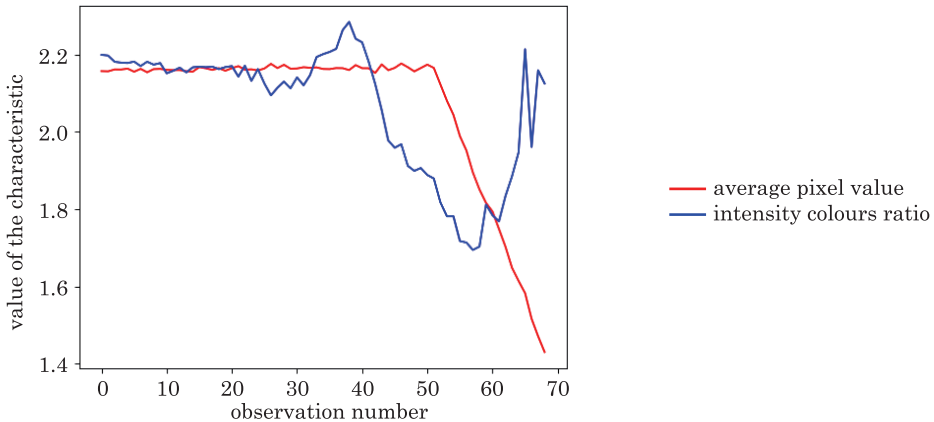


Fig. 3. Parameters' change in picture value along with night coming on

For the sake of clarity presented data, the intensity colour parameter ratio (coloured blue) was rescaled with a common logarithm. Each of the following observation number means a taken photo a minute later. It can be noticeable that from the moment when the night is coming on, the plurality of pixels is dark colour, whereby the parameter which is the ratio of colours number sum, is increasing again, as can be seen around the 60 minute of observation.

Weather characteristics

Intuitively, the sunny weather is seen as an under partly cloudy blue sky. The cloudy weather means no blue colour on the sky.

Empirically, it was noticed, that red colour doesn't influence on classifying the sunny or cloudy weather in the bitmap picture of the sky. Let us adopt that the sum number ratio of blue to green colour above the horizon's edge (the algorithm of detecting the horizon's edge was described in the next subsection) is a parameter which characterises the weather classification, it was formulated by B/G , where B is the sum number of blue colour, G is the sum number of green colour.

The pixel number ratio of higher intensity from the threshold level set of lower intensity from the threshold level, it will be called as a picture dichotomy. By taking threshold value 128, which is the middle range of set values by

the pixel in the picture, in the scale of grey, it was noticed that the picture dichotomy taken during the sunny weather is higher than the dichotomy picture taken during the cloudy weather. Table 1 includes the parameters' values of pictures taken during the sunny and cloudy weather.

Table 1

Parameter values of pictures taken during the sunny and cloudy weather			
Taken photo time	Weather	B/G	Dichotomy
28.08.2017 6:34 pm	sunny	1.281	1.643
29.08.2017 6:43 pm	sunny	1.124	1.608
29.08.2017 6:40 pm	sunny	1.154	1.499
29.08.2017 7:04 pm	sunny	1.011	1.206
01.09.2017 12:29 am	cloudy	0.960	1.109
01.09.2017 1:01 pm	cloudy	0.962	1.103
06.09.2017 12:11 am	cloudy	0.966	0.966
06.09.2017 6:57 pm	cloudy	0.970	0.810

The parameter values, which characterise the weather in the picture taken during the sunny weather are higher than the parameter values, which characterise the weather in the picture during the cloudy weather.

The edge of the horizon demodulation

With the aim of determination the edge of the horizon, it is necessary to determine outlines all of the subsets presented in the picture. Sobel (KAEHLER, BRADSKI 2017) operator shall produce the outlines in the picture in shades of grey, which as used during the determining the edge of the horizon. It was noticed that the pixels of outside edge contour, most commonly have their values at least threefold higher than average pixels values outline. For our purposes, the horizon will be called as lower edge of the sky outline (subset).

Determining edge of the horizon in the picture rely on finding the threshold value which is a lower limit (infimum). In order to analyse the weather, the land was divided from the sky. To that end, the function called `get_threshold` was constructed, its aim is to count three times the average pixel intensity of outline. Due to that function, the lower limit of the sky was determined. By means of `get_threshold` (Fig. 4) function, the edge of the horizon was determined, by creating `get_horizon_edge` (Fig. 5) function.

```
function get_threshold(image)
    sum_values = 0
    pixel_count = 0
    for i = 0 to image.height-1 do
        for j=0 to image.width-1 do
            if image[i][j] > 0 then
                sum_values += image[i][j]
                pixel_count += 1
            endif
        endfor
    endfor
    return round((sum_values/pixel_count)*3)
endfunction
```

Fig. 4. Function calculating three times the average pixel intensity

```
function get_horizon_edge(image, threshold)
    horizon_edge = []
    for i = 1 to image.width-2 do
        j = 1
        while j < image.height-1 and obraz[j][i] <= threshold do
            j += 1
        endwhile
        horizon_edge.append(new Point(i, j))
    endfor
endfunction
```

Fig. 5. Function dividing the land from the sky

The function called `get_horizon_edge` (Fig. 5) determines from the designated picture pixels list, which establish the horizon. In Figures 6 and 7 are original photos before and after the operation of the `get_horizon_edge` function result. In Figure 6 is noticeable an original photo, in Figure 7 is symbolically pixels list of the horizon.



Fig. 6. An exemplary photo showing the horizon covered by trees

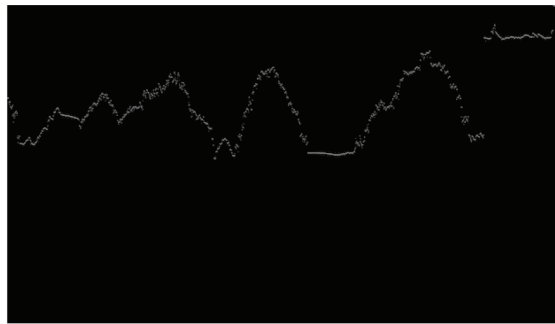


Fig. 7. Symbolically pixels list affixed to the photo horizon number 1

The detection algorithm of the horizon edge has disadvantages, which can negatively influence on the parameter values of current weather in the picture. When analysing photos both light-struck and low resolution, also overly contrasty, it was noticed, that the edge of the horizon is not always being determined well. The list of horizon dots determined with `get_horizon_edge` sometimes has deviated from some pixels under or above a real horizon line.

kNN algorithm

The kNN algorithm (k-nearest neighbours) is a machine model learning which facilitates multiclass classification. The kNN model belongs to lazy classifier- learning from the examples. The kNN algorithm working principle is performed by checking only k objects in the training set, which features in the expanse are close to classified object as possible. Basing on just founded k-similar objects the decision-making class is chosen, which total weight is the best. The kNN algorithm needs two parameters: k-nearest neighbours number and a metric to assess proximity of objects.

Selected metric remoteness

The most common measure of distance is Euclidean metric, used in scores of kNN algorithm implementation as default. Euclides distance of two objects is formulated as:

$$d(x, y) = \sqrt{\sum_{i=1}^n (a_i(x) - a_i(y))^2},$$

where:

- $d(x, y)$ – Euclidean distance in n -dimensional space of real numbers,
- $a_i(x)$ – the value of i coordinate – that x object's point in n -dimensional space of real numbers,
- $a_i(y)$ – the value of i coordinate – that y object's point in n -dimensional space of real numbers.

Manhattan metric is a metric used in the cities, where a grid system of streets run north-south and east-west. The distance determined as Manhattan metric is the sum of the absolute differences coordinate points' values in space, which is formulated as:

$$d(x, y) = \sum_{i=1}^n (a_i(x) - a_i(y)),$$

where:

- $d(x, y)$ – Manhattan distance in n -dimensional space of real numbers,
- $a_i(x)$ – the value of i coordinate – that x object's point in n -dimensional space of real numbers,
- $a_i(y)$ – the value of i coordinate – that y object's point in n -dimensional space of real numbers.

Chebyshev metric is a distance metric used in chess game, in determining the minimum number of moves, to go from one square to another one. Chebyshev distance is formulated as:

$$d(x, y) = \max. (|a_i(x) - a_i(y)|), \text{ for } i = 1, 2, \dots, n,$$

where:

- $d(x, y)$ – Chebyshev distance in n -dimensional space of real numbers,
- $a_i(x)$ – the value of i coordinate – that x object's point in n -dimensional space of real numbers,
- $a_i(y)$ – the value of i coordinate – that y object's point in n -dimensional space of real numbers.

General kNN algorithm procedure:

- loading test system (X, A, c) and training system (Y, A, c) , where: X is objects testing set, Y is objects training set, A is conditional objects' features, c is a class objects set;
- the d metric's choice of counting the distance between objects and k-nearest neighbours number;
- the classification of all tested objects by using k-nearest objects, for each of the training objects' class set – the decision is a class, which objects are the closest to tested object, based on before stated d metric.

Testing classifier efficiency

As the result method of classifier efficiency there was chosen Internal Bagging-5 method, which is based on frequentative Bagging method's carrying out, in training set to matching the most effective parameter of k-nearest neighbours number, and then checking the classification effectiveness in testing set. The each test results are averaged out, which gives classifier's estimate effectiveness better and closer to reality.

Bagging

The foundation of Bagging method is repeated performing Bootstrap test. The each test results are levered (ARTIEMJEW 2016).

In Bootstrap method from n -objects set of original decision – making system, selecting at random is restored of n -objects, which are the training set. It is easy to spot that not all of the objects will be chosen, the other ones will appear over and over again. Following that procedure there is a chance that in the training set the same objects will be many a time. In case of appearing an empty test set, we repeat its draw. The Bootstrap method gives inaccurate, perfunctory evaluation of classifiers effectiveness, contingent on random, a single split on training and testing set (ARTIEMJEW 2016).

Results discussion

During the survey there were taken 2,611 photographs. There were randomly chosen of 1,000 photos showing a day and a night, sunny and cloudy weather, with shared of 500 photos for each *class*. In Figures 8 and 9 is performed a parameters visualization for 1,000 objects of a daytime and 1,000 weather's objects.

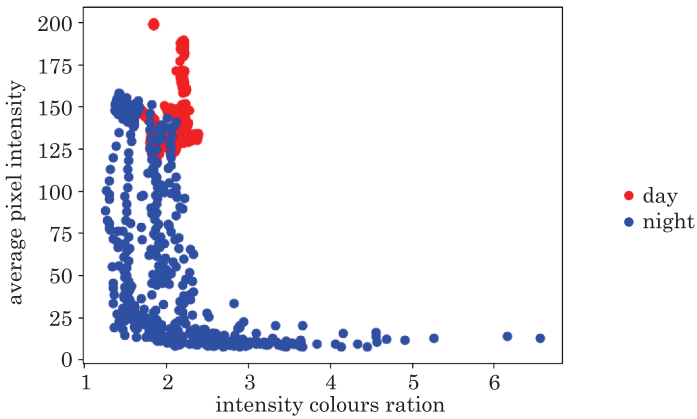


Fig. 8. Visualisation of a daytime parameters

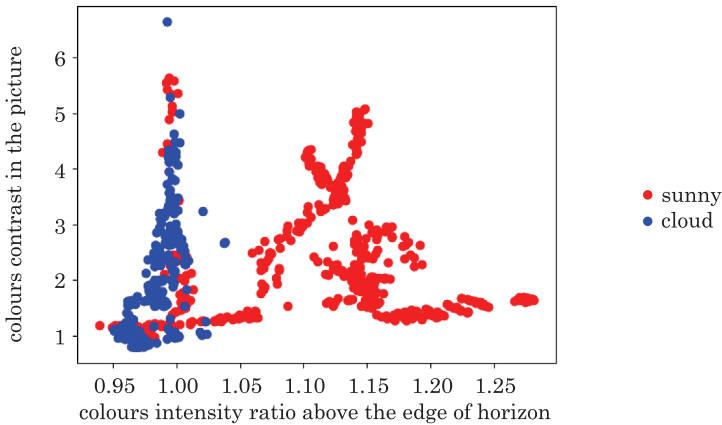


Fig. 9. Visualisation of weather parameters

The parameter values for day and cloudy weather are more focused rather than for night and sunny weather (Fig. 8, 9).

The kNN validation model with Euclidean distance metric for recognising a part of a day and weather in the photos, was done by using fivefold Internal Bagging-5 method test, on 1,000 objects containing daytime parameters and on 1,000 objects containing weather parameters, with fives k -parameter (Tabs. 2, 3). After the test, results are presented in Table 4.

Table 2

Parameter's fives used during the daytime classifier test by Internal Bagging-5 method

Part of a day					
Test number	<i>k</i> 1	<i>k</i> 2	<i>k</i> 3	<i>k</i> 4	<i>k</i> 5
Test 1	<i>k</i> 1=2	<i>k</i> 2=2	<i>k</i> 3=4	<i>k</i> 4=2	<i>k</i> 5=2
Test 2	<i>k</i> 1=3	<i>k</i> 2=2	<i>k</i> 3=2	<i>k</i> 4=2	<i>k</i> 5=2
Test 3	<i>k</i> 1=2	<i>k</i> 2=2	<i>k</i> 3=2	<i>k</i> 4=2	<i>k</i> 5=2
Test 4	<i>k</i> 1=4	<i>k</i> 2=2	<i>k</i> 3=3	<i>k</i> 4=2	<i>k</i> 5=2
Test 5	<i>k</i> 1=2	<i>k</i> 2=4	<i>k</i> 3=2	<i>k</i> 4=2	<i>k</i> 5=2

Table 3

k parameter's five used during the Feather classifier test by Internal Bagging-5 method

Weather					
Test number	<i>k</i> 1	<i>k</i> 2	<i>k</i> 3	<i>k</i> 4	<i>k</i> 5
Test 1	<i>k</i> 1=3	<i>k</i> 2=2	<i>k</i> 3=2	<i>k</i> 4=2	<i>k</i> 5=2
Test 2	<i>k</i> 1=3	<i>k</i> 2=2	<i>k</i> 3=2	<i>k</i> 4=2	<i>k</i> 5=2
Test 3	<i>k</i> 1=2	<i>k</i> 2=2	<i>k</i> 3=2	<i>k</i> 4=2	<i>k</i> 5=2
Test 4	<i>k</i> 1=3	<i>k</i> 2=2	<i>k</i> 3=2	<i>k</i> 4=2	<i>k</i> 5=4
Test 5	<i>k</i> 1=2	<i>k</i> 2=2	<i>k</i> 3=2	<i>k</i> 4=2	<i>k</i> 5=2

Table 4

Test results of daytime and weather classifier by Internal Bagging method

Type of problem	Arithmetic average	Standard deviation
Part of a day	0.943548097603988	0.010142184895868
Weather	0.958484382006594	0.008661892051049

709 photos from different location were used to confirm the effectiveness of the method. There were randomly chosen of 300 photos showing a day and a night, sunny and cloudy weather, with shared of 75 photos for each class.

For the data checking the effectiveness of the method, the test Internal Bagging-5 was performed again. The results are presented in Table 5.

Table 5

Test results of daytime and weather classifier by Internal Bagging method in the different location

Type of problem	Arithmetic average	Standard deviation	The most common <i>k</i>
Part of a day	0.991473908231302	0.005949486731013	2
Weather	0.911436556374957	0.030718308098330	3

Conclusions

A key aim of the article was to performance a proposal of recognizing a part of a day and the weather, based on the learning machine algorithm k-nearest neighbours, in virtue of digital photos containing significant sky surface. Also, there was shown the new approach to the edge of the horizon detection in the picture, noted for Adobe Photoshop.

The suggested solution has achieved a satisfactory effectiveness, confirmed by fivefold Internal Bagging-5 test: about 94% to daytime classification and about 96% to weather classification. The suggested solution in the different location has also achieved a satisfactory effectiveness, confirmed by fivefold Internal Bagging-5 test: about 99% to daytime classification and about 91% to weather classification.

Future works

In the future it is planned to check effectiveness in other locations and at different times of the year. For this purpose photos from locations: North and South Europe, Central Africa, Eastern Asia are collected.

In the future is also planned a comprasion of the proposed method with other solutions performing similar tasks.

References

- ARTIEMJEW P. 2016. *Wybrane paradygmaty sztucznej inteligencji*. PJATK Publishing House, Warszawa.
- ESPOSITO R., SAIITA L. 2003. *Monte Carlo Theory as an Explanation of Bagging and Boosting*. Proceedings of the Eighteenth International Joint Conference on Artificial Intelligence IJCAI-03 Contents al and Data Integration, p. 499–504, <http://www.ijcai.org/Proceedings/03/Papers/074.pdf> (access: 27.01.2018).
- KAEHLER A., BRADSKI G. 2017. *OpenCV 3. Komputerowe rozpoznawanie obrazu w C++ przy użyciu biblioteki OpenCV*. Helion Publishing House, Gliwice.
- LEMMENS A., CROUX C. 2006. *Bagging and Boosting Classification Trees to Predict Churn*. <http://citeseerx.ist.psu.edu/viewdoc/download?doi=10.1.1.196.6659&rep=rep1&type=pdf> (access: 9.02.2018).
- MACHOVÁ K., BARČÁK F., BEDNÁR P. 2006. *A Bagging Method using Decision Trees in the Role of Base Classifiers*. http://people.tuke.sk/kristina.machova/pdf/bagging_o6.pdf (access: 12.04.2018).
- MOLINARO A.M., SIMON R., PFEIFFER R.M. 2005. *Prediction error estimation. a comparison of resampling methods*. *Bioinformatics*, 21(15): 3301–3307.



Quarterly peer-reviewed scientific journal

ISSN 1505-4675
e-ISSN 2083-4527

TECHNICAL SCIENCES

Homepage: www.uwm.edu.pl/techsci/



IMPACT OF FRICTION COEFFICIENT ON PARTICLES CIRCULATION VELOCITY CALCULATED BY EULER-LAGRANGE MODEL IN SPOUTED BED APPARATUS FOR DRY COATING

Wojciech Ludwig

Department of Chemical Engineering
Faculty of Chemistry
Wroclaw University of Technology

Received 14 May 2018; accepted 20 November 2018; available online 21 November 2018.

Key words: spout-fluid bed, friction coefficient, restitution coefficient, Euler-Lagrange approach.

Abstract

This paper is a continuation of research concerning gas-solid flow modelling using the Euler-Lagrange approach in a spout-fluid bed apparatus. The major challenge in this case was to determine the friction coefficient for particles hitting against the walls of the apparatus. On the basis of the properties of similar materials the value of this quantity was estimated at 0.2. Therefore, it proved useful to check the model's sensitivity to the value of this parameter. The study investigated the effect of friction coefficient on calculated values of particles velocity in the draft tube and the annular zone of the device for various volumes of the circulating bed. In the course of calculations, a relatively small influence of friction coefficient on particles velocity was observed in the tested zones of the apparatus. The changes were most visible for large volumes of the bed, which was connected with an increase in the number of collisions of particles with the walls.

Symbols

- a – coefficient of Morsi-Alexander drag law, –
- a_s – particle acceleration, m/s^2 ,
- c – coefficients of e_t correlation, –
- C_D – drag coefficient, –
- d – particle diameter, m,

Correspondence: Wojciech Ludwig, Zakład Inżynierii Chemicznej, Wydział Chemiczny, Politechnika Wroclawska, ul. Norwida 4/6, 50-373 Wrocław, e-mail: wojciech.ludwig@pwr.edu.pl

e	– restitution coefficient, –,
E^*	– effective Young’s modulus for impact of two materials, Pa,
$F_{\text{interaction}}$	– averaged force of momentum exchange between phases per unit volume, N/m^3 ,
$F_{\text{exchange},i}$	– force of momentum exchange between fluid and individual particle per unit mass, N/kg ,
g	– gravitational acceleration, m/s^2 ,
H	– height of the fixed bed, m
I	– unit vector
m	– mass, kg.
m^*	– effective mass for impact of two materials, Pa,
P	– pressure, Pa,
R^*	– effective radius for impact of two materials, m
Re	– relative Reynolds number, –,
S_g	– deformation rate tensor of fluid phase
u_g	– velocity vector of fluid phase, m/s
$u_{s,i}$	– velocity vector of individual solid particle, m/s
$V_{s,i}$	– velocity component, m/s, volume, m^3 ,
w	– average velocity, m/s
x	– coordinate vector (x, y, z)

Greek letters

β	– momentum transfer coefficient, –
η	– dynamic viscosity of the fluid, $\text{Pa}\cdot\text{s}$,
θ_i	– incident angle according to WU et al. (2007),
$(\theta_i)_{\text{Fluent}}$	– incident angle according to ANSYS Fluent software, °,
Θ	– nondimensional angle of incident, –,
Θ_{crit}	– critical value of nondimensional angle Θ , –,
κ	– rigidity coefficient, –,
λ	– kinetic energy loss ratio, –,
μ	– friction factor, –,
ρ	– density, kg/m^3 ,
τ_g	– stress tensor of fluid phase
ω	– volume fraction, m^3/m^3 .

Subscripts

bed	bed
elast	elastic
g	gas
i	incident
n	normal
o	inlet
r	rebound
s	solid
t	tangential
Thornton	from Thornton’s model
y	yield

Introduction

Spouting apparatuses were created as a modification of classic fluidized bed devices (MATHUR, GISHLER 1955). They eliminated their basic disadvantage, i.e. the possibility to use only small particles (SUTKAR et al. 2013). They enabled operations on beds of materials with diameters of up to several millimetres (Geldart's class *D*) (GELDART 1973). This is related to the unique characteristics of the bed flow in such devices (EPSTEIN, GRACE 2011, MOLINER et al. 2017). The gas, which is fed only through the hole in the axis of the device, lifts the particles in the so-called spout zone. Then they form a spout above the surface of the bed and fall freely into the annular zone (annulus), where they are entrained again to the spout zone. Taking into account the movement of particles, the two zones differ considerably. In the central part, we are dealing with pneumatic transport, high flow velocities of both phases and a small volume fraction of solids. On the contrary, in the annular zone, a slowly moving packed bed is created. Due to this mode of operation the spouting devices have been used from the very beginning in many areas of the economy (EPSTEIN, GRACE 2011, MOLINER et al. 2017). Spouting is widely used for drying sticky materials, e.g. pastes, sludge and grains with high moisture content, and in the food industry for dehydrating fruit and vegetables. This type of devices is also used for pyrolysis, combustion and gasification of waste materials, e.g. biomass, post-production sludge, used plastics and tyres. The ordered movement of particles compared to the fluidized bed makes the spouting devices ideal for coating in both the pharmaceutical and food industries (TEUNOU, PONCELET 2002). A coating layer is applied in the spout zone and the material is dried in the annular zone. In classic spouting devices, particles are entrained into the spout zone from any point in the annular zone, which results in varying humidity and a random distribution of the coating times (ZHONG et al. 2010). The solution to this problem is the use of the draft tube that physically separates the two zones and thus organises the circulation of particles. They may only be entrained into the spout zone along a short distance between the lower edge of the tube and the bottom. In addition, the draft tube reduces the minimum spouting velocity and allows the use of high beds (no maximum spoutable bed depth) (ISHIKURA et al. 2003).

Initially, the coating was carried out in spouting apparatuses where the spray nozzle was located in the upper part of the chamber with the bed. However, both the efficiency of the process and the quality of the coating were low. Therefore, devices with a spraying nozzle located in the lower part of the bed have been introduced. In this system, the probability of collision between the particles and the coating droplets is higher and the drying time shorter, however, there is a risk of agglomeration of moistened bed particles due to their high concentration just above the nozzle. This can be prevented by using an additional stream of fluidizing air (spout-fluid bed system). Some modification of the construction

described above is the Wurster apparatus – a spout-fluid device with the draft tube and a nozzle in the bottom. It is considered to be the best design for coating of fine grain materials (TEUNOU, PONCELET 2002, KARLSSON et al. 2006).

SZAFRAN et al. (2012) presented a new spout-fluid device with internal bed circulation, which is a modification of the Wurster apparatus, in which the hydrodynamics of particle flow significantly differs from that of classic spout apparatus. Thanks to the significant elongation, the device operates in the fast circulating dilute bed regime, which is characterized by low concentrations of particles in all zones and their high speed (LUDWIG, ZAJĄC 2017). Therefore, the device is suitable for dry powder coating of materials with small grain size, even those in Geldart's Group C (GELDART 1973).

The correct description of phase flow hydrodynamics is the basis for modelling the coating process in the spouting apparatuses. Due to the intensive development of models describing multiphase flows, computational algorithms and the increase in power of computer hardware, an increasing role of computational fluid dynamics (CFD) in the modelling of spouted beds can be observed. In the case of gas-solid systems, there are two approaches: Euler-Euler (EE) and Euler-Lagrange (EL) (RANADE 2002, MOLINER et al. 2017). The first approach treats both phases as interpenetrating continua. Equations describing both phases have a similar structure, they differ only in the volume fraction of a given phase (RANADE 2002). They are solved for each phase separately. We take into account the interaction of phases through pressure and the terms called inter-phase coefficients of momentum, energy and mass exchange (LUDWIG, ZAJĄC 2017). EE models have no limitations concerning volume fraction of individual phases; they can be used in devices of any scale. Unfortunately, in their case it is necessary to develop a model describing the rheology of the dispersed phase. EE models do not provide accurate information on particle movement – we only know their volume fraction and average velocity. The calculation cost of these methods is low, so they are often used. In this case, however, it is necessary to validate the values of the model parameters, e.g. packing limit, restitution coefficient, etc. (LUDWIG, ZAJĄC 2017). These must be determined by comparing the results of the simulation with the experimental data for a given device. In relevant literature there is a lack of satisfactory data, e.g. for devices with circulating bed.

EL models describe the dynamics of the continuous phase using the cell averaged momentum transport equations (DEEN et al. 2007). The motion of the dispersed phase is modelled by solving motion equations for each of its elements individually, which entails a high demand for computational power and memory (JAWORSKI 2005). Fluidized and spouted beds are characterized by granular flows with a high volume fraction of the dispersed phase. Therefore, in EL approach such flows are most often described using DEM (Discrete Element Method) (CUNDALL, STRACK 1979). In its original form, it is insufficient to describe

the multiphase fluid-solid flows, as it does not take into account the hydrodynamic forces resulting from the momentum exchange between the fluid stream and the particles that move within it. In this case, the DEM method is combined with the CFD models: the dispersed phase is described using DEM and CFD models are used for the continuous phase (fluid). This CFD-DEM approach has become an effective tool to study the hydrodynamics of complex granular flows. Two approaches are used to describe interparticle and wall collisions: soft-sphere and hard-sphere. The soft-sphere method assumes that particles may experience microdeformation in the contact point area due to friction and stress (TSUJI et al. 1993). Deformations cause some strain, i.e. ‘numerical’ displacement of two bodies. The greater the strain, the higher the value of the contact force between the bodies. The hard-sphere method assumes that all interparticle interactions are binary and immediate (contact time is infinitely small) and that contact forces are impulsive (HOOMANS et al. 1996, WACHEM, ALMSTEDT 2003). The particles are spherical and this shape is retained after impact. The basic correlations used in this method are the balance of momentum and energy before and after the collision. The contact between the bodies is point-based and during its course they undergo normal and tangential deformations resulting from the occurring elastic forces. Particle velocities after collision are determined by the pre-collision velocities and restitution factors according to the formula:

$$e_{n,t} = \frac{V_{r\ n,t}}{V_{i\ n,t}} \quad (1)$$

When we deal with the significant low volume fraction 10^{-3} – 10^{-4} , a simplified DEM model called the Discrete Phase Model (DPM) can be used to describe the circulation of the dispersed phase, where only collisions of particles with the walls of the apparatus are taken into account. During the previous studies the author presented a model of particle-wall collision, which was successfully used to calculate the velocity of particles in the key area for coating in the modified Wurster apparatus (LUDWIG, PŁUSZKA 2018). The model assumed the use of selected Thornton and Wu equations describing respectively the normal and tangential restitution coefficient as a function of the particle velocity and the angle of its incidence on the surface from which it rebounds (THORNTON et al. 2001, WU et al. 2009). In order to be able to apply the model equations, it was necessary to know many physical properties of the circulating particles and the material of the walls (see Tab. 1). The biggest problem in this case was to determine the value of the friction coefficient of particles against the walls of the apparatus. Based on the properties of similar materials, its value was initially estimated at 0.2 (WU, SEVILLE 2016). In order to check the impact of an error in adopting this value on the correctness of calculating the particle velocity in the apparatus, an analysis was made of the dependence of the results

in the draft tube zone and the annular zone on the assumed friction coefficient value for various volumes of the bed. Data obtained from computer simulations were compared with experimental results.

Modelled apparatus

The modelled device is presented in Figures 1 and 2. Its main part is a very long column (3 m high) consisting of three cylindrical glass segments *B*, *D* and *E* and an aluminium cone *C* with air supply nozzles, a plasticiser and a coating substance, which, contrary to classical solutions, was placed between the lower segment *B* (particle acceleration zone) and the upper part *D* of the device (coating zone).

In the axes of the segments there is a glass draft tube 6, above which there is a metal deflector 8, which prevents the bed from being blown away and allows for the use of high velocities of spouting air. It is fed through the injector 10, which sucks the gas from the annular zone. The particles poured into the apparatus fall freely to the bottom of the lower segment *B*. When the spouting gas stream 1 is switched on, the particles are sucked in and accelerated to achieve the required circulation velocity, passing through cone *C* with powder nozzle 3

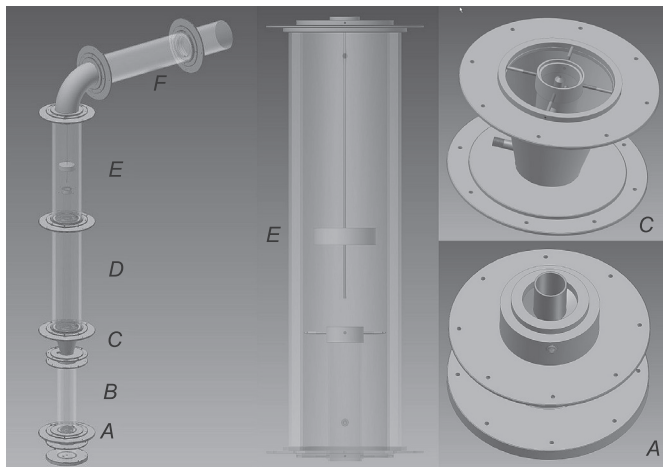


Fig. 1. Diagram of spout-fluid bed apparatus with a circulating dilute bed for dry coating: *A* – particle entrainment zone, *B* – bottom segment (acceleration zone), *C* – cone with nozzles spraying the plasticiser and coating powder, *D* – middle segment (coating zone), *E* – upper segment (spouting zone), *F* – outlet (dust extraction zone). Dimensions of the apparatus: height: 3 m, inside diameter of the lower section 0.08 m, inside diameter of the upper section: 0.15 m, length of the draft tube: 1.78 m, its inside diameter in the lower section: 0.041 m, its inside diameter in the upper section: 0.054 m
Source: based on LUDWIG and ZAJĄC (2017), LUDWIG and PŁUSZKA (2018).

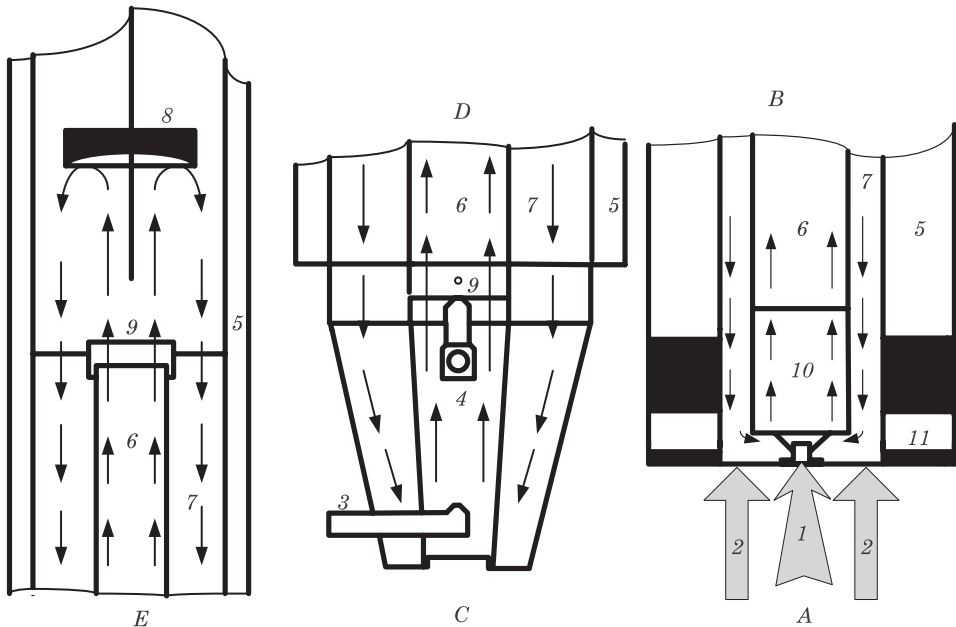


Fig. 2. Details of selected parts of the spout-fluid bed apparatus with a circulating dilute bed for dry coating (the arrows show the trajectories of the movement of the coated particles):

A – entrainment zone with the injector, *B* – bottom segment (acceleration zone),

C – cone with nozzles, *D* – middle segment (coating zone), *E* – upper segment (spouting zone);

1 – main stream of spouting air, *2* – stream of fluidizing air, *3* – powder spraying nozzle,

4 – plasticizer nozzle, *5* – double external glass wall of the apparatus, *6* – glass draft tube,

7 – annular zone (drying zone), *8* – aluminium deflector, *9* – aluminium connecting rings,

10 – metal injector, *11* – holes for bed unloading

Source: based on LUDWIG (2016).

and plasticiser nozzle 4, and then through the upper draft tube 6 in segment *D*. When they leave the draft tube, they rebound off deflector 8, fall into annular zone 7 and fall to the bottom. In entrainment zone *A*, they are sucked in again.

Model description

In Eulerian-Lagrangian modelling the flow of the continuous phase is described by means of the transport equations averaged in the calculation cell. A significant difference, in comparison to single-phase flows, is the inclusion of the volume fraction of the phase ω in the equation terms. The continuity equation is in the form (WACHEM, ALMSTEDT 2003):

$$\frac{\partial}{\partial t} (\omega_g \rho_g) + \nabla (\omega_g \rho_g u_g) = 0 \quad (2)$$

where the index g means the continuous phase (fluid). The momentum conservation equation:

$$\frac{\partial}{\partial t}(\omega_g \rho_g \mathbf{u}_g) + \nabla(\omega_g \rho_g \mathbf{u}_g \mathbf{u}_g) = -\omega_g \nabla P + \nabla(\omega_g \boldsymbol{\tau}_g) + \omega_g \rho_g \mathbf{g} + \mathbf{F}_{\text{interaction}} \quad (3)$$

contains a stress tensor $\boldsymbol{\tau}_g$ defined as:

$$\boldsymbol{\tau}_g = 2\eta S_g - \frac{2}{3}\eta S_g^T I \quad (4)$$

where η is the dynamic viscosity of the fluid, I is the unit vector, and S_g is the tensor of the deformation velocity in the continuous phase:

$$S_g = \frac{1}{2}(\nabla u_g + (\nabla u_g)^T) \quad (5)$$

In equation (3), the source term $\mathbf{F}_{\text{interaction}}$ represents the average effect of the momentum exchange between the continuous phase and all the elements of the discrete phase that are present in the control volume under investigation:

$$F_{\text{interaction}} = \frac{\sum_{i=1}^N [V_{s,i} \rho_s F_{\text{exchange},i}]}{\sum_{i=1}^N V_{s,i}} \delta \quad (6)$$

In equation (6), $V_{s,i}$ is the volume of the i -th solid particle and δ is a pulsating function:

$$\delta = f(\mathbf{x}_g - \mathbf{x}_{s,i}) = \begin{cases} 1, & (\mathbf{x}_g - \mathbf{x}_{s,i}) = 0 \\ 0, & (\mathbf{x}_g - \mathbf{x}_{s,i}) \neq 0 \end{cases} \quad (7)$$

Function $\delta = f(\mathbf{x} - \mathbf{x}_{s,i})$ ensures selective occurrence of interphase interactions ($\mathbf{F}_{\text{exchange}}$ forces) by limiting them to discrete points of space \mathbf{x} in the continuous phase, in which the particles of the dispersed phase are present.

The momentum transfer between the gas stream and a single solid particle for the Eulerian-Lagrangian approach is calculated from the following equations (WACHEM, ALMSTEDT 2003):

$$F_{\text{exchange},i} = \frac{18 \eta C_D \text{Re}}{\rho_s d_s^2 24} (u_g - u_{s,i}) \quad (8)$$

$$\text{Re} = \frac{\rho_g d_s |u_g - u_{s,i}|}{\eta} \quad (9)$$

Symbols appearing in the above formulas indicate respectively: $\rho_s, \rho_g, \eta, d_s$ – particle density, fluid density, dynamic fluid viscosity and particle diameter, Re – relative Reynolds number, $\mathbf{u}_g, \mathbf{u}_{s,i}$ – velocity of gas stream and i -th particle. The last element is C_D drag coefficient. The model developed by MORSI and ALEXANDER (1972) for spherical particles was chosen for its calculation (according to the manufacturer’s data, the sphericity of circulating particles is 0.95):

$$C_D = a_1 + \frac{a_2}{Re} + \frac{a_3}{Re^2} \tag{10}$$

The constant a take different values in the function of the relative Reynolds number. It is one of the most complete correlations, taking into account the wide range of Reynolds numbers used.

Equations describing the movement of the dispersed phase are based on Newton’s second law of dynamics. The effects of gravity, interaction with the continuous phase and collisions with walls were taken into account in the calculations (WACHEM, ALMSTEDT 2003):

$$m_s \mathbf{a}_s = m_s \mathbf{g} + V_s \nabla \boldsymbol{\tau}_g - V_s \nabla P + m_s \mathbf{F}_{\text{exchange}} \tag{11}$$

where:

- \mathbf{a}_s – symbolizes the acceleration of a given solid particle,
- V_s – the volume of the particle,
- P – the local value of the pressure field,
- $\boldsymbol{\tau}_g$ – the stress tensor for the continuous phase, averaged in the calculation cell.

The expression $V_s \nabla \boldsymbol{\tau}_g$ is often omitted due to the small value in comparison with other parts on the right side of the equation. $\mathbf{F}_{\text{exchange}}$ is calculated from equation (8). Equation (11) does not contain the term related to the interaction between particles, because it can be omitted in our case due to the low concentration of the dispersed phase.

Inside the modelled apparatus oblique impacts take place (Fig. 3). In order to describe them the normal and tangential restitution coefficients are required. On their basis, the velocity of the particle and the angle of reflection after collision with the wall are determined according to equation (1). The oblique collision of a particle with the wall is schematically presented in Figure 3. The most important parameters of the model are marked on it: oblique incident velocity \mathbf{V}_i , being the resultant of the normal V_{ni} and tangential V_{ti} component, as well as incidence angles θ_i and critical angle θ_{cr} , the significance of which will be explained later. When particles come into contact with the wall, restitution coefficients e_n, e_t are calculated, leading to the formation of rebound velocity components V_{nr}, V_{tr} and determining the new velocity \mathbf{V}_r of the particle after collision.

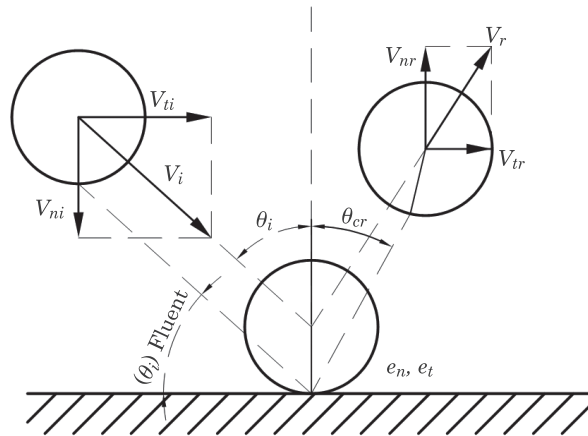


Fig. 3. The oblique impact of sphere on the flat surface

Source: based on LUDWIG and PLUSZKA (2018).

Calculation of the normal restitution coefficient

Elastic collisions for low particles velocities were described using Hertz theory (TIMOSHENKO, GOODIER 1951). They are characterized by the occurrence of stress wave effect, which is propagating in the material. The propagation of impact takes place at the expense of part of its initial kinetic energy. This dissipated fraction of energy is described using the kinetic energy loss ratio λ , which is correlated with a normal restitution coefficient (WU et al. 2005):

$$e_{n,\text{elast}} = \left(1 - \frac{\lambda}{100}\right)^{1/2} \quad (12)$$

where index elast indicates the range of elastic collisions and λ is calculated from the equation:

$$\lambda = 0.73 V_{ni}^{3/5} \quad (13)$$

As the collision velocity increases, the significance of plastic interactions also increases, while the significance of elastic interactions is reduced. In this work the analytical dependence of the normal restitution coefficient derived by Thornton from the simplified model of elastoplastic collision was used (THORNTON et al. 2001):

$$e_{n,\text{Thornton}} = \left\{ \left(\frac{6\sqrt{3}}{5} \right) \left[1 - \frac{1}{6} \left(\frac{V_y}{V_{ni}} \right)^2 \right] \right\}^{1/2} \left\{ \left(\frac{V_y}{V_{ni}} \right) \left[\left(\frac{V_y}{V_{ni}} \right) + 2 \sqrt{1.2 - 0.2 \left(\frac{V_y}{V_{ni}} \right)^2} \right] \right\}^{1/4} \quad (14)$$

where V_y is the yield velocity calculated from relation:

$$V_y = 3.194 \left(\frac{Y^5 (R^*)^3}{E^{*4} m^*} \right)^{0.5} \tag{15}$$

where Y is the yield strength, R^* , E^* , m^* are the effective radius, Young’s modulus and mass for impact of two materials. When the normal component of the particle velocity hitting the wall is greater than V_y , an elastoplastic collision is present and the normal restitution coefficient is calculated from equation (14). Otherwise, an elastic collision occurs and equation (12) is used.

In particle collisions with the deflector in the apparatus under investigation, the model for the normal velocity component will be predominant. In the case of rebounds from the inner surface of the draft tube and two surfaces of the annular zone, the hydrodynamics of the particles will be influenced mainly by the tangential model, which is described below.

Calculation of the tangential restitution coefficient

As with the normal restitution coefficient, the tangential part of the model is described by a single analytical equation. On the basis of available literature it was found that only one model of tangential collisions, presented in the article by WU et al. (2009) can be implemented in a relatively simple way in calculations. Its additional advantage is good correlation with experimental data, which is proved by the authors. Equations (16)–(18) present the most important model formulas (WU et al. 2009):

$$e_t = \begin{cases} 1 - \frac{2}{\Theta} [c_1 + c_2 \tanh(c_3 + c_4 \Theta)], & \Theta < \Theta_{crit} \\ 1 - \frac{2}{\Theta}, & \Theta \geq \Theta_{crit} \end{cases} \tag{16}$$

$$\Theta = \frac{2}{(1 + e_n)\mu} \tan(90^\circ - \theta_i) \tag{17}$$

$$\Theta_{crit} = \frac{7\kappa - 1}{\kappa} \tag{18}$$

where:

e_n – the normal restitution coefficient (determined by the normal model equation),

μ – the friction coefficient,

κ – the rigidity coefficient and θ is the incident angle.

In this paper θ is defined as the angle between the velocity vector and the wall plane, as opposed to the definition from the source article, where the angle formed by the velocity vector and the normal to the wall plane is operated (Fig. 3). The c coefficients from equation (16) were determined by approximation of the results of numerical simulations of FEM (Finite Element Method) presented in the paper of WU et al. (2009) and amount to: $c_1=0.4459$, $c_2=-0.6112$, $c_3=0.9288$, $c_4=-0.4050$, respectively.

Materials used in simulations

In order to use the equations presented in the previous chapter, the value of V_y from equation (14) has to be determined. In this case the physical properties of the colliding particles and walls (glass and aluminium) (Tab. 1) must be known (LUDWIG, PLUSZKA 2018). In the simulations Cellets® 1000 particles produced from microcrystalline cellulose by SYNTHAPHARM were modelled. They are frequently used as drug carrier in the pharmaceutical industry.

Air parameters were assumed to be constant: density 1.22 kg/m^3 , kinematic viscosity $1.75 \cdot 10^{-5} \text{ Pa}\cdot\text{s}$.

Table 1

Physical properties of materials used in simulations	
Quantity	Value
Young's modulus for Cellets® C1000 [GPa]	1.559
Young's modulus for borosilicate glass 3.3 [GPa]	64
Young's modulus for aluminium 2017 [GPa]	73
Poisson's ratio for Cellets® C1000	0.3
Poisson's ratio for borosilicone glass 3.3	0.2
Poisson's ratio for aluminium 2017	0.334
Plasticization Pressure for Cellets® C1000 [MPa]	108.55
Yield velocity [m/s]	2.08
Particle density [kg/m^3]	1.570
Particle diameter [mm]	1.11

Model solution

In order to solve the presented model Ansys Fluent solver was used which settings are presented in Table 2 and 3. In the course of previous studies, an optimal numerical mesh with polyhedral cells and the following parameters has been obtained: number of cells 708,621, number of faces 3,968,399, number

Table 2

Model parameters – fluid (continuous) phase

Parameter	Value
Solver	3D, pressure based, steady
Pressure-velocity coupling	SIMPLE
Turbulence model	standard $k-\epsilon$ with modification “realizable”
Description of near-wall zone	enhanced wall treatment
Boundary condition at the inlet to column	velocity inlet
Boundary condition at the outlet of column	pressure outlet
Discretization scheme	second order upwind
Limit of scaled residuals	$1 \cdot 10^{-4}$

Table 3

Model parameters – particles (discrete phase)

Parameter	Value
Type of solver	transient, interaction with continuous phase
Number of continuous phase iterations on one iteration of discrete phase	10
Type of injection surface	surface
Particle diameter distribution type	uniform
Injection time	10^{-1} s
Number of particle in parcel	varying with the mass of the bed
Wall boundary condition	reflect

of nodes 2,967,161, maximal skewness 0.583836 (LUDWIG, ZAJĄC 2017, LUDWIG, PLUSZKA 2018). The flow was assumed as isothermic and incompressible.

During the simulation, only the air outflow from the main spouting nozzle was taken into account, which was determined on the basis of experimental observations of the bed (Tab. 4) (LUDWIG, ZAJĄC 2017). The results of the average particle velocity for different values of friction coefficient (0.1–0.4) and volumes of the poured bed (100–400 cm³) were read in each calculation time step from a cross-section located approximately in the middle of the upper segment (Fig. 4).

Table 4

Air velocities in the spouting nozzle corresponding to various volumes of bed applied during calculations

w_0 [m/s]	V_{bed} [cm ³]	H_{bed} [mm]
189	100	34
278	200	54
333	300	74
407	400	94

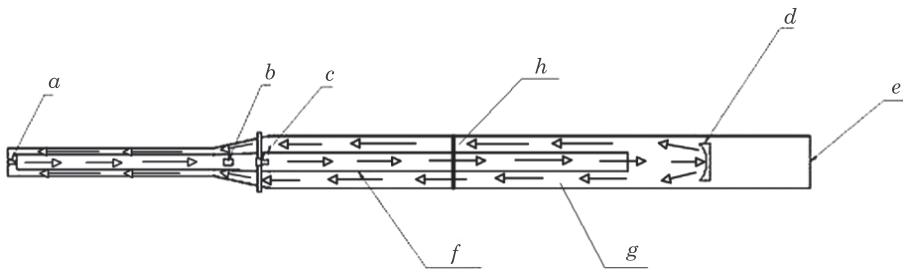


Fig. 4. Section of the simplified apparatus geometry used in the simulation (arrows show the circulation of particles): *a* — spouting air nozzle, *b* — powder spraying nozzle, *c* — liquid spraying nozzle, *d* — deflector, *e* — air outlet, *f* — draft tube, *g* — annular zone, *h* — localization of measurements and simulation data reading

Source: based on LUDWIG and PŁUSZKA (2018).

These results were then averaged over time. The averaged value of particle velocity was compared with experimental results obtained by PIV (Particle Image Velocimetry) method, which was described in detail in the article of LUDWIG and ZAJĄC (2017).

Results and discussion

In the course of calculations, a relatively small influence of friction coefficient on particles velocity was observed in the tested zones of the apparatus. Its increase by 300% from 0.1 to 0.4 caused an increase in particles velocity in the draft tube by maximum 16% (on average 14%) (Fig. 5), while its decrease in the annular zone by maximum 25% (on average 18%) (Fig. 6). The changes were

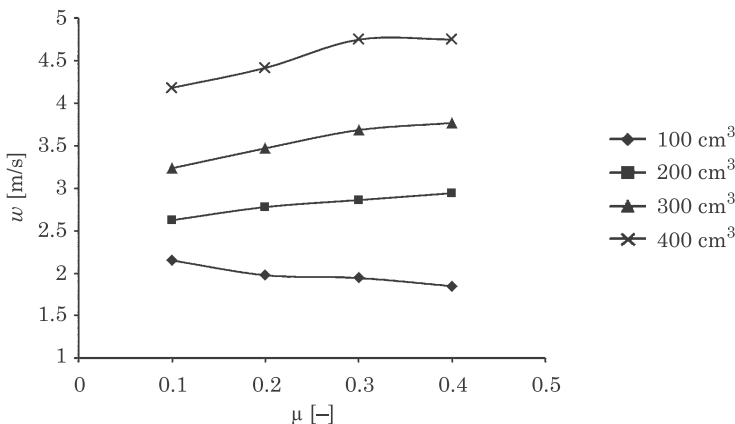


Fig. 5. Particles velocity in the draft tube as a function of friction coefficient for different volumes of the bed

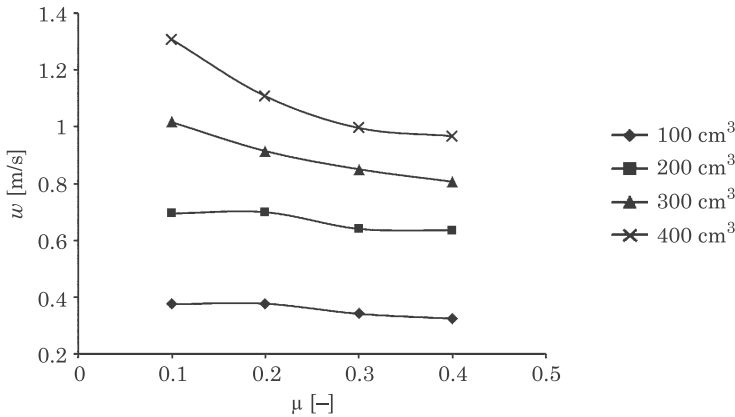


Fig. 6. Particles velocity in the annular zone as a function of friction coefficient for different volumes of the bed

most visible for large volumes of the bed in the annulus. For $V_{bed}=100 \text{ cm}^3$ and $V_{bed}=400 \text{ cm}^3$ they equalled respectively -13% and -26% in this zone (Fig. 6). In the draft tube the influence of the number of circulating particles was small (for $V_{bed} = 200 \text{ cm}^3$ the change was 12% and for $V_{bed} = 400 \text{ cm}^3$ 13%) (Fig. 5).

As the volume of the bed increases, the number of collisions between particles and the walls of the device increases. The number of collisions in the annulus is much higher than in the draft tube because the particles after rebounding from the curved bowl of the deflector move on curvilinear tracks, rebounding successively from the outer wall of the draft tube and the inner wall of the apparatus (LUDWIG, PŁUSZKA 2018). Inside the draft tube, except in the zone just above the spouting gas nozzle where there is intensive mixing, the bed moves parallel to the walls of the device.

The different dependency of particle velocity on the friction coefficient in the draft tube and the annular zone results from the properties of equation (15) (Fig. 7). According to it, in the area of low test angles (below approximately 70° , depending on the normal restitution coefficient), an increase in the value of the friction coefficient causes a decrease in the tangential restitution coefficient. For high incidence angles this relationship is reversed. A relatively small number of collisions with a high incidence angle occur in the draft tube, especially in the bottom part of the apparatus, where the bed is intensively circulating (LUDWIG, PŁUSZKA 2018). In the annular zone, on the other hand, the collisions are more frequent and the particles collide with the walls at low angles.

In the case of a 100 cm^3 bed, the particle velocity in both the draft tube and the annular zone always decreases with the increase in the friction coefficient from 0.1 to 0.4, but this change is small and amounts to -13% and -14% respectively (Fig. 5 and 6). With such a small number of particles, they do not mix in the lower zone of the draft tube and they move parallel to the walls from

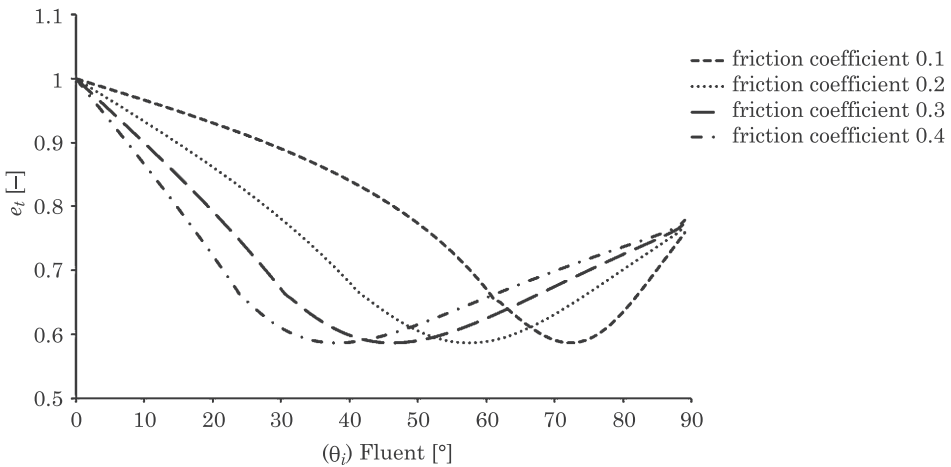


Fig. 7. Tangential restitution coefficient as a function of incident angle between particle velocity vector and the wall plane for different friction coefficients according to equation (16) (normal restitution coefficient 0.9)

the beginning and their incidence angles are small, resulting in a decrease in tangential restitution coefficients as the friction coefficient increases.

The curve of particle velocity simulation results in the draft tube for the coefficient of friction 0.1 gives the highest accuracy in reference to the experimental data in the draft tube (the largest and smallest relative errors are 15% and 1% respectively) and in the annular zone (the largest and smallest relative errors are 57% and 34% respectively) (Fig. 8 and 9). However, the increase in accuracy with respect to the value of 0.2 used in the previous calculations is small. In this case, the largest and smallest relative errors in the draft tube were 22% and 1% respectively and in the annular zone 57% and 44%. The relative error

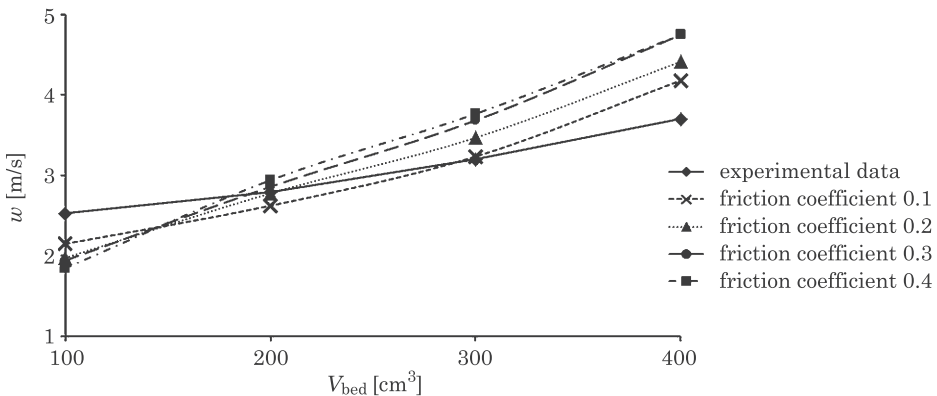


Fig. 8. Particles velocity as a function of bed's volume for different friction coefficients in the draft tube

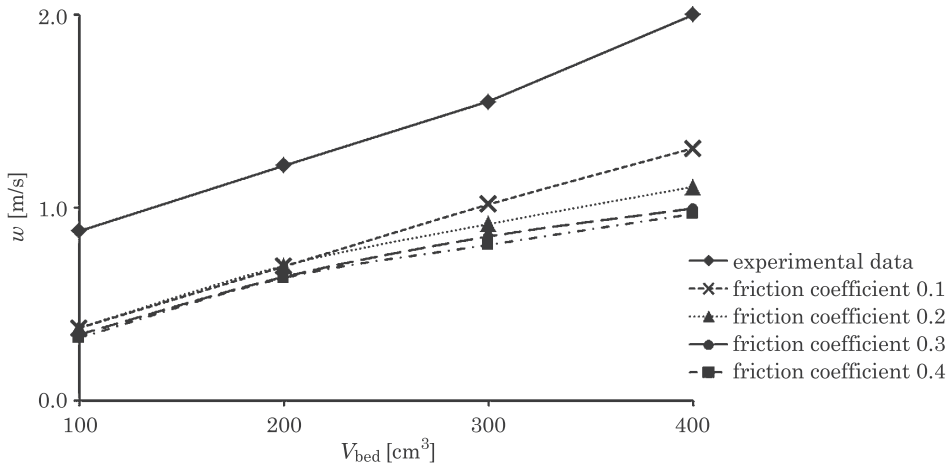


Fig. 9. Particles velocity as a function of bed's volume for different friction coefficients in the annular zone

in the annular zone remained relatively high, which was related to the hydrodynamics of the bed flow at this point (high values of the normal component of the particle velocity) and the properties of Thorton's equation (rapid decrease in the normal restitution coefficient with an increase in incident velocity). In turn, high values of incidence angles of particles against the apparatus walls in this zone caused a decrease in the tangential restitution coefficient. Both these factors caused the calculated particle velocity to be understated. A detailed description of this mechanism can be found in article LUDWIG and PŁUSZKA (2018).

Conclusions

The paper analyses the impact of the friction coefficient, difficult to measure and therefore not widely published in the literature, on the results of particle velocity simulation in a spout-fluid bed apparatus for dry coating. The most important zones from the point of view of the process have been taken into account: the draft tube and the annulus. It has been shown that even a large change in the assumed value of the friction coefficient of particles against the wall does not significantly affect the accuracy of model calculations. Therefore, this value does not need to be determined experimentally with high accuracy, which is very difficult. For model calculations it is enough to know only the approximate value of this parameter. An apparently surprising observation was also made that, depending on the particle incidence angle, an increase in the friction coefficient may cause both an increase and a decrease in their velocity. The choice of models calculating perpendicular and tangential restitution

coefficients has a significantly greater influence than the friction coefficient value. The literature offers many items concerning the description of these correlations (LI et al. 2001, JACKSON et. al. 2010). This will be the subject of my further research.

Acknowledgements

The studies were funded by the Polish National Science Centre within the framework of the research grant UMO-2013/09/B/ST8/00157.

References

- CUNDALL P.A., STRACK O.D. 1979. *A discrete element model for granular assemblies*. Géotechnique, 29: 47–65.
- DEEN N.G., SINT ANNALAND M. VAN, HOEF M.A. VAN DER, KUIPERS J.A.M. 2007. *Review of discrete particle modeling of fluidized beds*. Chemical Engineering Science, 62: 28–44.
- EPSTEIN N., GRACE J.R. 2011. *Spouted and Spout-Fluid Bed. Fundamentals and Application*. Cambridge University Press, Cambridge.
- GELDART D. 1973. *Types of fluidization*. Powder Technology, 7: 285–292.
- HOOMANS B.P.B., KUIPERS J.A.M., BRIELS W.J., SWAAIJ W.P.M. VAN. 1996. *Discrete particle simulation of bubble and slug formation in a two-dimensional gas-fluidised bed: a hard-sphere approach*. Chemical Engineering Science, 51: 99–118.
- ISHIKURA T., NAGASHIMA H., IDE M. 2003. *Hydrodynamics of a spouted bed with a porous draft tube containing a small amount of finer particles*. Powder Technology, 131: 56–65.
- JACKSON R.L., GREEN I., MARGHITU D.B. 2010. *Predicting the coefficient of restitution of impacting elastic-perfectly plastic spheres*. Nonlinear Dynamics, 60: 217–229.
- JAWORSKI Z. 2005. *Computational fluid dynamics in chemical and process engineerin*. First ed. EXIT, Warszawa.
- KARLSSON S., BJOERN I.N., FOLESTAD S., RASMUSON A. 2006. *Measurements of the particle movement in the fountain region of a Wurster type bed*. Powder Technology, 165: 22–29.
- LI L.Y., WU C.Y., THORNTON C. 2002. *A theoretical model for the contact of elastoplastic bodies*. *Proceedings of the Institution of Mechanical Engineers*. Part C. Journal of Mechanical Engineering Science, 216: 421–431.
- LUDWIG W. 2016. *Hydrodynamics of particles flow in the modified Wurster apparatus operating in a fast circulating dilute spout-fluid bed regime*. In Proceedings of the 22nd Polish Conference of Chemical and Process Engineering in Spala, p. 788–799.
- LUDWIG W., PLUSZKA P. 2018. *Euler-Lagrange model of particles circulation in a spout-fluid bed apparatus for dry coating*. Powder Technology, 328: 375–388.
- LUDWIG W., ZAJĄC D. 2017. *Modeling of particle velocities in an apparatus with a draft tube operating in a fast circulating dilute spout-fluid bed regime*. Powder Technology, 319: 332–345.
- MATHUR K.B., GISHLER P.E. 1955. *A technique for contacting gases with coarse solid particles*. AIChE Journal, 1: 157–164.
- MOLINER C., MARCHELLI F., BOSIO B., ARATO E. 2017. *Modelling of Spouted and Spout-Fluid Beds: Key for Their Successful Scale Up*. Energies, 10: 1729–1768.
- MORSI S.A., ALEXANDER A.J. 1972. *An Investigation of Particle Trajectories in Two-Phase Flow Systems*. Journal of Fluid Mechanics, 55: 193–208.
- RANADE V.V. 2002. *Computational Flow Modeling for Chemical Reactor Engineering*. Vol. 5. First ed. Academic Press, San Diego.

- SUTKAR V.S., DEEN N.G., KUIPERS J.A.M. 2013. *Spout fluidized beds: recent advances in experimental and numerical studies*. Chemical Engineering Science, 86: 124–136.
- SZAFRAN R.G., LUDWIG W., KMIEĆ A. 2012. *New spout-fluid bed apparatus for electrostatic coating of fine particles and encapsulation*. Powder Technology, 225: 52–57.
- TEUNOU E., PONCELET D. 2002. *Batch and continuous bed coating — review and state of the art*. Journal of Food Engineering, 53: 325–340.
- THORNTON C., NING Z., WU C.Y., NASRULLAH M., LI L.Y. 2001. *Contact Mechanics and Coefficients of Restitution*. Granular Gases, Springer, Berlin, p. 184–194.
- TIMOSHENKO S. , GOODIER J.N. 1951. *Theory of Elasticity*. Second ed. McGraw-Hill, New York.
- TSUJI Y., KAWAGUCHI T., TANAKA T. 1993. *Discrete particle simulation of two-dimensional fluidized bed*. Powder Technology, 77: 79–87.
- WACHEM B.G.M. ALMSTEDT A.E. 2003. *Methods for multiphase computational fluid dynamics*. Chemical Engineering Journal, 96: 81–98.
- WU C.Y., LI L.Y., THORNTON C. 2005. *Energy dissipation during normal impact of elastic and elastic-plastic spheres*. International Journal of Impact Engineering, 32: 593–604.
- WU C.Y., SEVILLE J. 2016. *Particle Technology and Engineering*. Elsevier.
- WU C.Y., THORNTON C., LI L.Y. 2009. *A semi-analytical model for oblique impacts of elastoplastic spheres*. Proceedings of the Royal Society, A, 465: 937–960.
- ZHONG W., ZHANG Y., JIN B. 2010. *Novel method to study the particle circulation in a flatbottom spout-fluid bed*. Energy & Fuels, 24: 5131–5138.



Quarterly peer-reviewed scientific journal

ISSN 1505-4675
e-ISSN 2083-4527

TECHNICAL SCIENCES

Homepage: www.uwm.edu.pl/techsci/



INFLUENCE OF SAW CHAIN TYPE AND WOOD SPECIES ON THE KICKBACK ANGLE OF A CHAINSAW

Zdzisław Kaliniewicz¹, Łukasz Maleszewski¹, Zbigniew Krzyśiak²

¹ Department of Heavy-Duty Machines and Research Methodology
University of Warmia and Mazury in Olsztyn

² Department of Mechanical Engineering and Automation
University of Life Sciences in Lublin

Received 25 April 2018; accepted 25 November 2018; available online 25 November 2018.

Key words: chainsaw, kickback, saw chain, wood, correlation.

Abstract

Wood processing operations, in particular debarking, can pose a significant hazard for the chainsaw operator when performed without due caution. The most common hazards with potentially fatal consequences include kickback which occurs when the chainsaw's guide bar is violently thrown backwards towards the operator. The aim of this study was to determine the influence of wood species and different saw chain brands on the kickback angle of a chainsaw. The kickback angle of a combustion chainsaw was analyzed in a self-designed test stand with the use of a digital level gauge accurate to 0.1°. Four differently priced saw chain brands, including two standard chains and two chains with anti-kickback features, were evaluated. Kickback was analyzed on five wood species (pine, spruce, birch, alder and oak) at three engine speeds (50%, 75% and 100% of maximum rotational speed). Kickback was significantly determined by wood species and saw chain type, and it was less influenced by the rotational speed of the chainsaw engine. The average kickback angle was largest in alder and smallest in spruce. The analyzed parameter was not always reduced by saw chains with anti-kickback features. In some cases, low-priced saw chains with anti-kickback features offer less protection than more expensive standard chains. Chainsaw buyers should decide whether it is worthwhile to compromise on safety in exchange for a lower price.

Correspondence: Zdzisław Kaliniewicz, Katedra Maszyn Roboczych i Metodologii Badań, Uniwersytet Warmińsko-Mazurski w Olsztynie, ul. Oczapowskiego 11/B112, 10-719 Olsztyn, phone: 48 89 523 39 34, e-mail: zdzislaw.kaliniewicz@uwm.edu.pl

Introduction

Around 90% of wood harvesting operations in Poland are performed with the use of portable chainsaws (DĄBROWSKI 2004, MACIAK 2011). Chainsaws are widely used by both professional loggers as well as amateurs for performing minor tasks in construction sites, farms and home gardens (DĄBROWSKI 2012). A chainsaw consists of a saw chain that rotates along a guide bar. The saw chain is an exposed element which poses a considerable threat for the operator and his immediate surroundings. The majority of accidents involving chainsaws result from direct contact with a moving saw chain (KOEHLER et al. 2004, MALINOWSKA-BOROWSKA et al. 2012, WÓJCIK 2013, ROOB, COCKING 2014). To minimize that risk, modern chainsaws are equipped with anti-kickback features (DĄBROWSKI 2004, 2009, KALJUN, DOLŠAK 2012, TOMCZAK et al. 2012, WÓJCIK 2012). These include right and left hand guards, a chain catcher and a chain brake. The left hand guard protects the hand on the front handle, and it is integrated with the brake lever which stops the chainsaw (the brake is activated by the operator or automatically when the chainsaw kicks back). The right hand guard prevents a dislocated or broken chain from being thrown back to the hand on the front handle. The chain catcher is positioned underneath the chainsaw body in front of the clutch, and it serves a similar purpose. The most important safety feature is the chain brake which is activated by the operator or automatically when the guide bar kicks back. Kickback occurs when the tip of the guide bars comes into contact with a hard object, such as wood (BOWERS, RIPPY 2009, MACIAK 2009, DĄBROWSKI 2012, WÓJCIK 2013, ARNOLD, PARMIGIANI 2015). The saw chain comes to an abrupt stop or becomes wedged in the processed material, and the guide bar is thrown back towards the operator. The chainsaw rotates around its axis, and the cutting assembly poses a significant hazard for the operator. According to standard PN-ISO 6335-1999, mean chainsaw brake time should not exceed 0.12 s, and it should not exceed 0.15 s in any trial. The brake immobilizes the saw chain when the cutting assembly is thrown towards the operator, which minimizes the risk of serious injury. According to WIĘSIK (2001), kickback energy is determined by the moment of inertia of the power transmission system (engine, flywheel and clutch) and the cutting assembly, angular velocity of the crankshaft immediately before impact, and angular velocity of the crankshaft at which the clutch is disengaged. Kickback can be completely eliminated by sheathing the guide bar tip, but this solution compromises performance because it reduces active cutting length and prevents plunge-cutting (WIĘSIK 2001, WÓJCIK 2013). Chainsaws with the above modification of the cutting assembly can be used to perform minor tasks, but are not suited for professional use in forestry.

Kickback risk can be minimized by dispersing the generated energy. This can be accomplished by firmly grabbing the handle and assuming a proper

body position during operation (BOWERS, RIPPY 2009). Kickback is a rapid event which is usually not anticipated by the operator. For this reason, anti-kickback features are the key to the safe use of a chainsaw. In chainsaws with safety features, chain links have a different design. The depth gauge in front of each cutter has a special profile, and drive links and tie straps have higher pitch (DĄBROWSKI 2004, TOMCZAK et al. 2012). Chainsaws with low-profile chains have emerged in recent years. Cutting teeth and tie straps have an oblique profile in the rear part of the sliding surface, and the resulting clearance between the tooth and the guide bar dampens vibrations and decreases kickback energy.

The factors which significantly influence kickback angle and kickback energy have been exhaustively discussed by DĄBROWSKI (2012, 2015). They include engine power and rotational speed, length of the guide bar, radius of the guide bar tip, type of saw chain and its geometric parameters, chain tension, sharpness of cutting teeth, chain brake effectiveness, temperature and moisture content of wood, position of the saw chain relative to the direction of wood grain. Kickback risk increases with an increase in engine power (displacement). Amateur operators should opt for chainsaws with smaller engines and smaller potential kickback angle, even at the expense of lower cutting performance. Professional loggers should also choose chainsaws that are best suited for the performed tasks to avoid working with heavy equipment and to minimize the risk of kickback (DĄBROWSKI 2012).

The length of the guide bar should also be appropriately selected for the task at hand. The longer the guide bar, the smaller the kickback angle. A longer guide bar decreases the moment of inertia of the cutting assembly and moves the cutting force away from the engine; therefore, a large portion of the chain's kinetic energy is absorbed in the cutting process. According to the literature (DĄBROWSKI 2012, 2015), kickback energy accounts for only 2% to 11% of the chain's kinetic energy, but it can still have very dangerous consequences for the operator. In practice, very long guide bars do not serve a useful purpose. They add to the chainsaw's weight and make it more difficult to operate. In extreme cases, engine power may be insufficient to effectively perform a cutting operation. Guide bars with a tapered end and small nose radius, preferably with an armor tip, increase operating safety (MACIAK 2009, DĄBROWSKI 2012).

Kickback is also effectively minimized by the chain brake which decreases the kickback angle by around 30–39% (DĄBROWSKI 2012). Chain stopping time is much shorter than the duration of kickback, which indicates that chain breaks are effective and should be installed in modern chainsaws as a standard feature. Some chainsaw brands, in particular log debarkers, are equipped with an additional brake lever by the rear handle (MACIAK 2009, WÓJCIK 2013, 2017). This feature enforces correct posture during operation, and it supports rapid braking during kickback when the operator's hand is thrown back to the brake lever.

According to BOWERS and RIPPY (2009) and TOMCZAK et al. (2012), chainsaw operators can minimize kickback by holding the front handle with the thumb in opposition to the remaining fingers, assuming a correct posture, anticipating dangerous events, initiating the cutting process with the underside of the guide bar, sharpening and maintaining the saw chain in good condition, and using saw chains with anti-kickback features. The appropriate cutting teeth geometry not only increases operating safety, but also improves performance (DĄBROWSKI 2012). For this reason, cutting teeth should be sharpened and maintained with the appropriate tools, and unskilled operators should rely on professional service outlets where saw chains are sharpened mechanically, despite the fact that mechanical sharpening shortens the chain's service life. Operators should ensure that the tension of the saw chain is properly adjusted. There are no universal tensioning guidelines. A correctly tensioned saw chain should adhere closely to the guide bar and move freely around it (TOMCZAK et al. 2012). Proper tensioning significantly reduces the kickback angle (DĄBROWSKI 2012, WÓJCIK 2013). The introduction of automatic chain tensioning systems would greatly reduce kickback and improve performance.

DĄBROWSKI (2012, 2015) states that the use of saw chains with anti-kickback features significantly reduce kickback. There is a wide selection of saw chain brands which differ vastly in price. Buyers are often faced with the dilemma whether low-priced saw chains compromise operating safety. In the literature, most kickback analyses were performed on samples of debarked wood. In practice, the saw rarely comes into contact with debarked wood at the beginning of the cutting process. Kickback occurs mainly during debarking or unskilled attempts at plunge-cutting (MACIAK 2009, TOMCZAK et al. 2012). Therefore, in the first phase of kickback, the saw is usually in contact with bark. For this reason, kickback analyses should be performed on samples of fresh wood, and the surface that comes into contact with the saw chain should not be debarked.

The aim of this study was to determine the influence of wood species and saw chain type on the kickback angle of a chainsaw.

Materials and Methods

The kickback angle of a combustion chainsaw was analyzed in a self-designed test stand (Fig. 1). The test stand was supported by a cradle of cold-formed closed profiles (2). A grip matching the shape of the chainsaw's front and rear handles was mounted on bearings in the cradle (1). The grip was fastened with cable ties around the top and rear parts of the chainsaw. The grip was connected to a digital level gauge on one side (4) and a unidirectional clutch on the other side. The level gauge measured the kickback angle which was modified by adjusting the segments of the loading lever (9). A jaw clutch coupling in front

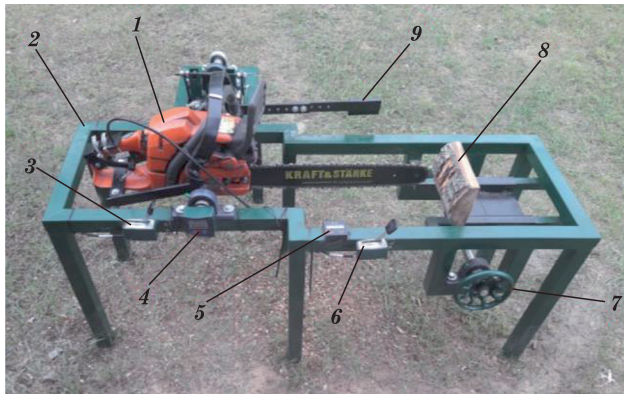


Fig. 1. Test stand for analyzing the kickback angle of a chainsaw: 1 – combustion chainsaw, 2 – cradle, 3 – clutch disengaging lever, 4 – digital level gauge, 5 – digital revolution counter, 6 – lever for controlling engine rotational speed, 7 – handwheel for adjusting the position of the wood sample, 8 – wood sample, 9 – loading lever

of the unidirectional clutch was used to return the chainsaw to its initial position. The wood sample (8) was fixed with screws to a shelf whose position relative to the chainsaw was controlled with a handwheel (7). The rotational speed of the chainsaw engine was adjusted mechanically with a lever controller (6), and it was measured with a digital revolution counter (5).

The test stand for measuring the kickback angle was equipped with the Husqvarna 345e combustion chainsaw with a 45 cm³ engine (2.2 kW). The chainsaw weighs 4.9 kg without cutting equipment, and it provides an idle speed of 2,700 rpm. The recommended speed at full power is 12,500 rpm. The clutch is disengaged at a speed of around 3,700 rpm. The recommended length of the guide bar is 18 to 45 cm. A Kraft & Starke guide bar with a length of 45 cm, nose radius of 23 mm and a 10 tooth sprocket was used in the test stand.

Four saw chains were tested in the study (Fig. 2), including two standard chains (SC-2 and SC-3) and two chains with anti-kickback features (SC-1 and SC-4). The technical specification and prices of the analyzed saw chains are presented in Table 1.

Saw chain kickback was tested on five wood species: pine, spruce, birch, alder and oak (Tab. 2). Wood samples were not debarked to simulate real-world conditions during wood harvesting. The samples were obtained directly from freshly logged trees by slicing off the top part of a trunk with a thickness of around 5 cm with the use of a frame saw. The slices were divided into segments with a length of around 20 cm to produce analytical samples. During the study, the samples were stored in sealed plastic bags to stabilize their relative moisture content. The relative moisture content of wood samples was analyzed in three replications for every wood species with the use of the DampMaster moisture meter (Laserliner, Germany) with $\pm 3\%$ accuracy.

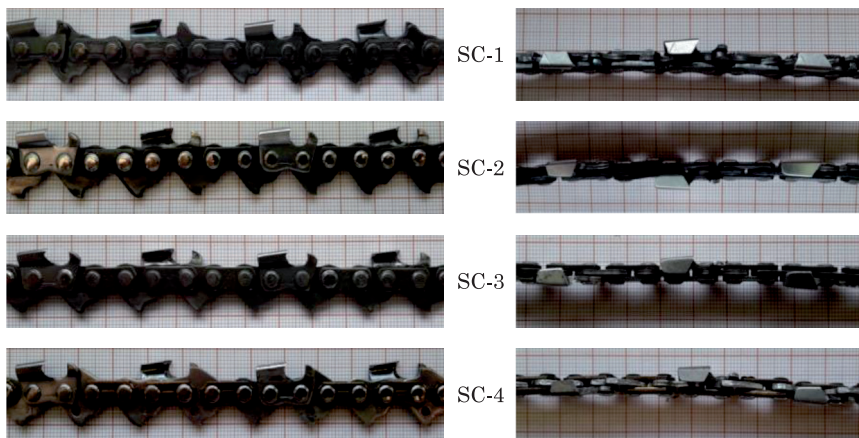


Fig. 2. Tested saw chains

Table 1

Specification of the tested saw chains

Symbol	No. of drive links	Pitch [in.]	Cutting tooth	Thickness of drive link [mm]	Anti-kickback drive link	Price [€]
SC-1	72	0.325	semi-chisel	1.5	yes	12.3
SC-2					no	8.2
SC-3					no	6.8
SC-4					yes	5.6

Table 2

Specification of the analyzed wood samples

Parameter	Wood species				
	pine	spruce	birch	alder	oak
Average trunk radius [cm]	12.5	8.2	21.3	14.0	20.1
Average bark thickness [mm]	3.4	2.4	6.8	6.2	7.2
Average moisture content [%]	58	69	61	63	55

Wood samples were fixed with screws to a shelf in the test stand with the bark-covered side facing the chainsaw. The samples were placed in the test stand by positioning the center of the trunk's radius of curvature around 1 cm higher than the sprocket's axis of rotation. The chainsaw was operated at three different speeds (50%, 75% and 100% of maximum rotational speed), and the wood sample was moved in the direction of the saw chain with a constant speed of around 0.01 m/s until kickback. The kickback angle was measured to the nearest 0.1° with a digital level gauge. Measurements in every variant were conducted in ten replications. Based on the results of preliminary trials,

the segments of the loading lever were adjusted to ensure that the kickback angle of the most susceptible saw chain does not exceed 70° (according to standard ISO 9518:1998).

The measured kickback angles were processed statistically in the Statistica PL v. 12.5 program at a significance level of $\alpha=0.05$. The differences between average kickback angles were determined by factorial ANOVA. Normal distribution in each group was analyzed with the use of the Shapiro-Wilk W test, and homogeneity of variance was evaluated with Levene’s test (RABIEJ 2012).

Results

The average values of the kickback angle for every tested variant are presented in Figure 3. The analyzed parameter ranged from 10.3° (spruce, saw chain SC-1, 50% of maximum rotational speed) to 54.9° (pine, saw chain SC-4, 50% of maximum rotational speed). Wood species, saw chain type and engine speed had a varied influence on the kickback angle. The largest kickback angles were most frequently noted during tests performed at maximum engine speed (8 out of 20 cases), on alder samples (8 out of 12 cases) with saw chain SC-3 (8 out of 15 cases). Chainsaw operations performed on spruce samples (8 out

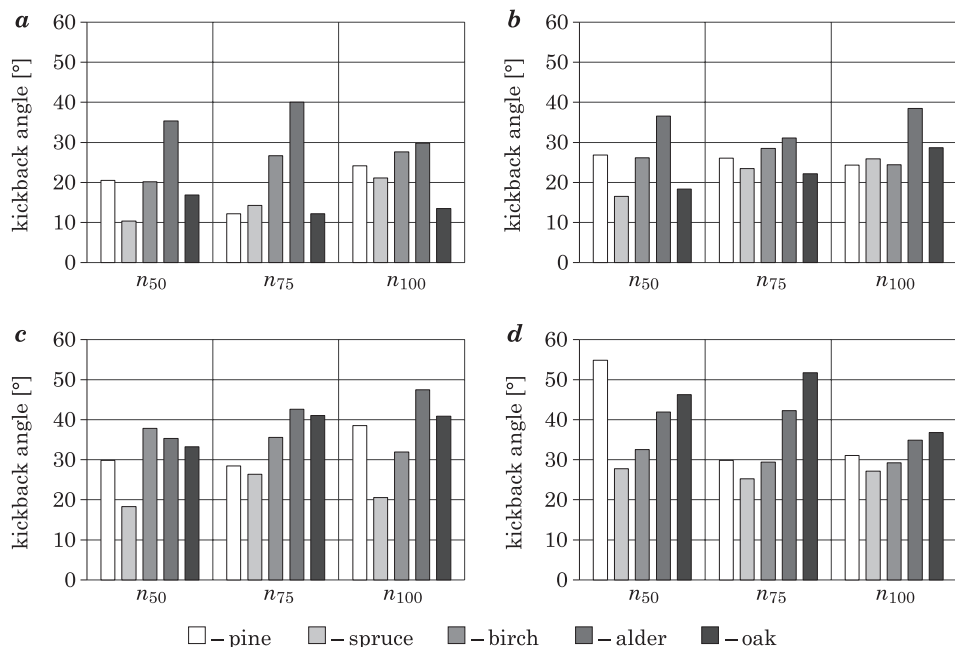


Fig. 3. Kickback angles for different engine rotational speeds, saw chain types and wood species: a – SC-1, b – SC-2, c – SC-3, d – SC-4

of 12 cases) with saw chain SC-1 supplied by a renowned manufacturer and equipped with anti-kickback features (10 out of 15 cases) were characterized by the highest operating safety.

The results of analyses evaluating the influence of wood species, saw chain type and engine speed on the kickback angle are presented in Tables 3÷5. Engine speed had the smallest impact on the analyzed parameter, but it exerted a significant influence in interaction with other factors. Saw chain SC-1 ensured the highest level of operating safety, whereas saw chain SC-4 was characterized by the lowest safety despite the presence of anti-kickback features. These saw chains differed considerably in price, and the safer option was twice as expensive as its cheaper counterpart. The price accurately reflects the manufacturing precision and the quality of materials used in the compared saw chains. The potentially most unsafe wood was alder (average kickback angle of 38°), and the safest wood was spruce (average kickback angle of 21.41°). Pine, birch and oak were similar in this regard. The average kickback angle was also similar at the same engine speeds, and the greatest variations in the analyzed parameter were noted at 50% of maximum engine speed.

Table 3

The influence of wood species and engine rotational speed on the kickback angle

Type of saw chain	Kickback angle [°] $x \pm SD$	Probability p for:		
		1 – wood species	2 – engine speed	1 × 2
SC-1	21.65 ± 9.41	< 0.001	0.002	< 0.001
SC-2	26.49 ± 6.76	< 0.001	< 0.001	< 0.001
SC-3	33.86 ± 8.77	< 0.001	< 0.001	< 0.001
SC-4	36.07 ± 9.61	< 0.001	< 0.001	< 0.001

$x \pm SD$ – mean value ± standard deviation

The analyzed factor significantly influences the kickback angle at a probability level of $p < 0.05$.

Table 4

The influence of saw chain type and engine rotational speed on the kickback angle

Wood species	Kickback angle [°] $x \pm SD$	Probability p for:		
		1 – saw chain type	2 – engine speed	1 × 2
Pine	28.89 ± 10.70	< 0.001	< 0.001	< 0.001
Spruce	21.41 ± 6.35	< 0.001	< 0.001	< 0.001
Birch	29.18 ± 5.73	< 0.001	0.087	< 0.001
Alder	37.99 ± 6.40	< 0.001	0.167	< 0.001
Oak	30.13 ± 13.39	< 0.001	0.001	< 0.001

$x \pm SD$ – mean value ± standard deviation

The analyzed factor significantly influences the kickback angle at a probability level of $p < 0.05$.

Table 5

The influence of saw chain type and wood species on the kickback angle

Engine speed	Kickback angle [°] $x \pm SD$	Probability p for factor:		
		1 – saw chain type	2 – wood species	1 × 2
n_{50}	29.28 ± 11.78	< 0.001	< 0.001	< 0.001
n_{75}	29.46 ± 10.75	< 0.001	< 0.001	< 0.001
n_{100}	29.82 ± 8.54	< 0.001	< 0.001	< 0.001

$x \pm SD$ – mean value ± standard deviation

The analyzed factor significantly influences the kickback angle at a probability level of $p < 0.05$.

Discussion

Chainsaw kickback is determined by both technical and operating factors (DĄBROWSKI 2012, 2015, WÓJCIK 2013). Technical factors include engine power, engine displacement, type and length of the guide bar, type of saw chain and efficiency of the cutting assembly. Operating factors are largely determined by the chainsaw operator who makes individual decisions regarding engine settings, the technical condition and tension of the saw chain, cutting technique and the use of protective equipment.

According to DĄBROWSKI (2012), operators should choose low-profile saw chains as well as saw chains with anti-kickback features. However, the results of this study revealed that drive links with a higher pitch do not always reduce kickback. Saw chain SC-4 was characterized by the largest average kickback angle which was even larger than in chain saws without anti-kickback features (SC-2 and SC-3). This suggests that kickback is significantly influenced by the profile of chain links, manufacturing precision and the quality of structural materials, which translates to a higher price. A comparison of the kickback angles of standard saw chains (SC-2 and SC-3) leads to similar conclusions (Tab. 3). Therefore, saw chains from renowned suppliers are more likely to guarantee manufacturing precision and operating safety.

Engine speed is controlled with the throttle trigger. According to DĄBROWSKI (2012), the kickback angle increases with an increase in the engine’s rotational speed because the kinetic energy imparted to chain links is used mainly for wood cutting. When the saw chain remains in contact with wood for a relatively long time, most of the generated energy is dispersed in the cutting process, which reduces kickback. In this study, the kickback angle of chainsaws equipped with the tested saw chains was significantly influenced when the engine was operated at 50–100% of maximum power in the analyzed wood species (the absence of such influence was noted only in birch and alder, Tab. 4). However, the nature of the observed changes is difficult to describe due to interactions between

the analyzed factors. The above observations are confirmed by the nearly equal average values of the kickback angle at the analyzed engine speeds (Tab. 5). Engine speed and, consequently, chain speed could exert a varied influence on the kickback angle due the presence of bark which is the first element that comes into contact with the saw chain. Bark surface is often uneven (due to the presence of cracks and groove), and the generated energy is dissipated differently on various types of wood.

According to DĄBROWSKI (2015), kickback is influenced by ambient temperature and the moisture content of wood. The kickback angle is largest at temperatures approximating 0°C and smallest when the processed wood is frozen. At low temperatures, wood fibers lose their elasticity, and their arrangement does not significantly influence the cutting process. In wood with high moisture content, fibers offer greater resistance against cutting teeth, which also increases kickback. The above implies that debarking of freshly cut trees requires greater caution than processing of declining trees or pre-dried wood. The wood samples analyzed in this study were characterized by high moisture content, therefore the noted kickback angles (Tab. 2) were close to the maximum values.

The kickback angle is also largely determined by wood species (Tab. 4). The smallest average kickback angle was noted in spruce, and the largest – in alder. Our findings do not fully conform to the observations made by DĄBROWSKI (2015) in whose study, kickback angle was not influenced by the hardness (and species) of wood. In the cited study, the largest kickback angle was reported in spruce, followed by oak and pine, and the smallest value of the analyzed parameter was noted in beech. The observed differences could be attributed to the fact that the samples analyzed in the cited study had been debarked. In the current study, trunk diameter was also an important factor (Tab. 2) which was smallest in spruce and largest in birch. According to DĄBROWSKI (2015), the kickback angle is proportional to the trunk's radius of curvature. In trunks with a larger radius, a longer section of the saw chain is wedged into the wood, which increases chain speed at the nose, transfers more energy in the opposite direction and causes kickback.

Conclusions

The results of this study indicate that chainsaw kickback is largely determined by wood species and saw chain type and is less influenced by engine speed. A clear pattern of changes in kickback angle is difficult to identify due to multiple interactions between the analyzed factors. In the present study, the kickback angle varied considerably from around 12° to around 55°. The average value of the analyzed parameter was smallest in spruce and highest in alder, whereas

pine, birch and oak were characterized by similar kickback angles. Considerable differences in average kickback angle were also observed between the tested saw chains. Not all chains with anti-kickback features effectively reduced the analyzed parameter. The kickback angle was decreased when the chainsaw was equipped with higher-priced chains made of higher-quality materials and characterized by greater manufacturing precision. Higher-priced saw chains were safer to operate than their cheaper counterparts. Chainsaw buyers should decide whether it is worthwhile to compromise on safety in exchange for a low price.

References

- ARNOLD D., PARMIGIANI J.P. 2015. *A study of chainsaw kickback*. Forest Products Journal, 65(5–6): 232–238. <http://dx.doi.org/10.13073/FPJ-D-14-00096>.
- BOWERS S., RIPPY R. 2009. *Safe and effective use of chain saws for woodland owners*. The Woodland Workbook EC, 1124: 1–17.
- DĄBROWSKI A. 2004. *Design solutions for portable chain saws, which increase the safety of their operation*. Bezpieczeństwo Pracy: Nauka i Praktyka, 12: 11–14 (article in Polish with an abstract in English).
- DĄBROWSKI A. 2009. *Portable chain saws – protection of the operator against contact with a moving tool*. Bezpieczeństwo Pracy: Nauka i Praktyka, 1: 16–19 (article in Polish with an abstract in English).
- DĄBROWSKI A. 2012. *Reducing kickback of portable combustion chain saws and related injury risks: laboratory tests and deductions*. International Journal of Occupational Safety and Ergonomics, 18(3): 399–417. <http://dx.doi.org/10.1080/10803548.2012.11076943>.
- DĄBROWSKI A. 2015. *Kickback risk of portable chainsaws while cutting wood of different properties: laboratory tests and deductions*. International Journal of Occupational Safety and Ergonomics, 21(4): 512–523. <http://dx.doi.org/10.1080/10803548.2015.1095547>
- ISO 9518:1998. *Forestry machinery – portable chain-saws – kickback test*. International Organization for Standardization, Geneva, Switzerland.
- KALJUN J., DOŁŚAK B. 2012. *Ergonomic design recommendations based on an actual chainsaw design*. South African Journal of Industrial Engineering, 23(2): 215–229.
- KOEHLER S.A., LUCKASEVIC T.M., ROZIN L., SHAKIR A., LADHAM S., OMALU B., DOMINICK J., WECHT C. 2004. *Death by chainsaw: fatal kickback injuries to the neck*. Journal of Forensic Sciences, 49(2): 345–50. <http://dx.doi.org/10.1520/JFS2003276>.
- MACIAK A. 2009. *Pilarka, jaka jest, każdy wie? (17) Hamulec bezpieczeństwa*. Drwal, 6: 36–38.
- MACIAK A. 2011. *Analiza rynku łańcuchowych pilarek spalinowych w Polsce*. Technika Rolnicza Ogrodnicza Leśna, 5: 2–4.
- MALINOWSKA-BOROWSKA J., SOCHOLIK V., HARAZIN B. 2012. *The health condition of forest workers exposed to noise and vibration produced by chain saws*. Medycyna Pracy, 63(1): 19–29 (article in Polish with an abstract in English).
- PN-ISO 6535:1999. *Pilarki łańcuchowe przenośne. Badanie hamulca pily łańcuchowej*. Polski Komitet Normalizacyjny, Warszawa, Polska.
- RABIEJ M. 2012. *Statystyka z programem Statistica*. Helion, Gliwice.
- ROBB W., COCKING J. 2014. *Review of European chainsaw fatalities, accidents and trends*. Arboricultural Journal, 36(2): 103–126. <http://dx.doi.org/10.1080/03071375.2014.913944>.
- TOMCZAK A., JELONEK T., GRZYWIŃSKI W. 2012. *Pozyskiwanie drewna pilarką*. G&P Oficyna Wydawnicza, Poznań.

- WIĘSIK J. 2001. *Zagrożenia przy użytkowaniu przenośnych pilarek łańcuchowych do drewna – analiza zjawiska odbicia, sposoby eliminowania lub ograniczania jego skutków*. W: *Bezpieczeństwo użytkowania przenośnych pilarek łańcuchowych do drewna*. Centralny Instytut Ochrony Pracy, Warszawa.
- WÓJCIK K. 2012. *By pilarka była bezpieczna*. Nowa Gazeta Leśna, 11: 44–47.
- WÓJCIK K. 2013. *Jak ograniczyć niebezpieczne odbicia pilarki?* Nowa Gazeta Leśna, 7: 44–47.
- WÓJCIK K. 2017. *Hamulec piły łańcuchowej. Bezpieczne zatrzymanie*. Nowa Gazeta Leśna, 6: 78–82.



EVALUATION OF HIGH-TEMPERATURE CORROSION ON 13CrMo4-5 STEEL OPERATED IN THE POWER INDUSTRY

Monika Gwoździk

Institute of Materials Engineering
Faculty of Production Engineering and Materials Technology
Czestochowa University of Technology

Received 6 December 2017; accepted 5 December 2018; available online 5 December 2018.

Key words: oxide layer, 13CrMo4-5 steel, SEM, XRD, LM.

Abstract

The paper presents results of studies of steel and the oxide layer formed during a long-term operation ($t = 130,000$ h) on 13CrMo4-5 steel at an elevated temperature ($T = 455^\circ\text{C}$). The oxide layer was studied on a surface and a cross-section at the inner site of the pipe (in the flowing medium – steam side). The paper contains results of studies such as: light microscopy, scanning electron microscopy, X-ray phase analysis.

Introduction

Both in Poland and worldwide there are attempts to ensure the energy security both on an industrial and household scale. This makes that the research and development of structural materials to be used in a modern conventional and nuclear power industry are still relevant. The basic objective of proper repairing of power units is to increase their reliability and efficiency and to extend their life at minimised costs (TRZESZCZYŃSKI 2010, BRUNNÉ et al. 2011).

In recent years, as demonstrated by Polish studies, a substantial share in part failure frequency is that of corrosion. Among others, such parts as superheater coils of secondary steam boilers get damaged due to excessive reduction of wall

Correspondence: Monika Gwoździk, Instytut Inżynierii Materiałowej, Politechnika Częstochowska, al. Armii Krajowej 19, 42-201 Częstochowa, e-mail: gwozdzik.monika@wip.pcz.pl

thickness. It is due to corrosion, from the inside as well as from the outside. Such a reduction is due to the widely understood high temperature corrosion, a contribution to which is made by oxides formed on the surface (or absence of such oxides), which do not always perform a protective role (DOBOSIEWICZ, BRUNNÉ 2007, KLEPACKI, WYWROT 2010).

Protective layers of oxides, which are formed during the normal operation exert equally important influence upon the longevity of operation of parts of turbines and boiler, dependent on mechanical properties, including creep strength and creep limit. Their good adhesion is important, as well as very slow growth, and slight susceptibility to scaling. Excessive growth of oxide layer from the steam side (internal wall of pipe) has negative consequences during long term operation, because:

- it reduces the bore of pipes, especially in heavy wall tubes with small inside diameter;

- the oxide layer causes reduction of wall thickness and increase of stresses, moreover – scaling of oxide layer may lead to erosion inside the turbine.

Scaling of oxide layer is an extremely harmful phenomenon, as the scaled particles may get to the turbine, and lead to fatal consequences. Scaled oxide layers may clog the bore of superheater pipe, as well as other steam pipelines, causing local overheating, which often leads to pipe burst.

On the flue gas end, besides oxide layers also ash deposits are frequently formed, which most often insulate.

DOBOSIEWICZ and BRUNNÉ (2007) showed that the main reasons for the wear of superheater coils are physicochemical processes occurring in steel associated with the simultaneous impact of: high temperature, aggressive exhaust and significant stress. To this processes belong to: creep, high-temperature corrosion, steam corrosion, erosion. The result of these processes are: degradation of the structure under the influence of high temperature and corrosive and erosive wall thickness degradation.

Steels for use in elevated temperatures find wide application first of all in the power sector. This steels are used mainly for boiler pipes, superheater coils, chambers, pipelines, parts of boilers, steam turbines, as well as other devices. Such steels include inter alia 10CrMo9-10, 13CrMo4-5 and also a high-chromium steel X10CrMoVNb9-1 (LAVERDE et al. 2004, PRISS et. al. 2014, GWOŹDZIK 2016a, 2016b).

Material and Experimental Methods

The material studied comprised specimens of 13CrMo4-5 steel operated at 455°C during 130,000 hours (the base steel material and the oxide layer). The oxide layer was studied on a surface and a cross-section at the inner surface

(in the flowing medium – steam side) of the tube wall. Through examinations of material comprised:

- macroscopic and microscopic examinations using an Olympus SZ61, GX41 light microscope (LM) and Jeol JSM-6610LV scanning electron microscope (SEM);
- thickness measurements of formed oxide layers;
- chemical composition analysis of oxides using Jeol JSM-6610LV scanning electron microscope working with an Oxford EDS electron microprobe X-ray analyzer;
- XRD measurements (studying the phase composition, crystallite sizes (D_{hkl})); the layer was subject to measurements using a Seifert 3003T/T X-ray diffractometer and the radiation originating from a tube with a cobalt. A computer software and the PDF4+2009 crystallographic database were used for the phase identification. Based on the width and the position of the main coat and substrate reflections, the size of the crystallites (D_{hkl}) of hematite and magnetite were determined using the Scherrer formula. X-ray studies were carried out on the surface, and then the layer surface was polished down. The next the diffraction measurements were performed again to determine individual oxide layers. After removal of the Cu_2O , X-ray measurements were carried out, then for each case, the iron oxide layer was removed ($5\mu\text{m}$) cyclically, each time making XRD measurements. The main reflections originating from planes (104) for Fe_2O_3 and (311) for Fe_3O_4 have been analysed;
- a quantitative evaluation of ferrite and perlite/bainite was carried out. The microstructure of the steel was analyzed by analyzer of image. Then the average size of phase and their volume share were calculated.

Results of examinations

The microscopic observations of the surface of the oxide layer showed a significant degree of layer development. Directly on the surface, the spheroidal character of the oxide layer was observed (Fig. 1). EDS studies have shown (Fig. 2) that the oxide layer is composed of copper oxides and iron oxides, where the dominant element is iron. Three zones have been distinguished in the oxides layer formed. Cu_2O occurs at the surface, then hematite (Fe_2O_3), under which a magnetite (Fe_3O_4) exists (Fig. 3).

Copper compounds appearing on the internal surfaces of energy equipment elements and in the entire water-steam system are the result of progressive erosion and corrosion processes in supply and condensation systems, where these waters are enriched in trace amounts of copper compounds (ŚLIWA, GAWRON 2009, GAWRON 2014). One of the main sources of copper compounds emission to the circulating medium are such elements of power devices as: condensers and regeneration heat exchangers. In this type of elements, the progressive

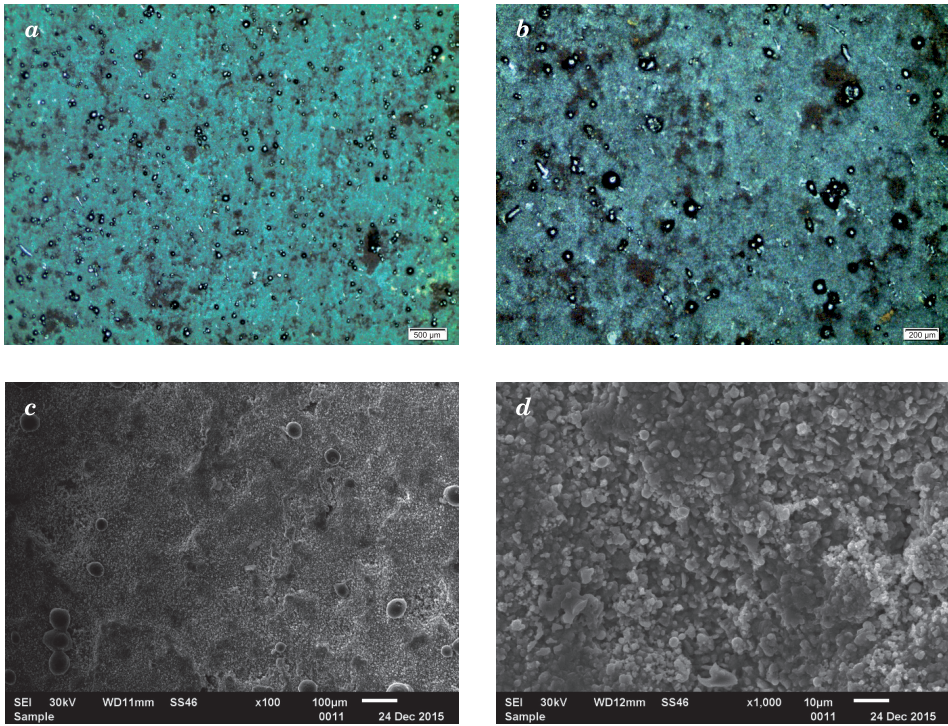


Fig. 1. Oxides formed on 13CrMo4-5 steel, inner surface:
a – LM, 20×, *b* – LM, 45×, *c* – SEM, 100×, *d* – SEM, 1000×

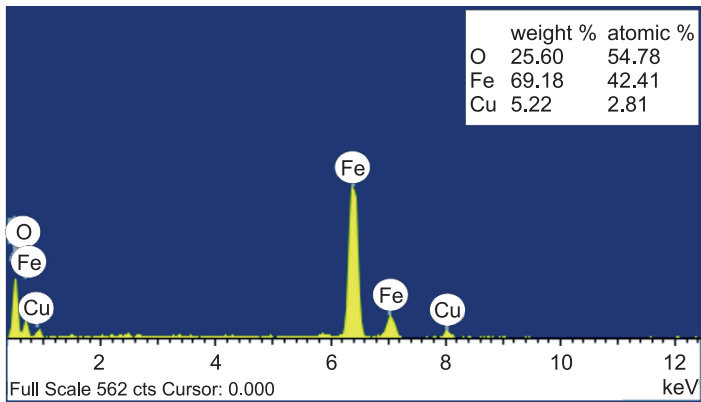


Fig. 2. EDS analysis of surface of oxides

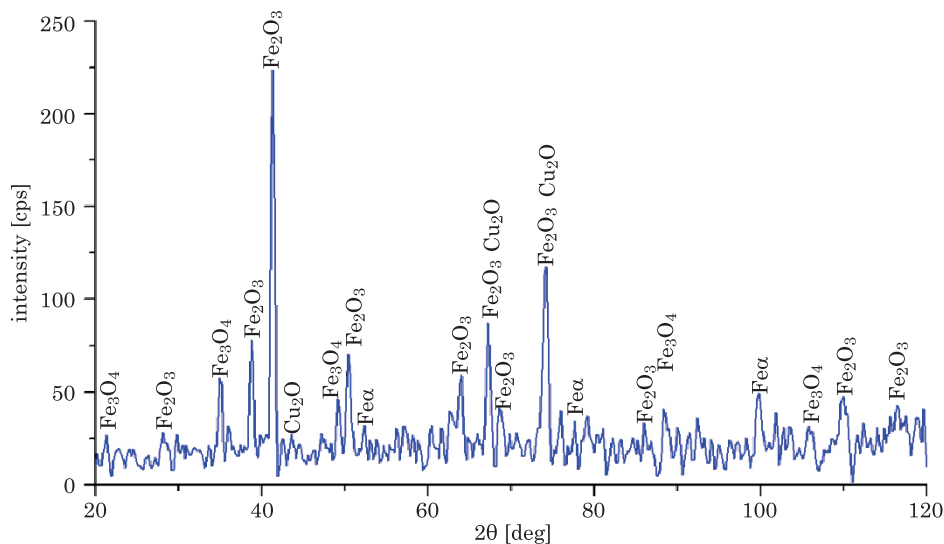


Fig. 3. X-ray diffraction patterns from the surface of oxide layer

corrosion processes result in the transfer of copper to the water in an ionic form. Copper then reacts with other compounds found in the circulating medium, which in turn causes uncontrolled emission of copper compounds, which under the temperature conditions of the boiler is released in the form of sediments. In addition, copper can pass into feed water in the form of copper oxides and copper metallic. This is caused by erosion or corrosion-erosion processes. These processes are caused by the influence of droplets on the condenser tubes or too high velocities of water flow through the tubes of the low-pressure regenerative heat exchangers (ŚLIWA, GAWRON 2009). However, from the side of the flue gas flow on this steel, as shown by previous tests, SiO_2 (GWOŹDZIK 2016b) occurs. SiO_2 precipitates in electrofilters after burning coal in various types of furnaces of power facilities (LELUSZ 2012).

The oxide layer formed on the studied steel on the inner side is $54.82 \mu\text{m}$ thick. This layer is mostly degraded. This degradation occurs in the form of microcracks and fissures. Directly on the steel side, there is little corrosion on the grain boundaries. The pits covered with oxides have been directly from the steel side. The pits are $76.37 \mu\text{m}$ thick.

Studies of crystallite sizes have shown (Fig. 4) that the hematite were existed to a depth of polishing $15 \mu\text{m}$. The crystallite size for this oxide was 43.14 nm , 42.15 nm , 16.34 nm , after removal of the layer by $5 \mu\text{m}$, $10 \mu\text{m}$ and $15 \mu\text{m}$, respectively. In contrast, the size of crystallites for magnetite gradually increases to a depth of $30 \mu\text{m}$ and it was 38.23 nm (The crystallite size for this oxide was 17.98 nm , 19.10 nm , 33.98 nm , 35.54 nm , 37.32 nm , 38.23 nm after removal of the layer by $5 \mu\text{m}$, $10 \mu\text{m}$, $15 \mu\text{m}$, $20 \mu\text{m}$, $25 \mu\text{m}$ and $30 \mu\text{m}$, respectively).

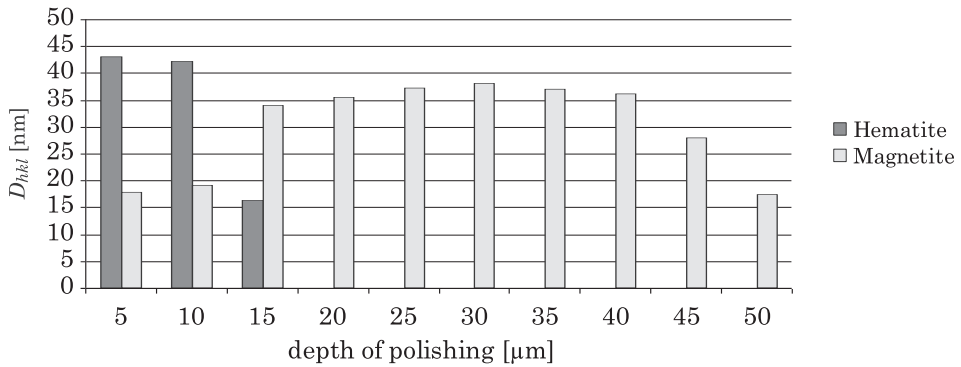


Fig. 4. Determination of crystallite size (D_{hkl}) for main peaks Fe_3O_4 and Fe_2O_3

The next, a slight decrease of crystallite size (D_{hkl}) was observed (The crystallite size for this oxide was 37.11 nm, 36.12 nm, 27.98 nm, 17,54nm after removal of the layer by 35 μm , 40 μm , 45 μm , 50 μm , respectively).

The size of crystallites, as well as the nature of stresses, affect the morphology and mechanical properties of the oxide layers (GWOŹDZIK 2014). The studies

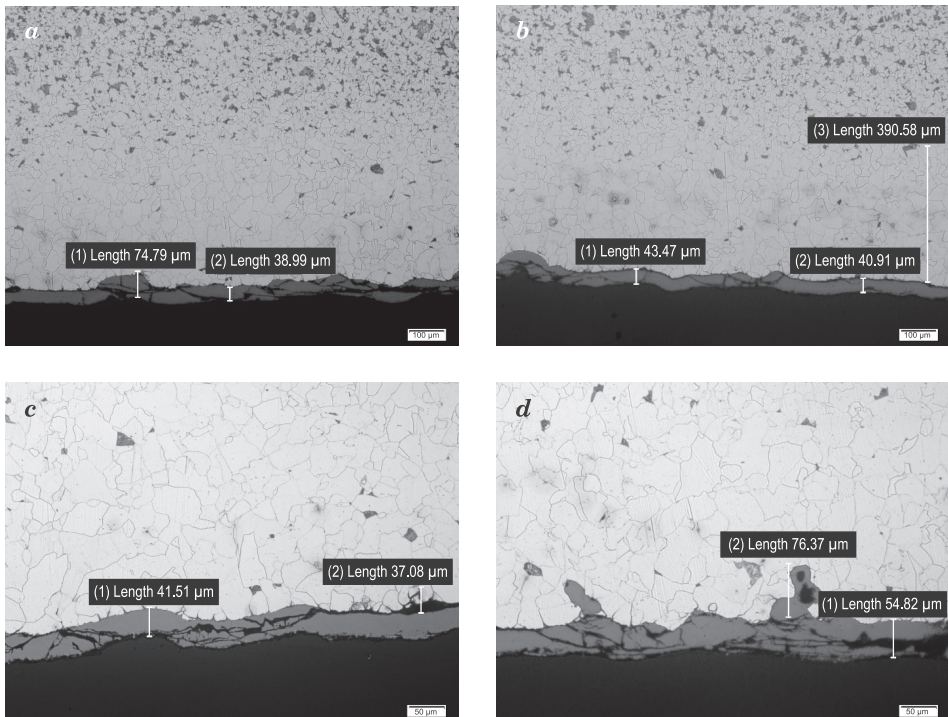


Fig. 5. The thickness of oxide layer formed on the steel examined, LM: *a, b* – 100 \times , *c, d* – 200 \times

have shown that crystallites for hematite are larger in size than crystallites for magnetite. In papers (GWOŹDZIK 2011, GWOŹDZIK, NIŹKIEWICZ 2011) it was shown that the outer oxide layer, i.e. hematite, is more brittle and prone to cracking, which is related to the size of crystallites.

The microscopic examination of the structure (Figs. 5, 6) have shown significant decarburization directly from the surface, which reaches a depth of 390.58 μm .

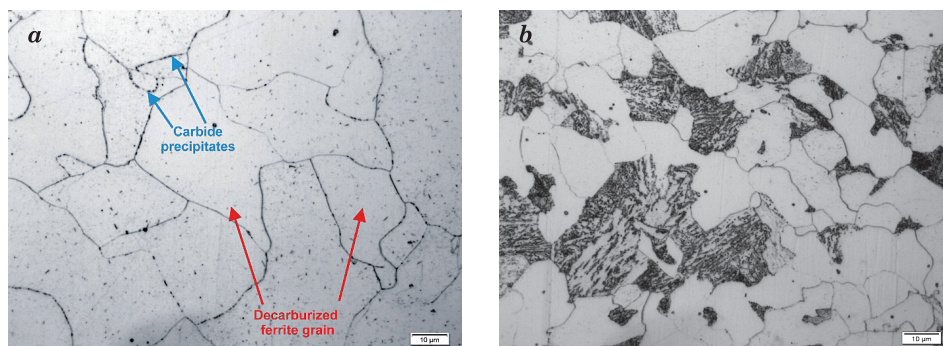


Fig. 6. Microstructure of 13CrMo4-5 steel, LM, 1000 \times :
a – 200 μm from oxide layer, *b* – 600 μm from oxide layer

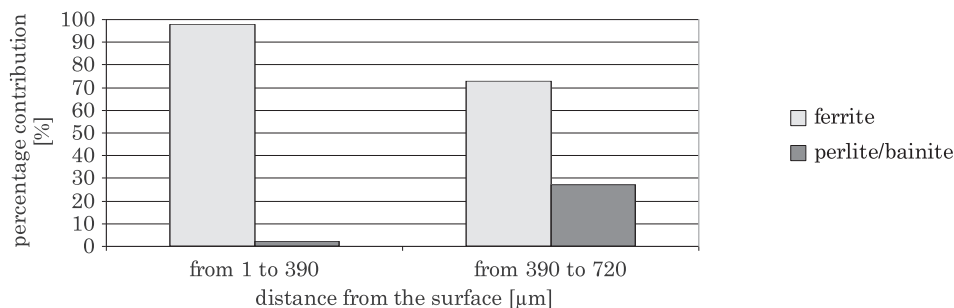


Fig. 7. Percentage contribution of ferrite and perlite/bainite

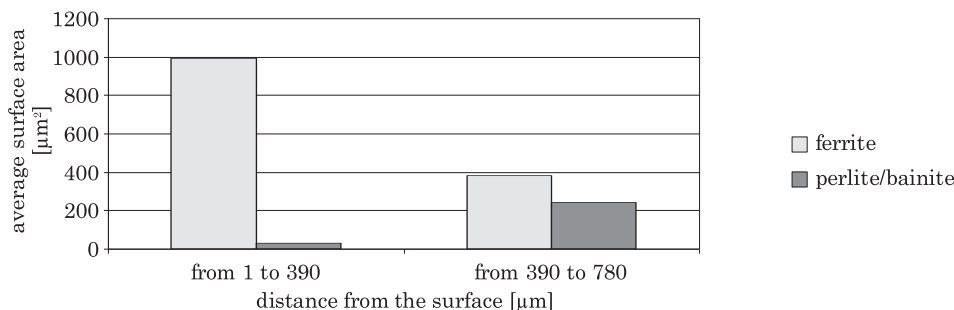


Fig. 8. Average surface area of ferrite and perlite/bainite

The quantitative phases analysis showed (Fig. 7) that only 2% perlite/bainite with a mean grain size of $28.46 \mu\text{m}^2$ (Fig. 8) was present in this area. Instead, the decarburized ferrite grain size was $992.25 \mu\text{m}^2$. In turn, the proportion of perlite/bainite to ferrite at a depth of $390 \mu\text{m}$ to $780 \mu\text{m}$ was 27% to 73%. The average grain size in this area was $382.46 \mu\text{m}^2$ and $243.27 \mu\text{m}^2$ respectively for ferrite and perlite/bainite. In addition, especially in the decarburised layer, a significant share of carbide precipitates distributed mainly at the grain boundaries was observed.

Summary

The research carried out on 13CrMo4-5 steel operated at 455°C for 130,000 h showed that:

- the structure of examined steel was ferrite and perlite/bainite with a share of 73% / 27%, respectively. The grain size of ferrite was $382.46 \mu\text{m}^2$, whereas perlite/bainite $243.27 \mu\text{m}^2$;
- from the inside of the pipe wall, there is considerable decarburization. In this part ferrite prevails 98% (the grain size $992.25 \mu\text{m}^2$), the rest was perlite/bainite, where the grain size was $28.46 \mu\text{m}^2$. In addition, there are the carbide precipitates along the grain boundaries that create chains in this places;
- the thickness of the oxide layer on the inner side of the pipe wall was $54.82 \mu\text{m}$. Numerous cracks and fissures were observed in this layer. Directly from the steel side there are pits covered with a layer of oxides;
- the phase analysis showed that the oxide layer is composed of Cu_2O , Fe_2O_3 , Fe_3O_4 ;
- the crystallite sizes for hematite is greater than for magnetite.

References

- BRUNÉ W., TRZESZCZYŃSKI J., HALIŃSKI J. 2011. *Remote diagnostics of main steam pipelines of power units*. 13th Informative & Training Symposium. Maintenance of thermo-mechanical power equipment. Management of the Productive Assets of a Group of Power Plants, p. 91–95.
- DOBOSIEWICZ J., BRUNNÉ K. 2007. *Ultrasonic measurement of oxides layer thickness on superheater coil inner surface*. *Energetyka*, 6: 460–464.
- GAWRON P. 2014. *Czystość wody kotłowej a uszkodzenia rur w rejonach przewężeń, na łukach oraz na odcinkach pochyłych*. *Dozór Techniczny*, 3, 54–58.
- GWOŹDZIK M. 2011. *Analiza zdefektowania warstw tlenkowych na stali X10CrMoVNb9-1 długotrwale eksploatowanej w temperaturze 535°C* . *Inżynieria Materiałowa*, 182(4): 432–434.
- GWOŹDZIK M., NITKIEWICZ Z. 2011. *Charakterystyka odporności na zarysowanie warstwy tlenkowej powstałej na stali P91*. *Inżynieria Materiałowa*, 182(4): 435–438.
- GWOŹDZIK M. 2014. *Mechanizm degradacji warstw tlenkowych na stalach długotrwale eksploatowanych w energetyce*. Monograph No. 291, Wydawnictwo Politechniki Częstochowskiej.

- GWOŹDZIK M. 2016a. *Analysis of Crystallite Size Changes in an Oxide Layer Formed on Steel Used in the Power Industry*. Acta Physica Polonica, A, 130(4): 935–938.
- GWOŹDZIK M. 2016b. *Structure Studies of Porous Oxide Layers Formed on 13CrMo4-5 Steels Long-Term Operated in the Power Industry*. Technical Sciences, 19(3): 257–266.
- KLEPACKI F., WYWROT D. 2010. *Life of resuperheater coils exposed to the effects of low-emission combustion*. 12th Informative & Training Symposium “Maintenance of thermo-mechanical power equipment. Upgrading power equipment to extend its operating period beyond 300.000 hours”, 28–30.09.2010, Wisła, p. 29–35.
- LAVERDE D., GOMEZ-ACEBO T., CASTRO F. 2004. *Continuous and cyclic oxidation of T91 ferritic steel under steam*. Corrosion Science, 46: 613–631.
- LELUSZ M. 2012. *Ocena zawartości aktywnego SiO₂ w popiołach lotnych wytwarzanych w obiektach energetycznych północno-wschodniej Polski*. Civil and Environmental Engineering, 3: 179–184.
- PRISS J., ROJACZ H., KLEVTSOV I., DEDOV A., WINKELMANN H., BADISCH E. 2014. *High temperature corrosion of boiler steels in hydrochloric atmosphere under oil shale ashes*. Corrosion Science, 82: 36–44.
- ŚLIWA A., GAWRON P. 2009. *Miedź w osadach w urządzeniach energetycznych – problem eksploatacyjny i remontowy*. Dozór Techniczny, 2: 40–43.
- TRZESZCZYŃSKI J. 2010. *Technical condition assessment of and life prediction for the critical components of thermo-mechanical power equipment intended to remain in service beyond 300 000 hours*. 12th Informative & Training Symposium: “Maintenance of thermo-mechanical power equipment. Upgrading power equipment to extend its operating period beyond 300.000 hours”, 28–30.09, Wisła, p. 13–21.



Quarterly peer-reviewed scientific journal

ISSN 1505-4675
e-ISSN 2083-4527

TECHNICAL SCIENCES

Homepage: www.uwm.edu.pl/techsci/



THE EFFECT OF TRAYS' SLOPE IN THE TUNNEL DRYER ON DRYING RATE OF CARROT CUBES

Jarosław Kubiaszczyk, Ewa Golisz, Małgorzata Jaros

Faculty of Production Engineering
Warsaw University of Life Sciences

Received 29 October 2018; accepted 7 December 2018; available online 10 December 2018.

Key words: carrot, convective drying, tunnel dryer, simulation, trays' slope.

Abstract

Drying of food is perhaps the oldest method of food preservation. The aim of this study was the analysis of the effect of changing the slope angle of trays in a tunnel dryer model on the drying rate. Real experiments were carried out for trays' slopes of 0, 5, 10 and 15°. Carrots' cubes were dried at a constant temperature of 60°C, with air flow velocity of 1.2 m/s. Also this process was simulated using the COMSOL Multiphysics 4.3 software. The research results showed that increasing slope angle of tray disrupted the laminar flow of the dried cubes layer through the drying air stream and forced the partial air flow through the layer. Thus, the contact surface of the heated air with the material particles and the drying rate have been increased and made it possible to shorten the duration of the drying.

Introduction

Convective drying of products with a high initial moisture content is a long-term and energy-consuming process as well as destructive in relation to biological products such as vegetables and fruits. However, this is the oldest, best known and therefore the most commonly used method of drying.

Many factors affect the convective drying process. One of them is the temperature of the drying agent. Higher temperature shortens the drying time

Correspondence: Ewa Golisz, Wydział Inżynierii Produkcji, Szkoła Główna Gospodarstwa Wiejskiego, ul. Nowoursynowska 164, 02-787 Warszawa, e-mail: ewa_golisz@sggw.pl

(SKORUPSKA 2005, SZARYCZ et al. 2011, VELEŞCU et al. 2013, GARBA et al. 2015, NADERINEZHAD et al. 2016, MAISNAM et al. 2017). In addition, the temperature affects the colour change. An increase in temperature and a longer drying time means that the colour of the dried material is darker (BILLER et al. 2005 SHARMA, PRASAD 2001, SUMNU et al. 2005). In the case of carrots, an increase in temperature causes a reduction in the content of β -carotene (GAWALEK 2005). Disadvantages of drying include unfavourable changes in the plant tissue caused by chemical reactions such as: non-enzymatic browning, changes in vitamins or oxidation processes (NOWACKA, WITROWA-RAJCHERT 2007), decrease in anthocyanin content (in strawberries, MORALES-DELGADO et al. 2014). During convective drying, the highest loss of volatile compounds was observed compared to other drying methods (CALÍN-SÁNCHEZ et al. 2012). Another important factor is the speed and direction of air flow relative to the material to be dried. Higher airflow speeds up the moisture removal process (VELIĆ et al. 2004, ZLATANOVIĆ et al. 2013, VELEŞCU et al. 2013, NADERINEZHAD et al. 2016). WITROWA-RAJCHERT and RADECKA'S research (2005) showed that the air flow through the layer shortens the drying time compared to drying along the layer, while the shortest drying time was observed during fluidized bed drying.

The length of the convective drying time is also influenced by grinding degree of raw material (GŁOWACKI et al. 2005, FERNANDO et al. 2011), geometric shape of the sample (BÉTTEGA et al. 2014, NADERINEZHAD et al. 2016) and physical properties dependent on the variety (NOWAK et al. 2005). DING et al. (2015) investigated the effect of different voltages on carrot drying rate. One of the basic physical changes taking place during drying is the drying shrinkage, which is manifested by the reduction of the volume of the dried material and, as a result, its density (WANG, BRENNAN 1995, PABIS, JAROS 2002). The disadvantage of this drying method at lower drying temperatures, although it results in a better quality of the final product and low flow of the drying medium, is a long drying time. Due to the above reasons, for many years various works have been undertaken to increase the efficiency of the drying process. The use of convection allows for both drying of large batches and getting a dried material of relatively good quality. Frequently, tunnel dryers are used in practice. The material to be dried is placed on trays filling the trolleys and placed in a drying tunnel. The drying air is forced into the tunnel generally co-currently or countercurrently manner with the direction of movement of the carriages. The range of flow velocity of the drying air stream causes that it flows over the layer laminar, possibly turbulent – in points of local flow disturbance due to various resistance. Thus, the air flows around the dried material, having contact with it mainly along the upper horizontal surface of the layer, while the local velocity of the drying air over this surface is greater than over the other surfaces of the particle.

Currently, it is possible to simulate such phenomena using specialized software, for example COMSOL Multiphysics. This tool is used, among others, to simulate phenomena related to fluid flow, including laminar flow, turbulent and coupled heat transfer (COMSOL Multiphysics... 2013). This software has been used, for example, to develop heat and mass transfer models during convective drying of fruits, depending on their shrinkage and temperature (KUMAR et al. 2012a) and variable material properties (KUMAR et al. 2012b). GERLICH et al. (2013) used COMSOL Multiphysics 4.3. for calculating the heat transfer in buildings and DZIAK et al. (2009) determined the values of heat and mass transfer coefficients during evaporation from a thin layer of a two-component liquid solution of high viscosity.

Increasing the active surface of heat exchange and mass of a moist material, dried convectively in a tunnel drier, i.e. with forced horizontal flow of the drying air stream, should result in a higher drying rate of this material. Therefore, a simple technical solution, increasing the efficiency of drying, would be to increase the active drying surface by sloping the trays. Therefore, the aim of the work was to examine how the inclination of the trays from the horizontal level by a certain angle will affect the drying rate of carrot cube in a tunnel dryer. In this study was analysing also how the flow of air flowing over the carrot inside the dryer changes. For this purpose, actual measurements and simulation tests were carried out using COMSOL Multiphysics 4.3 software.

Materials and methods

Carrot cubes of 0.01 ± 0.001 m side were used as a research material. Carrot came from a single source. Cubes were prepared from carrot roots of even shape and mass. The initial mass of sample was 0.230 ± 0.001 kg. The dry mass was determined according to PN-A-75101-03:1990 standard. Moisture content was determined according to the equation:

$$u(\tau) = \frac{m(\tau) - m_{ss}}{m_{ss}} \tag{1}$$

where:

- τ – drying time [min],
- $u(\tau)$ – moisture content at time τ [kg kg^{-1}],
- $m(\tau)$ – mass at time τ [kg],
- m_{ss} – mass of dry substance [kg].

Experiment

Carrots cubes were dried in a laboratory tunnel dryer equipped with trays of adjustable slope from 0 to 20° relative to the horizontal plane. The laboratory tunnel dryer used in real previous experiments had four sections, four trays with dimensions of 0.25 × 0.40 m, positioned from each other vertically at distance 0.10 m. However, placing trays in the dryer with the possibility of changing the slope angle forces the number of trays to be reduced to 12.

The experiments were carried out for trays' slopes of 0, 5, 10 and 15°. The measurements were carried out at a constant temperature of 60°C, flow rate of 1.2 m/s. Relative humidity and drying air pressure was the same as in the laboratory, i.e. 40% and about 1,000 (±15) hPa. The measurements of moisture content were made from initial to a final moisture content of 0.01 kg·kg⁻¹. To assess the influence of the trays' slope on drying time calculated the relative differences in moisture content samples after the same drying time were calculated relative to the moisture content in the 0 sample – dried on a horizontal tray, according to the equation:

$$\Delta u_{\%} = 100 \frac{u(0^{\circ}, \tau_i) - u(S^{\circ}, \tau_i)}{u(0^{\circ}, \tau_i)} \quad (2)$$

where:

- $\Delta u_{\%}$ – relative differences of moisture content [-],
- $u(0^{\circ}, \tau_i)$ – moisture content in sample on a horizontal tray [kg·kg⁻¹],
- $u(S^{\circ}, \tau_i)$ – moisture content in the sample on a tray inclined at angle of S° [kg·kg⁻¹].

The effect of tray slope on the drying efficiency of the examined drying variants was also examined by determining the coefficients of: the initial drying rate and heat transfer. The carrot's cubes have a large initial moisture content, therefore in the relevant time range, the drying rate at the set temperature is determined by external mass exchange conditions. An indicator of this is the coefficient of heat transfer to the surface, depending on the speed of the drying air stream flowing over the boundary layer of the dried objects. The drying rate in this period is constant and is expressed by the equation (PABIS 1982):

$$\frac{du}{d\tau} = k_0 = \frac{\alpha A}{r \rho_s V_s} (t_p - t_M) \quad (3)$$

where:

- α – coefficient of heat transfer [W·(m²K)⁻¹],
- A – material surface [m²],
- k_0 – coefficient of initial drying rate [min⁻¹],

- r – heat of evaporation [$\text{kJ} \cdot \text{kg}^{-1}$],
- ρ_s – density of dry material [$\text{kg} \cdot \text{m}^{-3}$],
- V_s – volume of dry material [m^3],
- t_p – temperature of the drying agent [$^{\circ}\text{C}$],
- t_M – temperature of the wet thermometer [$^{\circ}\text{C}$].

Equation (3) is the basis for the formulation of theoretical models of the first drying period. The structure of the theoretical model taking into account the shrinkage (PABIS, JAROS 2002) is a third degree polynomial with the form:

$$u(\tau) = u_0 - k_0\tau + C_2\tau^2 + C_3\tau^3 \tag{4}$$

where:

- u_0 – initial moisture content [$\text{kg} \cdot \text{kg}^{-1}$],
- C_2, C_3 – model coefficients [-].

The k_0 values of the drying rate coefficient, in the tested tray settings, were taken from the trend function – third degree polynomials, matched for moisture content measurements. Then the values of αA were calculated from the equation (3).

Comparison of these values gives the premise to formulate the conclusion about the impact of the angle of tray settings in the tunnel dryer on the drying rate of the tested carrot cubes.

Simulation

For the purpose of simulating the drying process COMSOL Multiphysics 4.3 application was used. First a tunnel dryer model with trays and material in the form of cubes was created. The model also included tray holders and a grid placed at the end of one diffuser because these elements significantly affect the airflow inside the dryer. Next, the model was covered with a computational mesh consisting of approximately 130,000 irregular triangles (Fig. 1). The compaction degree at the trays, holders and diffuser inlet is higher since those are elements which affect the most an air flow.

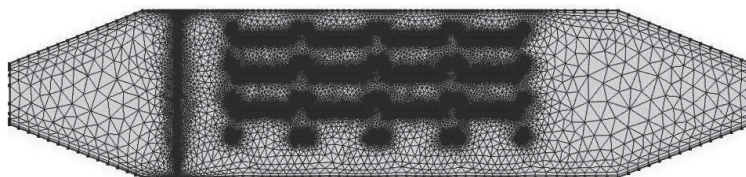


Fig 1. Model of a laboratory tunnel dryer with a mesh

In COMSOL Multiphysics 4.3 was used the Navier-Stokes equation in the form:

$$\rho(u \cdot \nabla)u = \nabla \cdot [-p + \eta(\nabla u + (\nabla u)^T) - \frac{2}{3}\eta(\nabla \cdot u)] + F$$

$$\nabla(\rho u) = 0 \quad (5)$$

where:

- ρ – air density [$\text{kg} \cdot \text{m}^{-3}$],
- u – air velocity [$\text{m} \cdot \text{s}^{-1}$],
- p – the pressure [Pa],
- η – dynamic viscosity [$\text{Pa} \cdot \text{s}$],
- T – temperature [K],
- F – volume force [$\text{N} \cdot \text{m}^{-3}$].

Boundary conditions used in the model were: no slip, stationary and laminar flow, geometry 2D. As the initial condition for the simulation was assumed the air velocity of 1.2 m/s and pressure 1000 hPa at the inlet to the dryer chamber. Density and viscosity of air were calculated by the program for the assumed temperature.

Results and discussion

Drying kinetics

The results of measurements of moisture content of carrot cubes, dried in a tunnel dryer for different slopes of trays, depending on time, are presented in Figure 2.

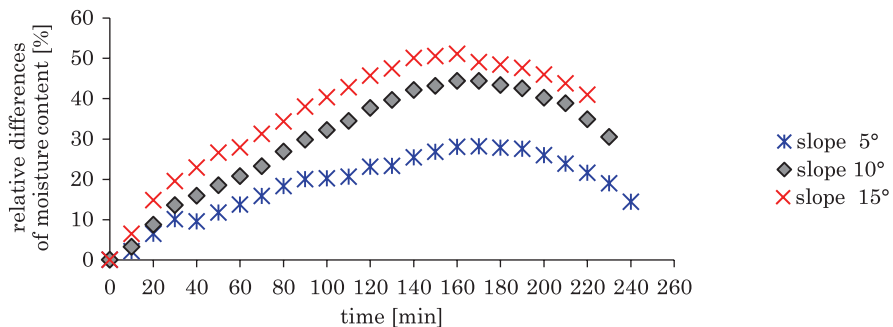


Fig. 2. Graph of changes in moisture content of dried carrot cubes at various slope angles of tray

Analysing the effect of different slopes of trays on moisture content of carrot cubes it was observed that for the largest trays' slope the drying process ran the fastest. It can be supposed that increasing the slope of trays increased the active surface of drying, which caused that the heat and mass exchange runs faster, so the drying process is shorter. For example, without slope of tray, the moisture content of 1 kg/kg was achieved after 160 minutes of drying, for slope 5° after time 140 minutes, for 10° after 130 minutes and for the largest angle 15° after 120 minutes. Analysing the results of moisture content measurements, it was found that increasing the slope of trays by another 5° resulted in shortening the drying time by 10 next minutes. Then the percentage changes in the moisture content were analysed.

Figure 3 presents percentage differences in moisture content in dried samples relative to drying time determined for 0 sample – dried on a horizontal tray (equation 2).

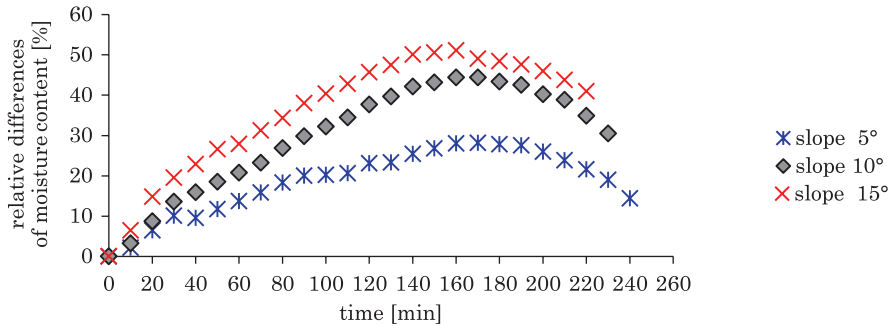


Fig. 3. Differences in the moisture content in the samples relative to the drying time in the 0 sample – dried on a horizontal tray

The highest percentage differences in moisture content in dried samples relative to drying time determined for 0 sample – dried on a horizontal tray were observed after a drying time of 160 min, it was: 28, 44, 51% respectively for slope of trays of 5, 10, 15°.

The effect of the slope of tray on a dried sample of carrot cubes can be concluded on the basis of the coefficients determined from the model (3) and (4), whose values are summarized in Table 1.

It can be noticed that the drying rate of the same carrot cubes mass increases with the increase of tray's slope – the coefficient of the initial drying rate k_0 increases. Its value has increased by about 60% for a slope of 15° compared to without slope of tray.

Similarly, the product of the heat transfer coefficient and the αA surface increases for the higher slope of tray. The largest values of k_0 and αA were obtained for slope of 15°.

Table 1

Parameters of the drying model			
Slope of tray [°]	Coefficient of initial drying rate k_0 [min^{-1}]	Mass of dry substance m_{ss} [kg]	Product of heat transfer coefficient and surface [W/K]
0	0.096	0.00243	0.2117
5	0.121	0.00244	0.2657
10	0.134	0.00244	0.2962
15	0.158	0.00244	0.3478

Computer simulation

The next stage of the research was a computer simulation of air flow in a dryer with 12 trays in COMSOL Multiphysics 4.3 software. It can illustrate the way and parameters of air flow at various slope of the trays and at any

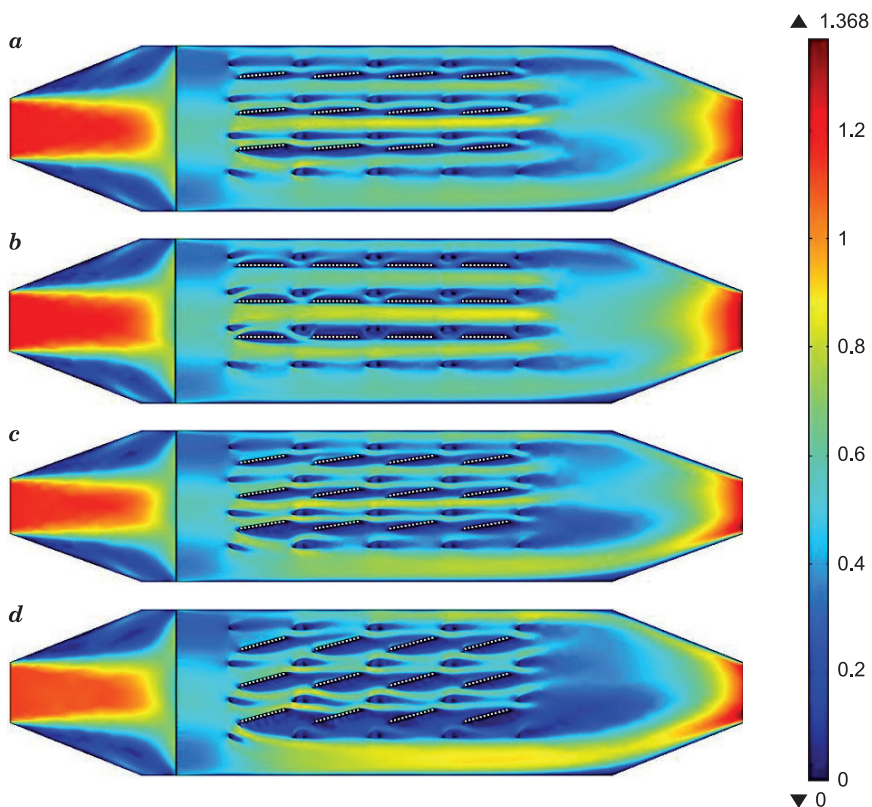


Fig. 4. Simulation of air flow: *a* – trays in horizontal position, *b* – trays' slopes of 5°, *c* – trays' slopes of 10°, *d* – trays' slopes of 15°

places of the drying chamber, in which measurement is practically impossible (KUBIASZCZYK 2017). Figure 4 shows the result of air flow simulation for selected slopes of trays.

Analysing Figure 4 it can be noticed that for trays in horizontal position the air flew only along the material placed on the trays. Values of airflow velocities indicate laminar flow or laminar but disturbed in the central part of the drying chamber. The air stream was lifted up during contact with material particles, which caused that the airflow velocity near above the layer decreased. In this case, an increase of air velocity along the layer allows for shorten the drying time and thus increase the efficiency of the process. Increasing a slope of trays forced the airflow through the layer thus the active drying surface also increased. Changing the slope of trays to the value of 15° caused an expansion of the active drying surface. The airflow velocity at the bottom of the chamber also increased. In general, the increase of the trays' slope caused a decreasing the surface of the high velocity air stream that occurred between the trays.

Table 2 presents the minimum and maximum values of air flow velocities along and through the material placed on trays of different slopes, obtained from simulation.

Analysing the data in Table 2, it can be noticed that the highest air flow velocities along and through the material layer were observed for slope of 15°.

Table 2

Simulated values of air flow velocity along and through the layer

Slope of tray [°]	The velocity of the air flow along the layer [m/s]		The velocity of air flow through the layer [m/s]	
	min.	max.	min.	max.
0	0.03	0.12	–	–
1	0.03	0.40	–	–
2	0.03	0.53	–	–
3	0.06	0.64	0.06	0.18
4	0.07	0.69	0.06	0.20
5	0.07	0.73	0.06	0.21
6	0.07	0.75	0.06	0.21
7	0.07	0.77	0.07	0.25
8	0.07	0.79	0.08	0.29
9	0.07	0.82	0.08	0.33
10	0.07	0.85	0.08	0.35
11	0.07	0.88	0.09	0.40
12	0.08	0.88	0.09	0.43
13	0.09	0.88	0.09	0.46
14	0.11	0.88	0.10	0.50
15	0.12	0.88	0.10	0.55

On the other hand, the smallest values occurred during traditional drying method, without sloping the trays. For minimum airflow velocities, the first change occurred at an angle of 3°, then above 11°. At maximum airflow velocities a sudden increase was observed already at the first change of slope. Subsequent trays' slope changes allowed gradual change of the airflow velocity along the layer.

The air flow through the material layer was forced already at the trays' slope of 3°. It can be noticed that airflow velocity increase is not directly proportional to the change of slope. When changing the trays' slope, a change in the heat exchange surface took place. As the slope increased, the active drying surface also increased. At the slope of 15°, the air flow through the layer did not cover the entire surface of the dried material. This phenomenon shows that it is possible to further optimize the process, but it must be remembered that too large slope may result in sliding material from the trays.

Conclusions

Drying carrot cubes in the same conditions in the drying tunnel, on inclined tray by 5, 10 and 15°, shortened the drying time and allowed to reduce the moisture content by 30–50% at the moisture content around 1 kg·kg⁻¹.

The coefficient of the initial drying rate increased with the increase of the slope angle of the tray. This was caused by the increase of the air flow velocity along the layer, the occurrence of the flow through the layer and the increase of the contact surface of the material particles with the drying agent.

The computer simulation illustrated that increasing the slope angle of trays increases the flow velocity of the drying agent along the dried material and forces the flow of air through the layer of raw material laid on the tray. Another phenomenon, which was caused by the flow of the drying agent between the raw material particles, is the increase of contact surface of the stream of heated air of higher velocity with particles of the dried material, which results in a shorter drying time.

Acknowledgements

The authors thank dr Monika Janszek-Mańkowska for linguistic and content-related consultations during editing the text of this manuscript.

References

- BÉTTEGA R., ROSA J.G., CORRÊA R.G., FREIRE J.T. 2014. *Comparison of carrot (Daucus carota) drying in microwave and in vacuum microwave*. Braz. J. Chem. Eng., 31(2).
- BILLER E., WIERZBICKA A., PÓLTORAK A. 2005. *Wpływ obróbki termicznej na zmiany parametrów barwy na przykładzie marchwi*. Inżynieria Rolnicza, 69(9): 7–12.
- CALÍN-SÁNCHEZ Á., LECH K., SZUMNY A., FIGIEL A., CARBONELL-BARRACHINA A.A. 2012. *Volatile composition of sweet basil essential oil (Ocimum basilicum L.) as affected by drying method*. Food Research International, 48(1): 217–225.
- COMSOL Multiphysics. User's Guide. Version 4.3. Comsol. 2013. The COMSOL® Software Product Suite, <https://www.comsol.com/products>.
- DING C., LU J., SONG Z. 2015. *Electrohydrodynamic Drying of Carrot Slices*. PLoS One, 10(4): e0124077.
- DZIAK J., KAPŁON J., KOLEK A., KRÓLIKOWSKI L. 2009. *Badania równoczesnego transportu ciepła i masy w procesie cienkowarstwowego odparowywania roztworów o podwyższonej lepkości*. Politechnika Wroclawska, Wroclaw.
- FERNANDO W.J.N., LOW H.C., AHMAD A.L. 2011. *Dependence of the effective diffusion coefficient of moisture with thickness and temperature in convective drying of sliced materials. A study on slices of banana, cassava and pumpkin*. Journal of Food Engineering, 102(4): 310–316.
- GARBA U., KAUR S., GURUMAYUM S., RASANE P. 2015. *Effect of hot water blanching time and drying temperature on the thin layer drying kinetics and anthocyanin degradation of black carrot (Daucus carota l.) shreds*. Food Technology and Biotechnology, 53(3): 324–330.
- GAWAŁEK J. 2005. *Wpływ warunków konwekcyjnego i sublimacyjnego suszenia korzeni marchwi na jakość suszu*. Inżynieria Rolnicza, 71(11): 119–127.
- GERLICH V., SULOVSÁK K., ZÁLEŠÁK M. 2013. *COMSOL Multiphysics validation as simulation software for heat transfer calculation in buildings: Building simulation software validation*. Journal of the International Measurement Confederation, 46: 2003–2012.
- GŁOWACKI S., SOJAK M., KOZBIAL B. 2005. *Wpływ kształtu cząstek krajanki jabłek na czas suszenia w warunkach konwekcji wymuszonej*. Inżynieria Rolnicza, 62(2): 45–55.
- KUBIASZCZYK J. 2017. *Symulacja kinetyki suszenia marchwi w tunelu suszarniczym przy zmianach kąta nachylenia sit*. Praca magisterska, SGGW, Warszawa.
- KUMAR C., KARIM A., JOARDDER MUH. MILLER G. 2012a. *Modeling heat and mass transfer process during convection drying of fruit*. In The 4th International Conference on Computational Methods (ICCM2012), Crowne Plaza, Gold Coast, Australia.
- KUMAR C., KARIM A., SAHA S.C., JOARDDER M., BROWN R.J., BISWAS D. 2012b. *Multiphysics modelling of convective drying of food materials. Multiphysics modelling of convective drying of food materials*. In Proceedings of the Global Engineering, Science and Technology Conference, Global Institute of Science and Technology, Dhaka, Bangladesh.
- MAISNAM D., RASANE P., DEY A., KAUR S., SARMA C. 2017. *Recent advances in conventional drying of foods*. Journal of Food Technology and Preservation, 1(1).
- MORALES-DELGADO D.Y., TELLEZ-MEDINA D.I., RIVERO-RAMEREZ N.L., ARELLANO S. 2014. *Effect of convective drying on total anthocyanin content, antioxidant activity and cell morphometric parameters of strawberry parenchymal tissue (Fragaria × ananassa Dutch)*. Revista Mexicana de Ingeniería Química, 13(1): 179–187.
- NADERINEZHAD S., ETESAMI N., NAJAFABADY A.P., FALAVARJANI M.G. 2016. *Mathematical modeling of drying of potato slices in a forced convective dryer based on important parameters*. Food Science and Nutrition, 4(1): 110–118.
- NOWACKA M., WITROWA-RAJCHERT D. 2007. *Wybrane właściwości fizyczne suszonych produktów roślinnych*. In: *Wybrane właściwości fizyczne suszonych surowców i produktów spożywczych*. Wydawnictwo Naukowe FRNA, Lublin, p. 35–43.

- NOWAK D., POMARAŃSKA-ŁAZUKA W., LEWICKI P.P. 2005. *Wpływ odmiany selera korzeniowego na przebieg procesu suszenia*. Inżynieria Rolnicza, 69(9): 233–240.
- PABIS S. 1982. *Teoria konwekcyjnego suszenia produktów rolniczych*. Państwowe Wydawnictwo Rolnicze i Leśne, Warszawa.
- PABIS S., JAROS M. 2002. *The first period of convection drying of vegetables and the effect of shape-dependent shrinkage*. Biosystems Engineering, 81(2): 201–211.
- SHARMA G.P., PRASAD S. 2001. *Drying of garlic (Allium sativum) cloves by microwave-hot air combination*. Journal of Food Engineering, 50(2): 99–105.
- SKORUPSKA E. 2005. *Badanie procesu suszenia konwekcyjnego pietruszki korzeniowej*. Inżynieria Rolnicza, 69(9): 313–320.
- SUMNU G., TURABI E., OZTOP M. 2005. *Drying of carrots in microwave and halogen lamp-microwave combination ovens*. LWT- Food Science and Technology, 38(5): 549–553.
- SZARYCZ M., LECH K., JAŁOSZYŃSKI K. 2011. *Zależność współczynnika dyfuzji wody w kostkach marchwi od temperatury powietrza suszącego*. Inżynieria Rolnicza, 130(5): 275–282.
- VELEŠCU I.D., ȚENU I., CĂRLESCU P., DOBRE V. 2013. *Convective Air Drying Characteristics for Thin Layer Carrot*. Bulletin UASVM Food Science and Technology, 70(2): 129–136.
- VELIĆ D., PLANINIĆ M., TOMAS S., BILIĆ M. 2004. *Influence of air velocity on kinetics of convection apple drying*. Journal of Food Engineering, 64(1): 97–102.
- WANG N., BRENNAN J.G. 1995. *Changes in structure, density and porosity of potato during dehydration*. Journal of Food Engineering, 24(1): 61–76.
- WITROWA-RAJCHERT D., RADECKA-WIERZBICKA M. 2005. *Wpływ techniki suszenia konwekcyjnego na wybrane wyznaczniki jakości suszonej tkanki roślinnej*. Inżynieria Rolnicza, 69(9): 387–393.
- ZLATANOVIĆ I., KOMATINA M., ANTONIJEVIĆ D. 2013. *Low-temperature convective drying of apple cubes*. Applied Thermal Engineering, 53(1): 114–123.